Multi-scale and multimodal characterization of the ferret brain development using diffusion MRI and histology

Céline Delettre

THÈSE de DOCTORAT
de l'Université de Paris

École doctorale Bio Sorbonne Paris Cité (ED 562)
Specialité: Neurobiologie

Laboratoire de Génétique Humaine et Fonctions Cognitives
Institut Pasteur, Paris
et
Institute of Computational Neuroscience
University Medical Center Hamburg-Eppendorf

Multi-scale and multimodal characterization of the ferret brain development using diffusion MRI and histology

présentée par

Céline Delettre

Soutenue publiquement le 16 décembre 2020
devant le jury constitué de :

M.	**Daniel MARGULIES**	ICM, Univ. de Paris	Président du jury
M.	**Olivier COULON**	INT, Aix-Marseille Univ.	Rapporteur
M.	**Demian WASSERMANN**	INRIA, Univ. Paris-Saclay	Rapporteur
Mme.	**Jessica DUBOIS**	NeuroDiderot, Univ. de Paris	Examinatrice
Mme.	**Reem KHALIL**	American Univ. of Sharjah	Examinatrice
Mme.	**Camille MAUMET**	INRIA, Univ. de Rennes	Examinatrice
M.	**Roberto TORO**	Inst. Pasteur, Univ. de Paris	Directeur de thèse
M.	**Claus C. HILGETAG**	UKE, Hamburg Univ.	Co-directeur de thèse

Acknowledgements

First, I would like to thank my supervisors, Roberto Toro and Claus Hilgetag, for giving me the opportunity to work on this unique project. Thank you for giving me access to these various datasets and getting the chance to learn how to process them from scratch. And especially thank you for letting me work flexibly between France and Germany.

Many thanks to the GHFC and ICNS colleagues for the friendly work environment as well as the good advice.

In this process I have also learned to ask for help and was always happily surprised to find someone online or at a conference to give that extra push which would bring me closer to the finish line. So thank you to: Cameron Craddock (Brainhack), Eleftherios Garyfallidis (Dipy), Szabolcs Dávid (ExploreDTI), Thijs Dhollander (MRtrix), neurolabusc (Bru2Nii), mhogg (pyoctree), jcupitt (vips), Nick Tustison (ANTs), teseoch (libigl-python-bindings), Francis Williams (libigl-python-bindings).

But also many thanks to our collaborators at the Instituto de Neurosciencias (Alicante) and from Neurospin (Saclay) for the acquisition of the data. Thank you to David Briand for helping me with the Axioscan. Thank you to Arnaud Messé for sharing with me your experience with diffusion MRI. Thank you to Farid Kandil and Nicolas Traut for your help with the statistics. And thank you to Leigh-Anne Dell for sharing with me your knowledge about neuroanatomy and your coaching for the writing of this thesis.

Finally I would like to thank my family and friends, french and german, for their support during these 4 years and always reminding that even when I felt stuck, I should keep trust and I would eventually find a way to fix it.

Multi-scale and multimodal characterization of the ferret brain development using diffusion MRI and histology

The cytoarchitectonic organization of the brain and its connectivity are important substrates for brain function and behavior. A disruption in the structural organization (cytoarchitecture or connectivity) can cause neurological impairments (e.g. stroke). Moreover, early brain development is a period during which the brain is very plastic and a disruption in its structural development can cause neurodevelopmental disorders such as autism spectrum disorders or schizophrenia. The development of brain structure occurs at different scales. In this work we examined the whole brain, regional and laminar/cellular levels. The interactions within these levels can also be reported using different modalities. We focused on tract-tracing at the microscopic scale and diffusion MRI at the macroscale scale. We used these methods to study the structural connectivity between different brain areas at the different scales.

We adopted a multi-scale and multimodal approach to characterize the ferret brain development, structural connectivity and cytoarchitecture. We used diffusion MRI to describe structural brain connectivity and histological Nissl slices, to describe the cellular organization. The ferret was specifically chosen as the animal model because during their first days postnatally, they provide an opportunity to witness processes which occur during the last trimester of gestation in humans.

To summarize, (1) we validated the use of non-invasive diffusion MRI in the adult ferret by comparing its results to the precise quantifications obtained by tract-tracing. (2) We developed a semi-automated pipeline for extracting whole brain quantifications from microimages of Nissl stained slices, informing us about the development of the cytoarchitectonic organization. These quantifications allowed us to identify a laterodorsal gradient of maturation of the cortical lamination. This gradient is present up until 4 weeks postnatally, after which all the layers are formed. (3) The histological slices were registered to the MRI dataset in order to investigate the relationship between the maturation of cortical lamination and the development of cortico-cortical connectivity. We observed that the similarity of cytoarchitectonic organization of two brain areas of ferrets as young as 4 postnatal days (P4), indicated a higher likelihood of interconnection at P32 and at the adult stage. This relationship was, however, not maintained when predicting the connectivity likelihood at earlier stages (from P4 to P16). This indicates that the footprint of the mature cytoarchitectonic organization is already present early in development (P4) and prior to the one of mature connectivity which appears around P32.

Keywords

Ferret; Brain development; Structural connectivity; Diffusion tractography; Cytoarchitecture; Histology

Caractérisation multi-échelle et multimodale du développement du cerveau du furet par IRM de diffusion et histologie

L'organisation cytoarchitectonique du cerveau et sa connectivité sont des éléments essentiels pour le fonctionnement du cerveau et le comportement. Une perturbation de l'organisation structurelle du cerveau (cytoarchitectonie ou connectivité) peut entraîner des troubles neurologiques (comme, par exemple, un accident vasculaire cérébrale). Le développement précoce du cerveau est une période durant laquelle le cerveau est très plastique et une perturbation de son développement structurel peut provoquer des troubles neurodéveloppementaux tels que des troubles du spectre autistique ou de la schizophrénie. Le développement de la structure cérébrale se produit à différentes échelles. Dans ces travaux, nous avons analysé le cerveau à l'échelle du cerveau entier, à l'échelle régionale et laminaire/cellulaire. Les interactions entre ces différents niveaux peuvent également être capturés en utilisant différentes modalités d'acquisition. Nous avons utilisé des traceurs à l'échelle microscopique et l'IRM de diffusion à l'échelle macroscopique. Ces méthodes nous ont permis d'étudier la connectivité structurelle entre différentes régions cérébrales à différentes échelles.

Grâce à notre approche multi-échelle et multimodale nous avons caractérisé le développement cérébral du ferret, sa connectivité structurelle et son organisation cellulaire. Nous avons utilisé l'IRM de diffusion pour décrire la connectivité structurelle et des coupes histologiques marquées au Nissl pour décrire l'organisation cellulaire. Le furet a été spécifiquement choisi comme animal modèle car pendant les premiers jours après la naissance, il permet d'étudier des phénomènes qui se produisent au cours du dernier mois de gestation chez l'Homme.

En résumé, (1) nous avons validé l'utilisation de l'IRM de diffusion non-invasive chez le furet adulte en comparant ses résultats aux quantifications précises obtenues par les traceurs. (2) Nous avons développé une pipeline semi-automatisée pour extraire les quantifications de micro-images de coupes histologiques marquées au Nissl pour le cerveau entier, nous informant sur le développement de l'organisation cytoarchitectonique. Ces quantifications nous ont permis d'identifier un gradient latéro-dorsal de maturation de la stratification corticale. Ce gradient est présent jusqu'à 4 semaines après la naissance, après quoi toutes les couches sont formées. (3) Les coupes histologiques ont été recalées aux données d'IRM afin d'étudier la relation entre la maturation de la stratification corticale et le développement de la connectivité cortico-corticale. Nous avons observé que la similitude de l'organisation cytoarchitectonique de deux régions cérébrales de furets à partir de 4 jours postnatals (P4), indiquait une probabilité plus élevée d'interconnexion à P32 et à l'âge adulte. Cette relation n'était cependant pas maintenue lors de la prédiction de la probabilité de connectivité aux stades antérieurs (de P4 à P16). Cela indique que l'empreinte de l'organisation cytoarchitectonique mature est déjà présente au début du développement (P4) et précède celle de la connectivité mature qui apparaît autour de P32.

Mots clés

Furet; Développement cérébral; Connectivité structurelle; Tractographie; Cytoarchitectonie; Histologie

List of publications

Published

Delettre, Céline; Messé, Arnaud; Dell, Leigh-Anne; Foubet, Ophélie; Heuer, Katja; Larrat, Benoit; Meriaux, Sebastien; Mangin, Jean-Francois; Reillo, Isabel; de Juan Romero, Camino; Borrell, Victor; Toro, Roberto; Hilgetag, Claus. (2019). "Comparison between diffusion MRI tractography and histological tract-tracing of cortico-cortical structural connectivity in the ferret brain". en. In: *Network Neuroscience* 3.4, pp. 1038–1050.

Submitted

Messé, Arnaud; Hollensteiner, Karl; **Delettre, Céline**; Dell, Leigh-Anne; Pieper, Florian; Nentwig, Lena; Galindo-Leon, Edgar; Larrat, Benoit; Meriaux, Sebastien; Mangin, Jean-Francois; Reillo, Isabel; de Juan Romero, Camino; Borrell, Victor; Engler, Gerhard; Toro, Roberto; Engel, Andreas; Hilgetag, Claus. (2020). "Structural basis of envelope and phase intrinsic coupling modes of the cerebral cortex". Submitted to: *Neuroimage*. Available on *biorxiv*.

Contents

List of Figures

Copyrighted figures

Figure 1.1: figure 1 from Toro 2012. "**Diversity of the mammalian brain shape.** Lateral aspect of various mammalian brains, drawn at the same scale. Based on images from http://brainmuseum.org" Toro 2012

Figure 1.2: figure from Brodmann 1909. **Brodmann's cytoarchitectonic parcellation.**

Figure 1.3: figure 10 from Dombrowski, Hilgetag, and Barbas 2001. **Sketch of the cytoarchitectonic types described in terms of lamination and neuronal density (Nissl stain).**

Figure 1.5: figure 2 from Sawada and Watanabe 2012. "**Dorsal views of brain of male ferrets on postnatal days (PD) 4 to 90.**" Sawada and Watanabe 2012

List of Tables

Chapter 1

General introduction

The brain, like any complex system (organ, organism, population, planet, planetary system) can be examined from many aspects and at different scales. In this work we will investigate the ferret brain; its structural components and the physical connections between these components, at different scales. The application of a multi-scale approach will allow us to obtain a holistic view of brain connectivity and combine it with the precision of microscopic scales. In addition, we will examine how the cerebral organization develops and evolves to a mature brain.

1.1 Multi-scale - how is the brain structure organized ?

Firstly, I will define the different scales at which we can observe the organization of the cortex and then provide a description of the brain structure observed across these scales.

On a macroscopic scale and clearly identifiable with the naked eye, the cortex is comprised of an outer layer of grey matter (GM) (primarily neuronal cell bodies combined with axonal tracts, glia, capillary blood vessels and neuropil) and a white matter (WM) core (primarily myelinated axons combined with oligodendrocytes and astrocytes). On a mesoscopic scale, different cortical regions or parcellations can be observed based on differences observed in the cellular morphology (shape, size and class of neurons). To have an understanding of the cellular organization of the cortex, one needs to examine the cortex at a microscopic level to recognize that the cellular components of the cortex are not only arranged in functional layers known as laminae but also in columns.

Below is a description of the organization of the different cortical structures observed across the different scales and how they are integrated to provide a comprehensive understanding of brain connectivity.

1.1.1 Whole brain

Already at the naked eye, mammalian brains appear heterogeneous in size and shape (Figure 1.1). Such diversity at the macroscale foreshadows an equally extensive variability at the microscale. Nevertheless, it is possible to categorize these variations in an attempt to better understand the underlying principles that govern both these similar (similar components and organization across species with only small variations) and unique (inter-individual variability within species) systems. For instance, at the macroscale the mammalian brain can be divided morphologically into two categories: the lissencephalic (smooth) and the gyrencephalic (folded) brains. We can then wonder about what kind of biological advantages give rise to gyrification. It has been proven that an increase in cortical folding correlates with an increase in cortical surface area, more than expected for a smooth brain of the same volume (Toro 2012). Furthermore, a larger cortical surface supports a higher cortical complexity, including an increase in number of cortical regions and connections (Krubitzer 2009), e.g. the mouse has approximately 30 cortical areas (Dong and The Allen Institute for Brain Science 2008), the monkey approximately 90 (Markov et al. 2014a) and the human 180 (Glasser et al. 2016). Therefore brains with larger cortices and more neurons (mouse: 71 million, macaque monkey: 6376 million, human: 86000 million) should have an enhanced processing power (Herculano-Houzel 2009) and can thus execute more elaborate tasks such as higher cognition.

1.1.2 Region/parcellation

Brain parcellations are a tool for generalizing as well as simplifying this complex system by partitioning the brain in coherent populations of cells (mesoscale) (Sporns, Tononi, and Kötter 2005).

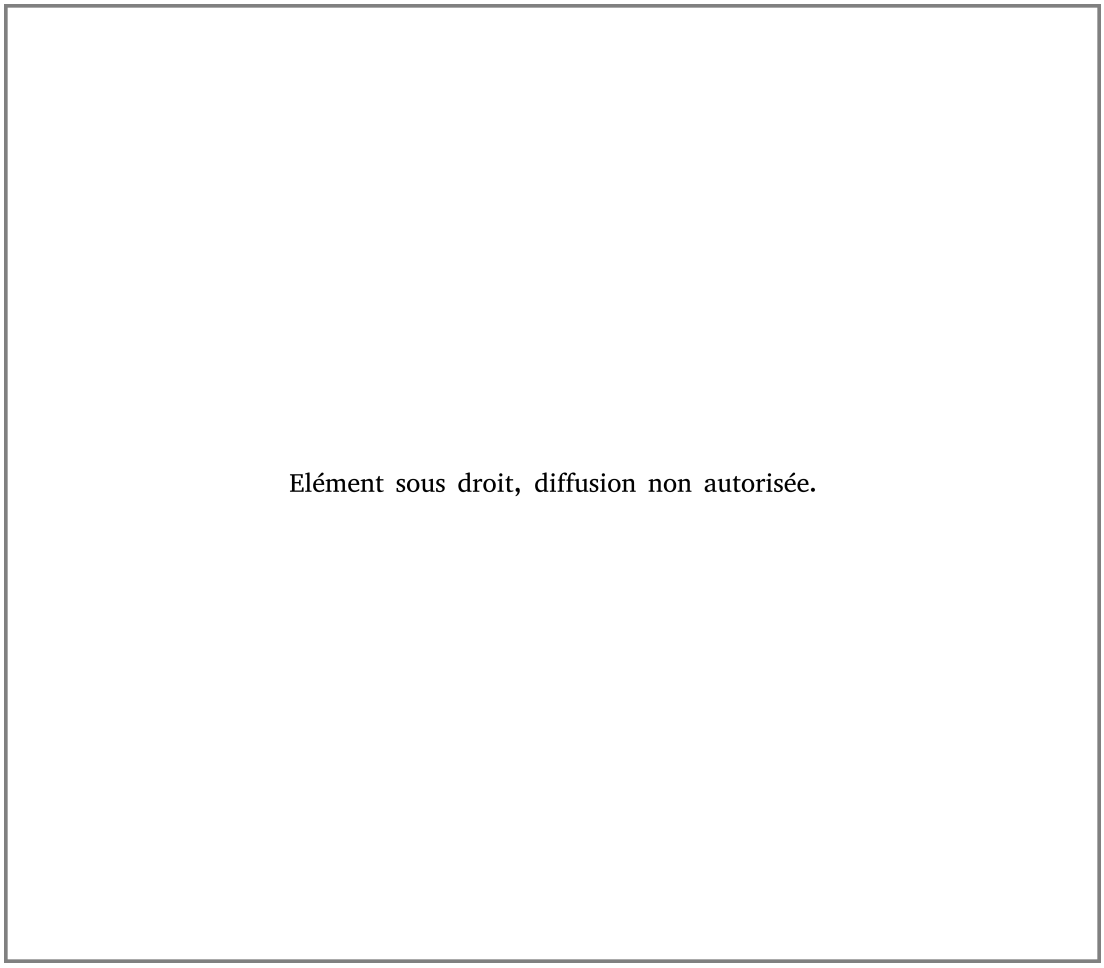

Figure 1.1: Figure 1 from Toro 2012. "**Diversity of the mammalian brain shape.** Lateral aspect of various mammalian brains, drawn at the same scale. Based on images from http://brainmuseum.org" Toro 2012

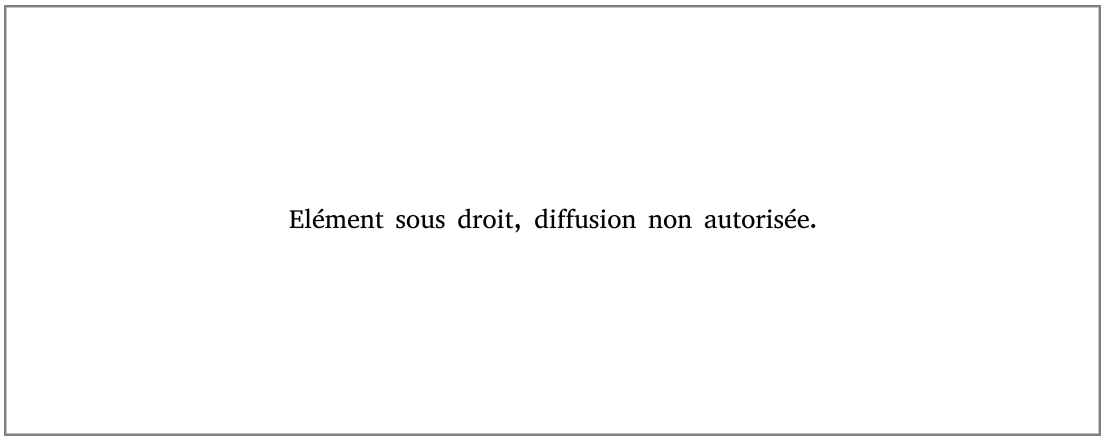

Figure 1.2: Figure from Brodmann 1909. **Brodmann's cytoarchitectonic parcellation.**

Since the early 1900s scientists have been trying to delineate a set of coherent brain regions across mammals. The traditional method for defining brain regions is by common cellular organization (cytoarchitecture) (Figure 1.2) (Brodmann 1909; Economo and Koskinas 1925). However the precision of parcellations is limited, as these methods are not only performed on a small sample size but the techniques are highly invasive and time consuming, which makes it an unsuitable solution for *in vivo* parcellations.

Scientists have since used alternative criteria and techniques for parcellating the brain. The brain has been often parcellated in terms of functional regions, which were first defined using the symptoms from patients with brain lesions and later on using non-invasive techniques such as functional magnetic resonance imaging (fMRI). Brain regions can also be defined following the pattern of brain folding (MarsAtlas; Auzias, Coulon, and Brovelli 2016); by similarity of structural or functional connectivity (Craddock et al. 2012) or a combination of the above (Glasser et al. 2016). These sets of brain regions, often called brain parcellations or brain atlases, comprise of approximately 30 cortical parcels for the mouse brain (Dong and The Allen Institute for Brain Science 2008) and extend to approximately 180 parcels for the human brain (Glasser et al. 2016) as mentioned above.

Although there are a number of accepted brain parcellations for commonly studied mammals like the human (Brodmann atlas; Brodmann 1909, Von Economo atlas; Economo and Koskinas 1925, Talairach atlas; Talairach and Tournoux 1988, MNI atlas; Collins et al. 1995, AAL atlas; Tzourio-Mazoyer et al. 2002, Desikan-Killiany atlas; Desikan et al. 2006), monkey (M132 atlas, Markov et al. 2014b) or mouse (Allen mouse brain atlas; Dong and The Allen Institute for Brain Science 2008), there is no agreement upon one common framework. Moreover, the delineation of such parcellations can influence analysis and results when modelling brain dynamics and structural connectivity (Messé 2020; Wu et al. 2019). In order to avoid the influence and bias of the choice for a specific brain parcellation, especially in more novel animal models, other strategies have been developed to overcome the lack of parcellations. One such strategy is to use random parcellations or to renounce using sharp boundaries and consider gradual variations across the whole brain (Horton 2000). This enables researchers to obtain an objective framework independent from any data type.

1.1.3 Lamination

At the microscopic scale, one can observe a heterogeneous repartition of cells across the cerebral cortex. Most noticeable, is a rostro-caudal increase in neuron density (Charvet, Cahalane, and Finlay 2015). This translates to sensory areas such as the visual cortex being more densely populated (primate; Collins et al. 2010, mouse; Herculano-Houzel, Watson, and Paxinos 2013).

When one examines the brain at a microscopic level, we can observe that it is arranged into layers, which we call lamination. The cortex usually consists of six layers (Economo 2009). The outermost layer (closest to the pial surface), layer I, is very sparsely populated, while layer IV (when it exists) is thin but the most densely populated layer. The overall variations in thickness and density of these cortical layers can be described from agranular to eulaminate. Agranular areas are mainly composed of three layers (layer I, layer II-III and layer V-VI). Dysgranular areas have a poorly defined layer IV and eulaminate areas have six clearly defined layers (Figure 1.3, Dombrowski, Hilgetag, and Barbas 2001). Furthermore neuronal density is often used as a proxy for cortical lamination as the two are positively correlated (Figure 1.3, Dombrowski, Hilgetag, and Barbas 2001). It is the variations of density, cell type and layer thickness that have enabled Brodmann to define his atlas. These layers can be further described in terms of cortical columns (vertical ensemble of interconnected cells) or cell types, however these scales are beyond the scope of this thesis.

In sum, the cortex can be classified according to different laminar profiles, based on neuronal density and this in turn allows us to organize the cortex into different brain regions. In order for this complex system to function as one coherent organ, the previously described entities need to form connections and interact. By using different experimental modalities and examining the brain and its connections across different scales, one can observe how these entities are interrelated.

1.2 Multimodal - how are different entities of brain structure connected ?

The different entities composing the brain (parcels, laminar layers, cells) are interconnected via axons travelling through the white matter (WM). These connections can be imaged at different scales: axon per axon (microscopic) or as bundles of axons (macroscopic). In this work we will describe and use two modalities; tract-tracing with images at the microscopic scale and diffusion weighted imaging at the macroscopic scale.

1.2.1 Tract-tracing

The neuronal bodies (cell somas) originating in the grey matter are connected via axons traveling through the white matter. These cell to cell connections can be quantified using histological tracers (Bizley et al. 2015; Bota, Sporns, and Swanson 2015; Markov et al. 2014a; Zingg et al. 2014). For retrograde tracers, the tracer is injected in the target region and travels back along the axons and sets in the neuronal cell bodies at the source region, where it can

Figure 1.3: Figure 10 from Dombrowski, Hilgetag, and Barbas 2001. **Sketch of the cytoarchitectonic types described in terms of lamination and neuronal density (Nissl stain).**

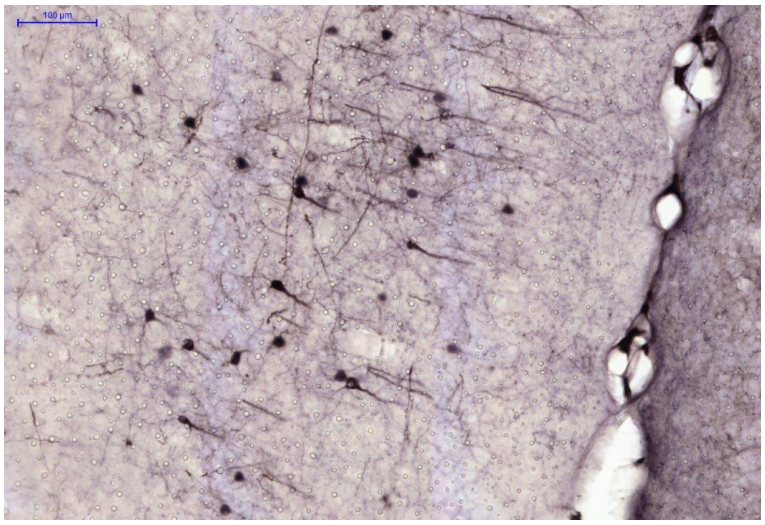

Figure 1.4: **BDA staining of neuronal cell bodies from tract-tracing experiments in the ferret.**
Courtesy of Dr. Leigh-Anne Dell.

be visualized via histochemistry (Figure 1.4). Thus, each labelled neuron is identified as a source neuron connected to the target region where the tracer was injected. Inversely, this method can function as an anterograde tracer, where the tracer travels from the injection site and source region to the target region, labelling the connecting axons at the target region. To date, tract-tracing techniques are still considered the gold standard for quantifying structural brain connectivity as it enables one to observe and quantify each physical connection between pairs of brain regions at the microscopic scale. Although it is considered the most reliable technique, it is highly time consuming and invasive as it requires sacrificing numerous test subjects per brain region injected. Hence this method is unsuitable for human or longitudinal studies.

1.2.2 Diffusion MRI

At the macroscopic scale, whole brain structural connectivity can be imaged using diffusion weighted magnetic resonance imaging (dMRI). dMRI records the gradients of diffusion of the water molecules which are constrained by the axonal architecture. The reconstruction of these gradients of diffusion of the water molecules (tractography) serve as a proxy to estimate the position of axonal fibre bundles travelling through the brain (Jeurissen et al. 2017). These fibre bundles, also called streamlines, are considered to correspond to the main connection pathways, composed of densely packed axons. Most importantly, this technique is non-invasive and allows one to obtain whole brain connectivity, at potentially different time points. Even with advantageous features such as non-invasive, *in vivo* imaging of whole-brain connectivity, the accuracy of diffusion tractography is still highly debated and subject to a number of limitations, such as containing a high number of false positives (Maier-Hein et al. 2017; Jones, Knösche, and Turner 2013; Thomas et al. 2014; Schilling et al. 2018) and the difficulty to track crossing fibers (Tournier, Calamante, and Connelly 2012; Dell'Acqua and Tournier 2019). However most tractography algorithms recover about 90% of the expected fiber bundles, they also all track at least as many invalid bundles (Maier-Hein et al. 2017).

It is therefore necessary to examine the tradeoff between specificity (tracking only existing fibers) and sensitivity (tracking all existing fibers) and prioritize specificity as false positives can have a strong impact on network topology (Zalesky et al. 2016). Moreover, the first tractography algorithms using tensor models were only capable of tracking the main fiber orientation at a given position (only one fiber orientation at a given position possible)(Basser et al. 2000). Most recent implementations privilege models based on spherical deconvolution in order to resolve ambiguous fiber topologies such as crossing, bending, fanning or kissing fibers (Tournier, Calamante, and Connelly 2012; Dell'Acqua and Tournier 2019). Therefore, both modalities (tract-tracing and diffusion MRI) are essential to obtain a global perspective of brain connectivity.

1.3 Brain connectivity - how does whole brain knowledge improve understanding function and behaviour ?

1.3.1 Cytoarchitecture and structural connectivity are essential for brain connectivity and function

The grey matter (GM) and white matter (WM) are essential for whole brain connectivity (Friedrichs-Maeder et al. 2017). The neuronal organization and structural connectivity have been shown to be correlated in the mouse (Goulas, Uylings, and Hilgetag 2017), cat (Beul, Grant, and Hilgetag 2015), monkey (Beul, Barbas, and Hilgetag 2017) and human (Goulas et al. 2016). Studies have shown that it is possible to predict the existence or absence of connections between a pair of regions based on their difference in cytoarchitecture and their relative spatial position (Beul, Barbas, and Hilgetag 2017; Beul, Grant, and Hilgetag 2015). Thus, regions of similar cytoarchitecture and in closer proximity to each other are more likely to be connected than regions that are dissimilar in structure and spatially distant.

Moreover, the structural organization (cytoarchitecture and structural connectivity) of the brain is the basis for functional brain dynamics which underlie cognition and behavior (Park and Friston 2013). In 1992, Roe and colleagues performed an experiment aimed at confirming the influence of connectivity on brain function (Roe et al. 1992). Specific lesions were performed on the visual and auditory cortex of newly born ferrets in order to provide visual inputs to cells in the auditory cortex. After the full development of the ferrets, the authors observed functional similarity in the auditory cortex cells when compared to cells in the primary visual cortex. This underscores the fundamental role of brain structural connectivity in defining the function of a cortical area.

1.3.2 A disruption in brain structure impacts brain function and behavior

The fundamental role of structural brain connectivity can be further observed by the impact that a disruption in its organization can have on brain function and behavior. In the case of brain lesions in humans, white matter disconnections were shown to better predict neurological impairments than the location of the lesion (Schotten, Foulon, and Nachev 2020). The work of Thiebaut de Schotten and colleagues suggests that brain functions should rather be assigned to WM connections than to cortical areas. This emphasizes the importance of

structural brain connectivity and its direct link with brain function and translation of lesion-symptom mapping.

Early cerebral development is a critical phase for organizational and structural processes (Guarnieri et al. 2018; Rahimi-Balaei et al. 2018). Such processes, which include neuronal migration, synaptogenesis, cortical folding, the emergence of thalamo-cortical connections as well as myelination are all prone to organizational disruptions (Rogers et al. 2018). Prematurity in humans and hence the early interruption of in utero development results in 30% of the cases of neurodevelopmental impairments, and this risk continues to increase as gestational time is shortened (Rogers et al. 2018). More specifically, disruptions in the white matter tracts have been observed in a number of neurodevelopmental disorders such as autism spectrum disorder, attention deficit/hyperactivity disorders (Dennis and Thompson 2013).

Therefore it is essential to better characterize the development of the brain structure in order to better identify and understand disruptions from the typical developmental trajectories causing neurological impairments and disorders.

Brain connectivity is studied using various animal models such as mice (Zingg et al. 2014), rats (Bota, Sporns, and Swanson 2015), cats (Hilgetag and Grant 2010), macaques (Pandya et al. 2015) or marmosets (Atapour et al. 2019), in the quest of obtaining data to translate experimental studies to humans. Despite the amount of knowledge gathered in these studies, these species present structural or practical limitations for studying human development. Mice and rats have a lissencephalic brain (Toro 2012). The marmoset has a long gestation period (144 days) (Tardif et al. 2003) and in general cats and primates are protected by numerous ethical considerations. Thus other animal models need to be explored. Such models should not serve to replace current animal models, from which we have gained invaluable insights, but rather to supplement and enrich our current understanding of brain development and connectivity across mammals. Consequently, this work will use the ferret as its model for examining brain development.

1.4 The ferret as animal model for brain connectivity and development

In this work on the development of brain connectivity we use the ferret (*Mustela putorius furo*) as our animal model. The ferret was introduced over 40 years ago as an animal model for studying influenza (e.g. Arroyo and Reed 1977). It continued to gain popularity as scientists discovered that it is one of the smallest mammals with a gyrified (folded) brain, thus a possible model to understand brain gyrification. Furthermore, its small size, sociability and short gestational duration (42 days) make ferrets inexpensive to house for experiments (Fox 1998).

Brain gyrification is considered an indicator of a more complex brain, as folding induces a significant increase in cortical surface area (Toro 2012) and number of neurons which allows more cortical complexity (Herculano-Houzel 2009). The ferret brain is a good intermediate between the mouse which has a lissencephalic (smooth) brain and human with a highly complex brain and thus a good translational model for studying brain development and gyrification (Reillo et al. 2011). Moreover, the ferret is born with a very immature and lissencephalic

brain that undergoes gyrification postnatally (Figure 1.5). Drastic changes in brain morphology and cellular organization have been observed in neonatal ferrets (Smart and McSherry 1986a; Smart and McSherry 1986b; Neal et al. 2007). Such postnatal folding and maturation allow us to witness and examine, postnatally, brain developmental events and processes that happen during gestation in humans (Clancy, Darlington, and Finlay 2001). Additionally, these phenomena can be conveniently imaged at higher resolutions in the ferret for optimal analysis and comparison of brain folding mechanisms.

Recently, the ferret has been used as a model for studying WM brain injuries caused by birth prematurity in humans in order to understand the consequences of white matter dysmaturation on pathological and motor deficits (Wood et al. 2018; Snyder et al. 2018). Furthermore, the ferret is also used to study the visual and auditory cortical development and the effects of external stimuli on brain development (Lempel and Nielsen 2019; Bizley and King 2009), specifically as eye and ear opening occur much later (around one month of age) (Fox 1998).

In closing, although humans are the ideal and desired experimental subject, numerous ethical considerations make human research difficult. Thus animal models, such as the ferret, play an important role in human brain research and require better characterization.

1.5 Ferret brain development

The ferret brain undergoes dramatic changes during the first month after birth. One such change, already visible at postnatal day 10 (P10) (Figure 1.5), is the transition from a lissencephalic cortex to a gyrencephalic cortex. By 4 weeks after birth the cortical layers are formed (Voigt, De Lima, and Beckmann 1993) and by 2 months of age the cortical cytoarchitecture can not be differentiated from that of a 2 year old ferret (Jackson, Peduzzi, and Hickey 1989). Neurogenesis and neuronal migration in the visual cortex begin at embryonic day 20 (E20) and finish around postnatal day 14 (P14) (Jackson, Peduzzi, and Hickey 1989).

The neuronal proliferation follows an inside-out pattern of development, seen in all mammals i.e. the deepest layer, layer VI, is completed first then layer V, layer IV and layer II/III. Layer I is the only exception which develops in two phases between E20 and E30 and between P1 and P14 in the visual cortex (Jackson, Peduzzi, and Hickey 1989). Synaptogenesis starts as soon as the neurons have completed their migration and follows the same inside-out pattern of development until the end of neuronal migration (P14) (Voigt, De Lima, and Beckmann 1993). In addition, synaptogenesis and neurogenesis follow a rostro-caudal and laterodorsal gradient of development (Voigt, De Lima, and Beckmann 1993). Dendritogenesis is shown to follow the same two patterns of development (inside-out and rostro-caudal/laterodorsal) (Zervas and Walkley 1999). Furthermore, dendritogenesis starts in layer V at P1 and peaks at P21, while in layer II/III it starts at P14 and peaks at P28 (Zervas and Walkley 1999).

Glia (including astrocytes, oligodendrocytes and microglia) are present in the intermediate zone (future WM) from E28 to P59 with a peak at P1 as well as appearing in the cortical plate at P4 (Berman, Johnson, and Klein 1997). More specifically, radial glia fibers are abundant at birth and rapidly increase until P14 after which they strongly decrease by P21 (Voigt 1989; Reillo et al. 2011).

Two weeks postnatally appears to be a key time point for changes at both the microscopic and macroscopic levels as the brain transitions from neuronal proliferation to cellular differentiation (Knutsen et al. 2013). Furthermore, at the macroscale, the cortical surface transitions to

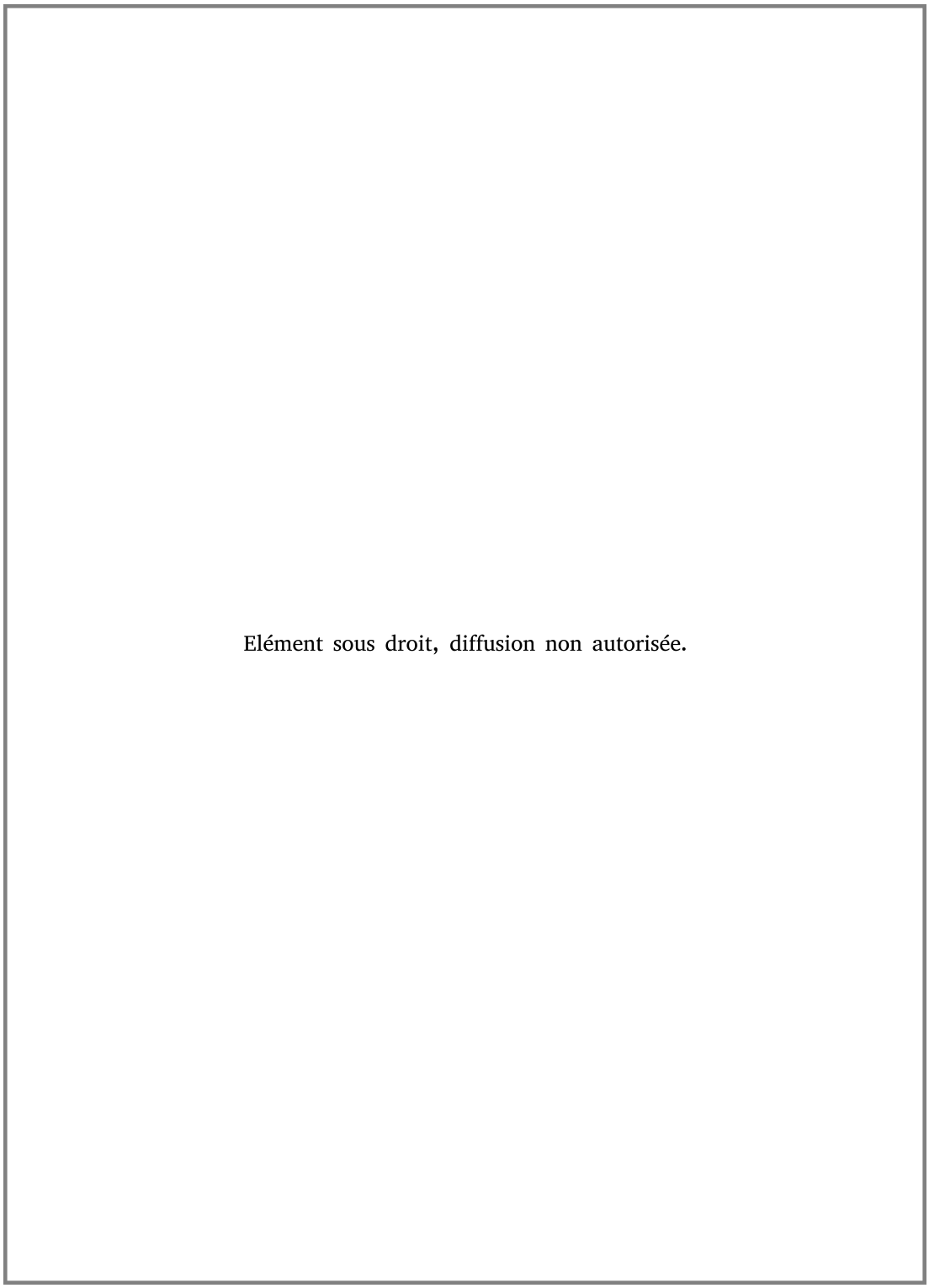

Figure 1.5: Figure 2 from Sawada and Watanabe 2012. "**Dorsal views of brain of male ferrets on postnatal days (PD) 4 to 90.**" Sawada and Watanabe 2012

a faster rate of extension and undergoes a phase of faster folding (increase in curvature and sulcal depth between P10 and P17) (Knutsen et al. 2013), however overall folding occurs from P4 to approximately P30. The brain continues to elongate until 2 months postnatally (Smart and McSherry 1986a; Barnette et al. 2009; Sawada and Watanabe 2012). Finally, myelination onset has been identified postnatally between week 5 and 6 (Barnette et al. 2009).

1.6 Overview of the performed studies

In this work we used a multi-scale and multimodal approach to characterize the development of the ferret brain cytoarchitecture and structural connectivity. A first aim of this thesis was to compare diffusion-based connectivity data with connectivity data derived by traditional histological approaches in the adult ferret. A second aim was to analyse Nissl stained histological slices to characterize the maturation of cytoarchitectonic lamination in the first postnatal month of development of the ferret. A third aim was to investigate the relationship between the organization of connectivity and cytoarchitecture and its evolution during early brain development.

Chapter 2

Datasets and data processing pipelines

In this section we described the main datasets that were used in the following analysis, namely MRI scans, especially diffusion MRIs and histological slices. These two datasets were acquired in the context of the FIIND project and first processed in the context of this thesis. The data was made available to the scientific community via the following website https://neuroanatomy.github.io/fiind/ .

The acquisition of these images and their processing was described in this section. The specifics for each of the analyses were mentioned in the corresponding chapters.

2.1 MRI acquisitions

The MRI dataset underlying the following studies was composed of T2-weighted magnetic resonance images (MRIs) and diffusion magnetic resonance images (dMRIs) from ferrets aged 4 days old (P4 – postnatal day 4), P8, P16, P32 and adult. The T2-weighted MRIs imaged brain morphology while dMRIs were a proxy for brain connectivity.

The following paragraphs are based on the previously published article Delettre et al. 2019.

2.1.1 Brain preparation

The acquisitions were performed *post mortem* in order to improve sensitivity (Holmes et al. 2017). The ferrets were euthanized by an overdose of pentobarbital and perfused transcardially with 0.9% saline solution and post-fixed with phosphate-buffered 4% paraformaldehyde (PFA). After extraction, the brains were stored at 4°C in a 4% PFA solution until the MRI acquisition. All procedures were performed in Victor Borrell's lab and approved by the Institutional Animal Care and Use Committee of the Universidad Miguel Hernández and CSIC (Consejo Superior de Investigaciones Científicas), Alicante, Spain.

The brains were transferred to a 0.01 M phosphate-buffered saline (PBS) solution for rehydration 24 hours before MRI acquisition. Shortly before MRI acquisition, the brain samples were transferred to a plastic tube filled with non protonic liquid (fluorinert) in order to avoid air-tissue interfaces that may induce susceptibility artefacts. The tube was then placed in a dedicated holder in the middle of the transmit/receive MRI volume radiofrequency coil. Temperature stability was ensured by a regulated room temperature as well as the cooling of the gradient coils, by water at 16°C that was constantly flowing inside the innermost part of the magnet. The equilibrium temperature at the sample was 20°C. High resolution MRI were acquired *ex vivo* using a small animal 7 Tesla Bruker MRI scanner (Neurospin, Saclay, France).

2.1.2 Structural MRIs

High-resolution T2-weighted MRI data were acquired using a multislice multi-echo (MSME) sequence with 18 echo times and 0.12 mm isotropic voxels. The T2-weighted images served as a base in order to segment the brain at the pial surface as well as the white matter surface, including a precise delineation of the sulci and gyri.

2.1.3 Diffusion MRIs

Diffusion MRI data were acquired using a multislice 2-D spin-echo segmented DTI-EPI sequence (4 segments) and the following parameters: 0.24 mm isotropic voxels; 200 diffusion-weighted directions with b = 2000 or 4,000 s/mm^2 ; and 10 b0 at the beginning of the sequence, diffusion gradient duration = 5 ms and diffusion gradient separation = 17 ms (the detailed parameters available in Table 2.1). Thanks to strong gradients compared with clinical scanners, the b-value could reach 2,000 or 4,000 s/mm^2, ensuring a strong diffusion

Ferret age (postnatal day)	4	8	16	32	Adult
b-value (s/mm2)	4000	4000	2000	2000	4000
# b-vecs (+B0)	200+10	200+10	200+10	200+10	200+10
TR (s)	20	12.5	18.75	17.5	40
TE (ms)	30	35	80	80	32
Matrix size	120x50x40	100x70x50	200x100x75	175x96x70	160x120x80
Voxel size (mm)	0.24	0.24	0.24	0.24	0.24
Diffusion gradient duration (ms)	5	5	5	5	5
Diffusion gradient separation (ms)	17	17	17	17	17
Scan time (hours)	9	11	17	16	37
SNR	2.7	4.4	9.6	6.4	4.2
# directions removed	8	11	12	11	3

Table 2.1: **Parameters of the diffusion MRI acquisitions.**

weighting and therefore an improved sensitivity to anisotropy while keeping the echo time low enough to save signal-to-noise ratio (SNR) and limit EPI distortions. A b-value of 4,000 s/mm^2 has been previously shown to be a good compromise for disentangling crossing fibers for *ex vivo* imaging (Dyrby et al. 2011). The noise introduced by the high diffusion weighting was balanced by a high angular resolution. The 200 directions were generated as non collinear directions uniformly distributed over a sphere (Hasan, Parker, and Alexander 2001). The spatial resolution was chosen as the highest resolution available on the scanner in order to achieve a good SNR while keeping a reasonable acquisition time. We obtained an SNR between 2.7 and 9.6 (Table 2.1), measured as the ratio between the mean of our signal in the brain and the standard deviation of the signal in the background. The total acquisition time of the diffusion MRI sequences was up to 37 hours (Table 2.1). Imaging was performed at Neurospin, CEA.

2.2 MRI processing

2.2.1 Structural MRI segmentation, brain masks

A brain mask was manually segmented from the high-resolution T2 image, in order to obtain a precise delineation of the sulci and gyri. The outline of the pial surface was delineated using a combination of automatic and manual tools. The segmentation was performed using an online tool, BrainBox (Heuer et al. 2016). The inner surface of the neocortex and white matter surface were also segmented following the same procedure. Spatial normalization using a linear transformation between the high-resolution T2 volume and diffusion MRI data was computed using FLIRT tools (Jenkinson et al. 2002), and the brain masks were registered to the diffusion space.

2.2.2 dMRI preprocessing

First, dMRI data were converted from the 2dseq bruker format to the standard NIFTI format using a modified version of the bruker2nifti script (original version: https://github.com/

SebastianoF/bruker2nifti; modified version: https://github.com/neuroanatomy/bruker2nifti). For a limited number of volumes, EPI trajectories were poorly corrected, by the Bruker routine image reconstructor, which resulted in noisy volumes. In order to exclude these volumes, diffusion-weighted directions for which their mean signal was two standard deviations away from the global average across all the volumes were visually inspected and removed. Three to twelve out of 200 volumes were removed following this criterion (Table 2.1). The preprocessing steps were mainly done using MRtrix3 functions and included: a local principal component analysis (LPCA) denoising (Veraart et al. 2016), Gibbs ringing correction (Kellner et al. 2016), FSL-based eddy current correction (Jenkinson et al. 2012; Andersson and Sotiropoulos 2016) and B1 field inhomogeneity correction (Tustison et al. 2010).

2.2.3 dMRI tractography

We considered three local models: (1) the diffusion tensor (DT) model; (2) fiber orientation distribution (FOD) estimated with a constrained spherical deconvolution (CSD) using the tournier algorithm (Tournier, Calamante, and Connelly 2013); and (3) FOD estimated with the multi-shell multi-tissue CSD (msmt CSD) using the dhollander algorithm, which provides an unsupervised estimation of tissue specific response functions. The msmt CSD was performed using a WM/CSF compartment model (Jeurissen et al. 2014). Each of the three tractography models was then paired with a deterministic and a probabilistic tracking algorithm. Deterministic DT-based tracking was performed using Euler integration (TensorDet; Basser et al. 2000, while DT-based probabilistic tracking used bootstrapping (TensorProb; Jones 2008. CSD-based tractography was performed according to FOD peaks either deterministically (SD_STREAM; Tournier, Calamante, and Connelly 2012 or probabilistically (iFOD2; Tournier, Calamante, and Connelly 2010. A spherical harmonic order of 8 was used for CSD-based estimations. One million streamlines were tracked over the full brain with the parameters recommended by MRtrix3: stepsize 0.024 mm (0.12 mm for iFOD2), angle 90° per voxel (45° for iFOD2), minimal streamline length 1.2 mm, maximal length 2.4 cm. Streamline seeds were produced at random locations within the brain mask until the defined number of streamlines was reached. To prevent streamlines from going across sulci, the brain mask was used as a stopping criterion.

2.2.4 Tractography based connectivity matrices

Structural connectivity matrices were extracted from the tractography results using the number of streamlines connecting pairs of regions. Matrices reporting the averaged fiber lengths between regions were also computed. Then, structural connectivity matrices were normalized using fractional scaling, such that the number of streamlines between pairs of regions were divided by the sum of the streamline counts connected to each of the regions, excluding self-connections (Donahue et al. 2016). The weights then represent the fraction of streamlines (FS).

All MRI data analysis was performed using the MRtrix3 software (https://www.mrtrix.org/), and custom scripts for Python (https://www.python.org), including python packages Nipype (Gorgolewski et al. 2011), Nibabel (Brett et al. 2018) and Numpy (Oliphant 2015; Harris et al. 2020).

2.3 Histological sections

The second key dataset in this work was composed of a set of histological slices of the ferret brain stained for Nissl substance. Nissl stains cell bodies (neurons and glia) in the tissue section. The dataset was composed of ferrets aged P4, P8, P16 and P32. This allowed us to describe the cytoarchitectural organization of the developing ferret cortex.

The description about the brain preparation can be found in the previous section 2.1.1 'Brain preparation'.

2.3.1 Histological data preparation and staining

The original dataset was composed of five time points: P0 (birth), P4, P8, P16 and P32 with four subjects per time point, however in this thesis, only one individual per time point could be included due to complications during the digitalization of the sections. Moreover, the P0 time point was also excluded as no dMRI scan could be acquired with a sufficient SNR. The neurohistology was performed by the NeuroScience Associates (NSA), using MultiBrain® Technology. The brains were embedded in four independent blocks. The first block included the four P0 brains and four P4 brains. The second block included the four P8 brains and four P16 brains. The four P32 brains were embedded in the third block. The blocks were cryo-sectioned at 40 microns (30 microns for the block containing the P0 and P4 brains) in the coronal plane through the entire brain. All sections were collected into a series of 24 wells containing antigen preservation solution. Every 8th (6th for the block with P0 and P4 brains) section was stained with Thionine (Nissl), marking cell bodies.

2.3.2 Digitalization

The slides were digitized using a slide scanner, Zeiss AxioScan Z1 and the ZEN software. The digitalisation was performed in collaboration with David Briand and David Hardy from the Experimental Neuropathology lab at the Institut Pasteur.

The full slides were scanned at magnification 20X (0.22 um/pixel), using brightfield imaging and no Z-stack (in order to keep manageable files). Thus, we obtained high resolution digital slides which allowed us to process and extract whole brain data with a minimal amount of manual input. The following semi-automated processing pipeline ensured a higher reproducibility and a shorter processing time.

2.4 Histological data processing

2.4.1 Histological data pre-processing (registration and extraction)

The original .czi images from the ZEN software were converted to the BigTiff format using a CZI to TIFF converter.

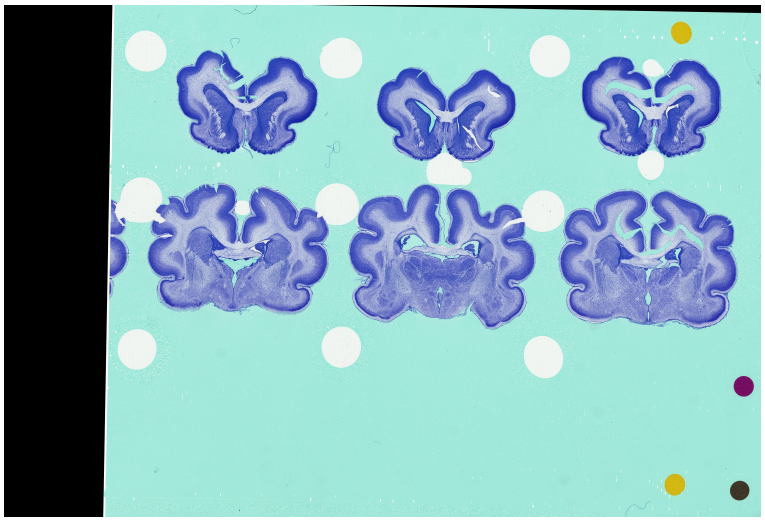

Figure 2.1: **Digitized Nissl brain section.**
Brain sections from P8 and P16 ferrets. The yellow, purple and black circles were used as landmarks for the registration of the slices.

The following pre-processing pipeline was implemented using Python (www.python.org) and Vips (https://github.com/libvips/libvips). The sections were registered using the micropillars for the sectioning of the gel block (yellow, purple and brown circles on the sections) as landmarks (Figure 2.1). The first template landmarks of each block were cropped out of the first section. These landmarks were then identified in the following sections using skimage.feature.matchtemplate (Walt et al. 2014) and registered to their position in the reference image (the first section if the landmarks were identifiable). In order to reduce computation time, the transformation matrices were computed on the images with a resolution scaled down to 2% using nudged.estimate (https://pypi.org/project/nudged/). The transformation parameters were then scaled back to the full resolution and the images were transformed using 'vips affine'. The sections which did not pass the automated registration, were visually checked and manually registered. Finally, the brains were consistently extracted from the registered images using manually set rectangles as field of views (Figure 2.2).

2.4.2 Delineation of pial contours

The registered and cropped images were converted to DeepZoom format (.dzi) and uploaded to the web application Microdraw (https://microdraw.pasteur.fr) for the delineation of the pial surfaces.

The original images were thresholded (hue < 20) in order to compute a first automatic segmentation. The automatically generated contours were imported to Microdraw and manually edited to imporve sulci delineation and remove unwanted (false) contours (Figure 2.3). The contours were then downloaded as polygons (list of consecutive coordinates of points) in json files for further processing.

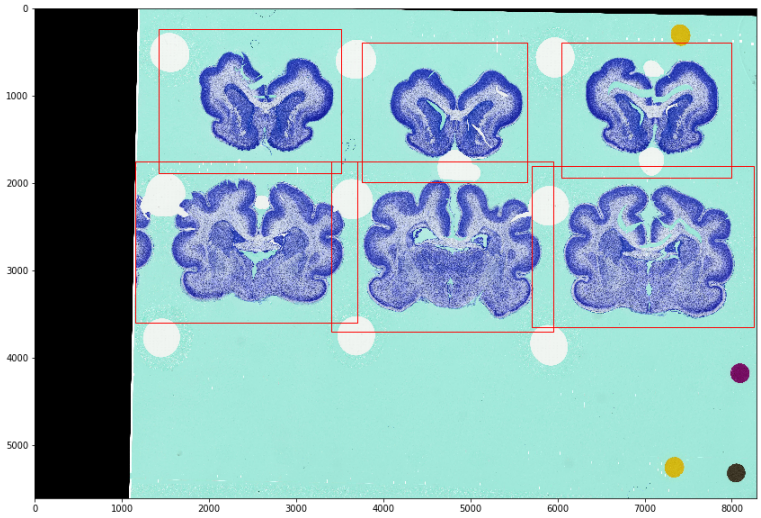

Figure 2.2: **Digitized Nissl brain section with cropping rectangles (red).**

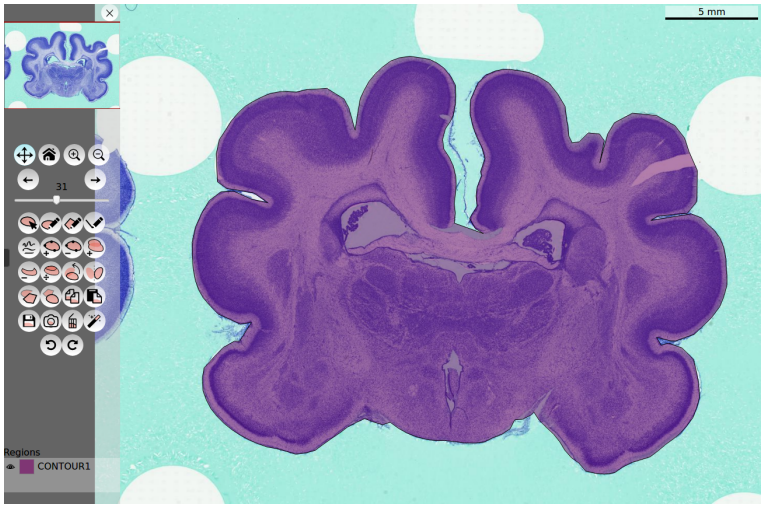

Figure 2.3: **Segmentation of a P16 brain section on Microdraw.**

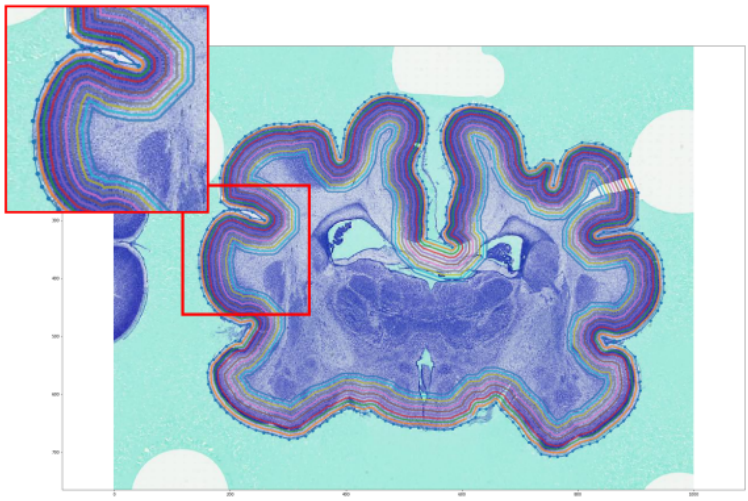

Figure 2.4: **Contour generation of a P16 ferret brain section.**
The outermost contour (blue, with scatter points) is the manually edited contour with Microdraw. The inner contours are automatically generated with pyclipper.

2.4.3 Extraction of grey level profiles

The pial contour segmentation, here also called outer contour, was the sole manual step and basis for the automatic extraction of grey level profiles in the GM. The outer contour was resampled (one node every 300 um) in order to obtain a homogeneous sampling of the cortical surface, after which a number of consecutive concentric contours (further called inner contours) were generated using pyclipper (https://github.com/fonttools/pyclipper) (Figure 2.4).

These inner contours (Figure 2.5, orange points) were aligned node to node with the initial outer contour (Figure 2.5, blue points) using optimal transport alignment (https://dfdazac.github.io/sinkhorn.html). The node to node alignment allowed us to obtain radial profiles, which were the basis for extracting the raw profiles (Figure 2.5, yellow lines). The digitized slices were converted to grayscale and a median filter was applied in order to smooth the local inhomogeneities. The profiles were extracted by the line drawn from the outer contour node to its corresponding node on the inner contour. The raw profiles started at the outer contour and measured 1700 um ensuring to cover the whole depth of the cortex (average cortical depth in the gyral crowns of 1477 um in the ferret aged P90 Horiuchi-Hirose and Sawada 2016).

The raw profiles were then limited to the extent of the GM using the following set of conditions. High values, corresponding to bright areas (layer I, sheers or WM), at the beginning and at the end of the profiles were thresholded out, in order to come as close as possible to the layer I/II and the GM/WM interfaces (Figure 2.6, beginning and end of the piecewise linear fit). The remaining profiles were fitted using a 6-piece piecewise linear function (https://jekel.me/2017/Fit-a-piecewise-linear-function-to-data/) in order to estimate the start position of layer II and the junction between the GM and the WM for each individual profile. Firstly, the steepest negative slope of the two first segments indicated the breakpoint corresponding to the start of layer II so that the lowest point around that breakpoint was chosen as the starting point of the profile (Figure 2.6, first red diamond). Secondly, the end

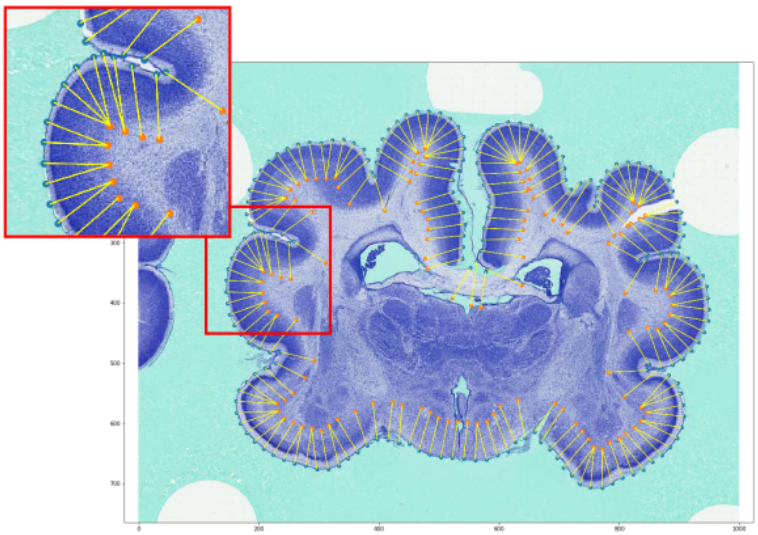

Figure 2.5: **Alignment of the outer and inner contours of a P16 ferret brain section.** The blue points are points on the outer contour. The orange points are points generated from the innermost contour. The yellow line segments indicate the correspondence between the nodes of the two contours and the orientation of the future grey level profiles.

point of the profile was chosen by identifying the maximum positive slope of the last three segments corresponding to the transition from the GM to the WM. Similarly, the lowest point around the breakpoint was selected as the end point of the profile (Figure 2.6, second red diamond). Profiles with lengths under 75 um were considered too short to represent the full cortical depth, as the cortical depth was measured at 255 um at P0 (birth), 1073 um at P14 (Reillo and Borrell 2012) and approximately 1500 um at P90 in the ferret (Horiuchi-Hirose and Sawada 2016). In addition, the profiles lengths two standard deviations away from its neighbors were flagged and excluded, as we expected smooth local variations of the cortical thickness (Figure 2.7). The final profiles were used as a quantitative metric for characterizing the laminar organization of the cortex.

2.4.4 Profile normalization

The profiles were normalized by their length in order to compare the relative variations in thickness of the different layers. In addition, we normalized the profiles by their mean value to minimize the effects of intensity variations which could have been caused by variation in the staining concentration or light variations during the scanning. Finally, we normalized the profiles by their minimum and maximum values to accentuate the variations of intensities along the cortical depth.

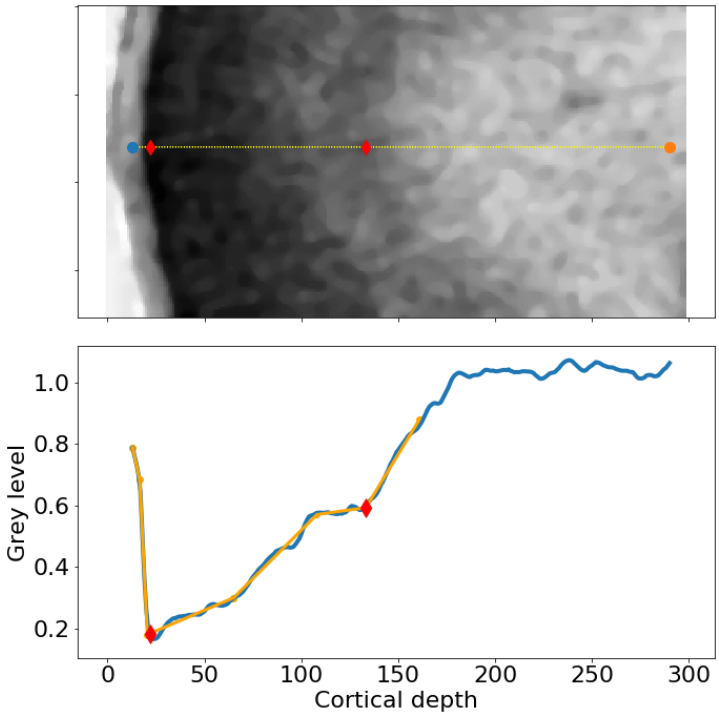

Figure 2.6: **Estimation of the GM borders of the extracted grey level profiles by piecewise linear fit.**
The upper panel represents an extract of a Nissl section with median filter. The blue point is a node from the outer contour. The orange point indicates the other end of the raw grey level profile. The yellow dotted line represents the position of the grey level profile. The lower panel represents the corresponding grey level profile (blue). The x-axis represents the cortical depth (arbitrary unit) and the y-axis represents the grey level (RGB, 0 is black, 255 is white). In orange is the 6-piece linear fit. The red diamonds represent estimated borders of the GM.

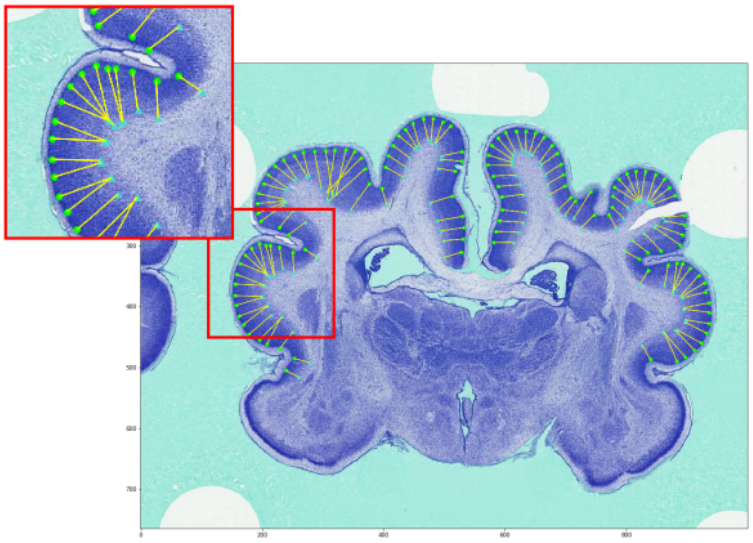

Figure 2.7: **Valid grey level profiles of a P16 ferret Nissl brain section.**
The grey level profiles were automatically generated, limited to the GM and filtered out if too short, with a length two standard deviations away from the average length of their neighbors or on a shear area (white).

2.5 Establishing the correspondence between histological sections and MRI space

2.5.1 2 step 2D registration

In order to obtain a precise correspondence between the MRI data and the histological microimages, we performed a series of 2D registrations.

Each histological slice was first associated with its corresponding slice in the MRI volume. We reported the indices of the most anterior and most posterior part of the brain in both the MRI and the histology datasets and we deduced the corresponding slice index of the histological data in the MRI by means of proportionality. The MRI slices were then registered to the histological slices using ANTs registration (Avants et al. 2011; Tustison and Avants 2013), in a succession of rigid, affine and deformable SyN 2D registrations.

This method allowed a precise slice to slice registration. Furthermore, the deformable registration provided a good sulci and gyri match which was important as the images from both modalities were from different individuals.

The transformation matrix allowed us to translate the histological coordinates to the MRI coordinates. This enabled us to establish the correspondence between each of the profiles and individual nodes in the surface mesh (cf. section 2.5.2 'Surface mesh reconstruction and morphing') to the reference space and hence translate a common parcellation (cf. section 2.5.3 'Random parcellation') across modalities.

2.5.2 Surface mesh reconstruction and morphing

The following paragraph describes the reconstruction and morphing of the meshes to consecutive time points. This pipeline was developed in the lab of Dr. Roberto Toro and will be further described in an article in preparation (Toro et al. in prep).

The pial surfaces of the brain were segmented from the structural MRIs using the online platform Brainbox (Heuer et al. 2016). The segmentations served as a basis for reconstructing the surface meshes using marching cubes and the software Graphite (http://alice.loria.fr/software/graphite). The meshes were then decimated and regularized. The mesh topologies were manually corrected using MeshSurgery (https://github.com/r03ert0/MeshSurgery). The meshes at each of the time points were first matched with each other based on the position of their sulci. The sulci were labelized using Cartographer (https://github.com/r03ert0/stereographic) and a first morphing of the meshes was performed using a spherical version of the Beier and Neely algorithm (https://github.com/r03ert0/spherical-beier-neely). The second automated mapping of the meshes of consecutive time points was performed as a minimization of the local deformations. The deformation field was expressed as a linear combination from a given number of Laplacian eigenvectors of the mesh. The projection between two consecutive time points was performed using spherical meshes. The deformation field was computed as the minimization of the sum of the deformation energy and the smoothness energy. This minimization was computed using the Broyden-Fletcher-Goldfarb-Shanno algorithm (scikit-learn, lbfgs solver, Garreta and Moncecchi 2013). Finally all the meshes from a developmental series were remeshed to have the same topology (i.e. each of the nodes represent the same position across the time points). The developmental mesh series was composed of one set of meshes per time point: in their reference space with their original topology, its spherical equivalent as well as meshes in the morphing space (corresponding nodes across time points) in both the original topology and the spherical equivalent. These four types of meshes allowed us to establish the correspondence between any time points.

The meshes in the morphing space had a direct node to node correspondence across the time points used in the developmental series. The correspondence between the morphing space and the reference space for each of the time points was performed using the spherical topology. This involves finding the closest point on the surface in the reference space of a given node in the morphing space (igl, signed_distance, https://github.com/libigl/libigl-python-bindings). We further computed the barycentric coordinates of that point with regard to its reference triangle. The position of the point in the reference space and the original topology could then be computed using the barycentric coordinates in the corresponding triangle (same index as the spherical mesh in the reference space).

2.5.3 Random parcellation

In order to overcome the absence of ferret atlases across development, we generated random parcellations using the surface meshes in the morphing space (Figure 2.8). An initial random parcellation was generated on the youngest ferret (P4) in its reference space as this surface mesh contained the lowest number of nodes and would allow the transfer of the parcels back up to the adult reference space without losing any parcel. Areas such as the olfactory bulbs and the entorhinal cortex were excluded due to a manual segmentation already performed in the adult ferret following the atlas from Radtke-Schuller 2018. The segmentation was transferred back to the younger ferret using the morphing meshes.

The parcellation generation started with an initial set of N (here N=200) random seed nodes (N/2 nodes per hemisphere). The 200 parcels allowed us to obtain a fine grained parcellation while being able to maintain all the parcels with a minimum of 3 mesh nodes for the smallest mesh at P4. Each node of the surface mesh was assigned to the label of their closest seed node. The seeds were reinitialized if a parcel was composed of less than 3 nodes. The parcellation was then transferred back into the morphing space, passing by the spherical equivalents of the meshes in the reference and morphing space (cf. section 2.5.2 'Surface mesh reconstruction and morphing').

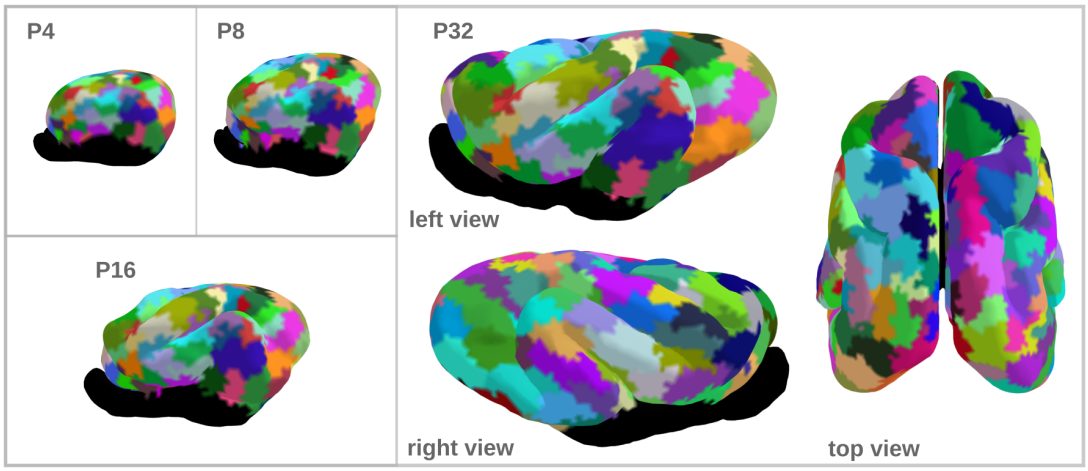

Figure 2.8: **Common 200 parcel random parcellation.**
Representation of the 200 parcel random parcellation at each time point (left views). Left, right and top view of the parcellation on the ferret at P32.

Chapter 3

Comparison between diffusion MRI tractography and histological tract-tracing of cortico-cortical structural connectivity in the ferret brain

This chapter is based on the published article Delettre et al. 2019.

The anatomical wiring of the brain is a central focus in network neuroscience. Diffusion MRI tractography offers the unique opportunity to investigate the whole brain fiber architecture *in vivo* and non invasively. However, its reliability is still highly debated. Here, we explored the ability of diffusion MRI tractography imaging at the macroscale to match invasive microscopic anatomical tract-tracing connectivity data of the ferret brain. We also investigated the influence of several state-of-the-art tractography algorithms on this match to ground truth connectivity data.

3.1 Introduction

Brain function emerges from the communication of spatially distributed large-scale networks via the underlying structural connectivity architecture (Kandel et al. 2012; Varela et al. 2001; Engel et al. 2013; Park and Friston 2013). Systematic analysis of structural connectivity has revealed characteristic features of brain networks, including the presence of modules, hubs and higher-order topological properties, thought to support efficient information processing (Sporns 2010). Moreover, structural connectivity is considered as a neural substrate that is affected in various pathological conditions, such as Alzheimer's disease and schizophrenia spectrum disorders (Fornito and Bullmore 2015). Therefore, reliable estimates of brain structural connectivity are essential for advancing our understanding of the network basis of brain function.

Diffusion MRI tractography is an indirect approach for inferring brain structural connectivity from the brownian motion of water molecules constrained by the axonal fiber architecture (Jeurissen et al. 2017). Thus, it provides the unique opportunity to investigate, *in vivo* and non invasively, the structural connectivity of intact or altered brains, such as in the case of stroke (Visser et al. 2018), in longitudinal analysis of brain development (Hagmann et al. 2010) or in utero acquisitions of prenatal brain structure (Kasprian et al. 2008). However, the reliability of diffusion MRI tractography for properly mapping structural connections remains highly debated (Jones, Knösche, and Turner 2013; Thomas et al. 2014). Therefore, validation appears as a key step in evaluating current methodologies and identifying new perspectives of improvement (Dyrby et al. 2018).

A small number of studies designed benchmarks in order to explore the reliability of diffusion MRI tractography (Schilling et al. 2018). For example, using a phantom dataset composed of known tracts reconstructed by diffusion MRI tractography as ground truth, the accuracy of a large number of state-of-the-art tractography algorithms was assessed in humans (Maier-Hein et al. 2017). The results showed, for all the algorithms, their ability to recover most of the existing bundles, but also revealed a variable, but substantial, number of false positives. Similarly Sarwar, Ramamohanarao, and Zalesky 2019 compared deterministic and probabilistic tractography algorithms with a numerically generated phantom and concluded on a trade-off to be made between sensitivity and specificity depending on the type of tractography algorithm. While these studies provided a first estimate of the specificity and sensitivity of a wide range of tractography algorithms, the ground truths used were based on diffusion MRI tractography or numerically generated and thus one can debate their realism.

To date, the gold standard for assessing structural brain connectivity is provided by tract-tracing experiments, which physically investigate, at the cellular level, the relative number of connections of an area to the rest of the brain using viral, bacterial or biotinylated dextran agents (Zingg et al. 2014; Markov et al. 2014a; Bota, Sporns, and Swanson 2015; Bizley et al. 2015). These agents act as either anterograde or retrograde tracers. Such histological tracing of anatomical connections provides directional (as well as laminar) information on projection. In the case of retrograde tracing, histological tracing also quantifies the number of axons in a projection, since each labeled projection neuron provides one axon. Studies performed in macaque (Donahue et al. 2016; Zhang et al. 2018; Azadbakht et al. 2015; Schilling et al. 2019b), squirrel monkey (Schilling et al. 2019a; Gao et al. 2013), pig (Knösche et al. 2015), mouse (Calabrese et al. 2015) and rat (Sinke et al. 2018), have explored the relationship between tract-tracing experiments and tractography. Overall these studies have shown that diffusion MRI tractography provides a good estimate of structural brain connectivity. Few explorations

have been made on the ability of the different tractography approaches available to estimate structural connectivity weights (Gao et al. 2013). Previous studies have mainly focused on the ability of tractography algorithms to properly estimate white-matter pathways by means of voxel-wise overlap (Knösche et al. 2015), or on the detectability (presence or absence) of connections (Sinke et al. 2018), or both (Schilling et al. 2019b; Schilling et al. 2019a).

The ferret brain starts to fold after birth, and reaches the adult folding pattern at about one month of age. Therefore, the ferret is a widely used animal model for studying brain folding (Barnette et al. 2009; Feng et al. 2013). Furthermore, these mammals display complex behavior, are inexpensive to house and have a short gestation period as well as a limited life time, making them an attractive 'whole lifespan model' (Fox 1998). Recently established extensive tract-tracing connectivity data of the ferret (Dell et al. 2019a; Dell et al. 2019c; Dell et al. 2019b) have made it possible to compare anatomical cortical connectivity with that reported by tractography methods. Thus, the present study aimed to use the ferret as an animal model to assess the performance of six diffusion tractography algorithms compared to histological tract-tracing data from the occipital, parietal and temporal cortices in the ferret. Overall, our results showed that diffusion MRI tractography provides statistically significant estimates of ferret brain structural connectivity, although the different tractography algorithms presented variations in terms of sensitivity and specificity.

3.2 Material and Methods

3.2.1 Ferret brain atlas

We used a parcellation based on the atlas of the posterior cortex by Bizley and King 2009. The parcellation scheme was manually drawn on the left hemisphere in the diffusion MRI space using the online tool BrainBox (Heuer et al. 2016, http://brainbox.pasteur.fr/). Tract-tracing data were available for areas 17, 18, 19, 21 (occipital visual areas); 20a and 20b combined (temporal visual areas); PPr and PPc (parietal visual areas) (Figure 3.1 A).

3.2.2 MRI data

T2-weighted and dMRI data was acquired for an adult ferret brain *ex vivo*. The brain was scanned on a Bruker scanner with a b-value of 4000 s/mm^2, 200 directions and 0.24 mm isotropic voxels. Details about the ferret handling, data acquisition pipeline as well as data processing was described in section 2.1 'Datasets and data processing pipelines/MRI acquisitions'.

3.2.3 dMRI processing

Diffusion tractography was performed using MRtrix3 (Tournier, Calamante, and Connelly 2010; Tournier, Calamante, and Connelly 2013). We evaluated the ability of different tractography approaches to reliably reconstruct structural connectivity provided by the tract-tracing experiments. The data was processed following three local models: (1) the diffusion tensor

(DT) model; (2) fiber orientation distribution (FOD) estimated with a constrained spherical deconvolution (CSD) using the tournier algorithm (Tournier, Calamante, and Connelly 2013); and (3) FOD estimated with the multi-shell multi-tissue CSD (msmt CSD) using the dhollander algorithm, each paired with a deterministic and a probabilistic tractography model. Details about data preprocessing and processing can be found in section 2.2 'Datasets and data processing pipelines/MRI processing'.

All the scripts and data are available on the following GitHub repository: https://github.com/neuroanatomy/FerretDiffusionTractTracingComparison.

3.2.4 Anatomical tract-tracing data

Structural connectivity data from anatomical tract-tracing experiments in adult ferrets (of two years age) were obtained from Dell et al. 2019a; Dell et al. 2019c; Dell et al. 2019b. The experiments examined the cortico-cortical and cortico-thalamic connectivity of areas 17, 18, 19 and 21 (occipital visual cortex), PPc and PPr (posterior parietal visual cortex), and 20a and 20b (temporal visual cortex) in adult ferrets by means of retrograde Biotinylated Dextran Amine tracer (BDA). By retrograde tract-tracing, neuronal projections were traced from the axon terminations located in areas 17, 18, 19, 21, PPc, PPr, 20a and 20b (injection sites) of one hemisphere to the neurons' cell bodies, located in different brain regions and across both brain hemispheres. Thus, the injected brain regions were defined as the target regions and the brain regions with cell bodies that were labeled positive for BDA were defined as the source regions. The connections were then quantified by obtaining a fraction of labelled neuron (FLN) value; refer to Dell et al. 2019a; Dell et al. 2019c; Dell et al. 2019b for a detailed explanation on the experimental procedures. Furthermore, for the purpose of this study, we considered only ipsilateral projections and adjusted the connectivity matrix and FLN values to exclude contralateral projections, in order to focus on the edge-complete subnetwork.

3.2.5 Tract-tracing based connectivity matrix

A structural connectivity matrix was assembled from the left hemisphere such that the weights represent the number of retrograde labeled neurons between pairs of regions. This provided us with an asymmetric (directed) matrix indicating projections to the tracer injection sites. The weights were normalized using the fraction of labeled neurons (FLN), the number of labeled neurons in a source region divided by the total number of labeled neurons from the injected region (Markov et al. 2014b). Considering that diffusion MRI tractography does not provide information on the directionality of the connections, the tract-tracing matrix was also symmetrized by averaging FLN values in both directions.

3.2.6 Statistical analyses

Correlation coefficients were used to quantify the degree to which diffusion MRI tractography matched tract-tracing data. Thereafter, in order to characterize the ability of tractography to map structural weights, the strongest connections in the tract-tracing data were progressively removed from both sources (tractography and tract-tracing), and correlation coefficients were then computed on the remaining connections. In the same way, we also computed

correlation coefficients when excluding the weakest tract-tracing connections. Such exploration allowed us to probe whether the correlation coefficient values were mainly driven by strong connections, which correlate with short-range connections and are statistically more likely to be detected. By contrast, weak or longer-range connections are more likely to be spurious (false positives). In order to deal with the log-normal distribution of structural connectivity values in both diffusion MRI tractography and tract-tracing experiments, we computed either the non-parametric Spearman's correlation coefficient or the Pearson's correlation coefficient on the values logarithmically transformed (both FLN and FS). In order to cope with absent connections when performing the logarithmic transformation, for the Pearson's correlations, all raw counts of streamlines and labeled neurons (before the normalizations) were incremented by one. Confidence intervals were computed using bootstrapping at a confidence level of 95%. In addition, we computed the partial Spearman correlations when regressing out the euclidean distance between the centroids of our cortical areas. We first modelled the relationship between the logarithm of the FLN and FS values with the euclidean distance between each pair of cortical areas and extracted its residuals. The residuals from the FLN and the FS were then correlated using Spearman's correlation.

To quantify the ability of tractography to correctly detect existing tract-tracing connections, we computed basic classification performance measures: sensitivity, specificity and precision. Sensitivity quantifies how good a measure is at detecting true connections, while specificity estimates how good a quantity is at avoiding false detections. Average precision quantifies how many of the positively detected connections were relevant. Tract-tracing structural connectivity matrix was progressively thresholded and binarized keeping a given proportion of the strongest weights, from 0.1 to 0.9 by step of 0.1 (Rubinov and Sporns 2010) in order to build a series of receiver operating characteristic and precision and recall curves. The performance measures were then averaged for each threshold as summary statistics.

The statistical analyses were performed using R (https://www.R-project.org/) and Python with the scikit-learn package (Garreta and Moncecchi 2013).

3.3 Results

Structural connectivity estimates from diffusion MRI tractography were all highly positively correlated with the tract-tracing data (Spearman's rho ranging from 0.67 to 0.91, all p < 10-3) (Table 3.1 and Figure 3.1). Probabilistic tractography algorithms increased the correlation values obtained with deterministic tractography. The DT model was not able to recover all the connections found in tract-tracing data for both deterministic (7 connections) and probabilistic (5 connections) tractography, as shown by the 'white' circles that correspond to connections that were not found by the diffusion MRI tractography (lowest rank), and hence the average streamline length of these connections is zero (white circles) (Figure 3.1 C and D). The 95% confidence intervals for the relative predictive power of the different tractography algorithms overlapped, suggesting an absence of statistically significant differences. Consistent results were observed when using the Pearson correlation coefficient (Table 3.1 and supplementary figure A.1).

Spearman correlations were decreased after regressing out the euclidean distance. Partial Spearman correlation values were no longer statistically significant for deterministic tractography (DTI: r = 0.36, p = 0.10 ; CSD: r = 0.39, p = 0.09 ; msmt CSD: r = 0.40, p = 0.07).

However, for probabilistic tractography correlations remained statistically significant (DTI: r = 0.54, p < 0.05 ; CSD: r = 0.66, p < 0.05 ; msmt CSD: r = 0.77, p < 0.05), see supplementary figure A.8. Consistent results were observed when using the Pearson correlation coefficient (Supplementary table A.1).

		Undirected tract-tracing matrix		Directed tract-tracing matrix	
		Spearman	Pearson	Spearman	Pearson
Deterministic	DTI	0.67 ** [0.44-0.94]	0.69 ** [0.37-0.86]	0.50 * [0.22-0.82]	0.48 * [0.07-0.75]
	CSD	0.76 ** [0.56-1.00]	0.68 ** [0.36-0.86]	0.62 * [0.35-0.93]	0.53 * [0.13-0.78]
	msmt CSD	0.71 ** [0.49-0.99]	0.71 ** [0.40-0.87]	0.57 * [0.22-0.95]	0.55 ** [0.16-0.79]
Probabilistic	DTI	0.79 ** [0.65-0.98]	0.78 ** [0.53-0.90]	0.67 ** [0.49-0.91]	0.63 ** [0.27-0.83]
	CSD	0.91 ** [0.82-1.00]	0.88 ** [0.73-0.95]	0.77 ** [0.56-1.00]	0.69 ** [0.38-0.86]
	msmt CSD	0.87 ** [0.75-1.00]	0.89 ** [0.76-0.95]	0.70 ** [0.46-0.99]	0.67 ** [0.33-0.85]

Table 3.1: **Correlations between diffusion MRI tractography and tract-tracing experiments.** P-values inferior to 1.10-3 are indicated by ** and p-values inferior to 0.05 by *.

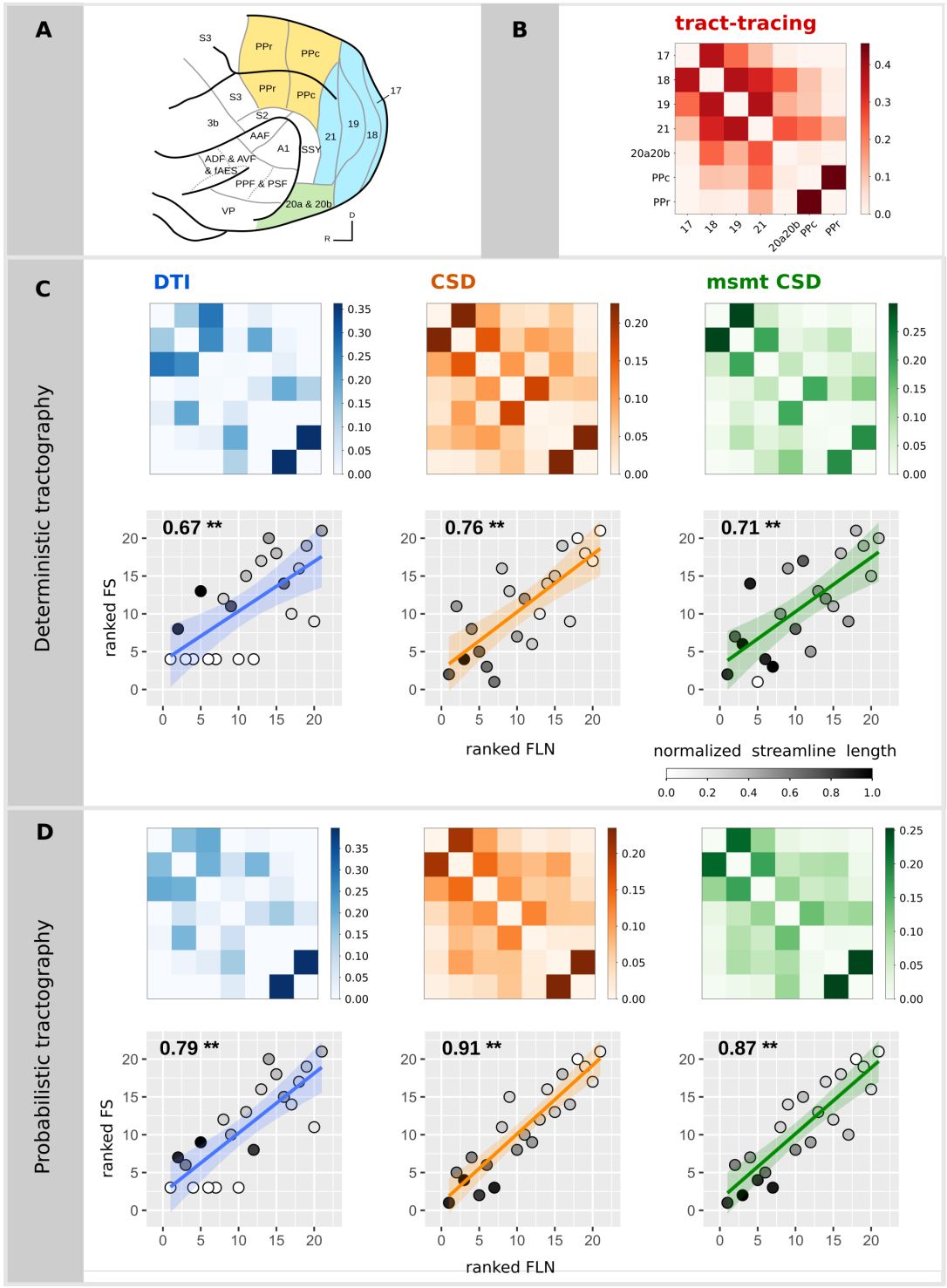
A
S3
PPr
PPc
S3
PPr
PPc
17
S2
3b
19
18
AAF
21
A1
SSY
ADF & AVF
& fAES
PPF & PSF
20a & 20b
VP
D
R
B
tract-tracing
17
18
19
21
20a20b
PPc
PPr
0.4
0.3
0.2
0.1
0.0
C
Deterministic tractography
DTI
CSD
msmt CSD
0.35
0.30
0.25
0.20
0.15
0.10
0.05
0.00
0.20
0.15
0.10
0.05
0.00
0.25
0.20
0.15
0.10
0.05
0.00
0.67 **
0.76 **
0.71 **
ranked FS
ranked FLN
normalized streamline length
0.0
0.2
0.4
0.6
0.8
1.0
D
Probabilistic tractography
0.79 **
0.91 **
0.87 **
ranked FS
ranked FLN

Figure 3.1: **Relationship between diffusion MRI tractography and tract-tracing experiments.**

(A) Ferret brain atlas according to the parcellation of Bizley and King (Figure adapted from Bizley and King 2009). The regions of interest for the comparative study are those colored. Colors code for the different visual brain areas: posterior parietal (yellow), occipital (blue) and temporal cortices (green). (B) Structural connectivity matrix based on tract-tracing experiments, where the weights represent the fraction of labeled neurons (FLN). Structural connectivity matrices estimated from the deterministic (C) and the probabilistic (D) tractography algorithms and the associated scatterplots of the ranked FLN vs. the ranked FS. Each point in the scatter plot corresponds to a connection between a pair of areas for the tract-tracing results (abscissa) and the diffusion results (ordinate). The ranked weights of the connections allow to visualize the Spearman's rho as the slope of the fitted curve. Grey colors code for the average streamline length (values normalized by the maximum streamline length of all the algorithms). P-values inferior to 1.10-3 are indicated by **.

We then tested the influence of strong and weak connections on the relationship between diffusion MRI tractography and tract-tracing data. Structural connectivity estimates from diffusion MRI tractography remained highly positively correlated to tract-tracing data after progressive removal of 25% of the strongest connections and similarly after removal of the weakest connections (Figure 3.2 and supplementary figure A.2 for Pearson correlations). These results show that the correlations between diffusion tractography and tract-tracing were not primarily driven by connections most likely to be recovered by diffusion tractography because of their topographic proximity or their strength (strong weights). Similarly, we observed that the correlations were not affected by the weakest connections which are generally more sensitive to noise (leading to false positives), otherwise there would have been an increase in correlation values.

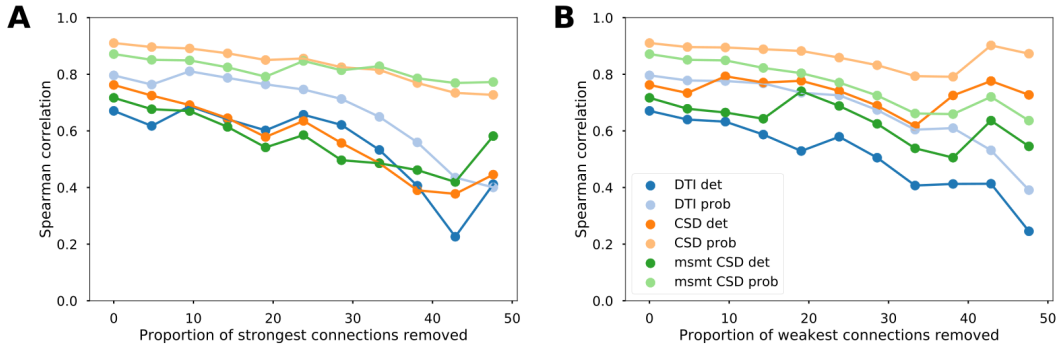

Figure 3.2: **Reliability of the association between diffusion MRI tractography and tract-tracing data.**
Evolution of the Spearman correlation values between tract-tracing and diffusion MRI tractography data as a function of the proportion of strongest (A) and weakest (B) connections removed for the different tractography algorithms.

Measures of sensitivity/specificity/precision give an indication of the detectability of the connections. Our results were averaged and plotted as a function of the proportion of

tract-tracing connections (Figure 3.3). CSD-based algorithms had generally higher sensitivity and precision compared to the diffusion tensor model, while tensor-based tractography had slightly higher specificity.

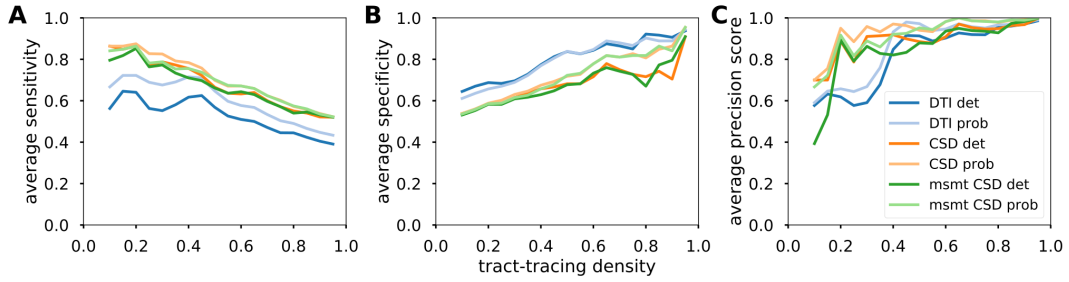

Figure 3.3: **Detection performance of diffusion MRI tractography algorithms.** Averaged sensitivity (A), specificity (B) and precision (C) as a function of the tract-tracing density.

All analyses were also performed comparing tractography with the directed structural connectivity from tract-tracing. We found decreased yet still statistically significant associations (Supplementary figures A.3 to A.7).

3.4 Partial discussion

In the present study, we investigated the ability of different diffusion MRI tractography algorithms to reliably map ferret brain structural connectivity as retrieved from invasive tract-tracing experiments. We found that structural connectivity estimates from tractography were highly correlated with tract-tracing data. The different algorithms presented small, non-significant variations. Our results confirm in the ferret results from previous studies in the monkey (Donahue et al. 2016) and the mouse (Calabrese et al. 2015) as well as results using manganese tracing in the pig (Knösche et al. 2015). Overall, these findings enhance our confidence in diffusion MRI tractography as a powerful tool for exploring the structural connectional architecture of the brain.

We obtained estimates of the reliability of six different tractography algorithms with regard to tract-tracing data for the same cortical areas of the ferret brain. CSD-based algorithms presented the highest degree of concordance with tract-tracing data, and DT-based algorithms the least. However, the differences in correlation values did not appear to be statistically significant, as suggested by the overlapping 95% confidence intervals. High concordance with no particular algorithm outperforming the others was also reported when matching tract pathways from tractography and manganese tracing for a set of tractography algorithms (Knösche et al. 2015). Comparable overall correlations of the weighted connections have been obtained in the macaque brain, with a Spearman's correlation of 0.59 (Donahue et al. 2016). However, here we report little effect of the strongest/weakest connections in the correlation values. The gradual decrease of our correlations indicated that our correlations were not amplified by the weight of strong connections or underestimated by a high amount of false positives stemming from weak connections. In addition, we showed high detection

performance values across algorithms. Consistent with the correlation analysis, we observed higher performances for CSD-based algorithms in terms of precision. Also consistent with prior studies, DT-based results appeared to give slightly higher specificity than CSD-based algorithms, to the detriment of its sensitivity (Sarwar, Ramamohanarao, and Zalesky 2019; Knösche et al. 2015). Such results are likely due to the lower ability of diffusion tensor models to resolve complex fiber geometries (Maier-Hein et al. 2017; Zalesky et al. 2016).

Our correlations were decreased and no longer statistically significant after regressing out distance, for deterministic tractography. Similar results have been reported in the macaque, where correlations decreased from r = 0.59 to r = 0.22 after regressing the distance effects (Donahue et al. 2016). Tractography's ability to recover tracts is expected to decrease as a function of the distance due to technical biases (eg., in probabilistic tractography, the probability to follow a given path drops exponentially with distance). Thus, it has been shown that structural connectivity estimates from diffusion MRI tractography are highly related to their lengths (Roberts et al. 2016; Liptrot, Sidaros, and Dyrby 2014). On the other hand, distance is a biological principle for the preferential connection between two brain areas (Hilgetag et al. 2016). As such, it remains challenging to disentangle these two factors from tractography outputs. Our regions can also be considered as neighbors relative to the whole brain size as they are all located in the occipital, parietal and temporal lobes of one hemisphere. This proximity could have inflated our correlations benefiting from the ability of tratography and tract-tracing to more accurately recover connections from neighboring areas. In any case, the correlations in which distance was regressed out, which corrects for both effects of distance (proximity and remoteness), maintain statistically significant correlations for all probabilistic tractography algorithms (especially based on CSD).

Our results showed a high correlation between diffusion MRI tractography and tract-tracing data, however, we note the limitations in our methodology. Firstly, the two datasets had different origins (i.e. the tract-tracing and tractography were not performed in the same animal) and the sample sizes were very small. Although the ferrets could all be considered mature in terms of brain development (Neal et al. 2007; Jackson, Peduzzi, and Hickey 1989), the ferret used for the MR imaging was only two months old, while the animals used in tract-tracing were around 2 years old. This may have increased inter-individual variability and induced a bias in our cortical parcellations: although the sulcal and gyral patterns (used for cortical parcellation of MRI data, in relation to Bizley and King 2009) are unchanged after postnatal week 4, the ferret brain is still undergoing maturation and growth in all brain structures. The ferret brain growth reaches a plateau at postnatal week 24, however, the differences due to age should be only minor because the cortical architecture at two months of age resembles that at adult age (Neal et al. 2007; Jackson, Peduzzi, and Hickey 1989). Similarly, the cortex continues to undergo rostrocaudal expansion until postnatal week 24, after which the ferret brain reaches its adult size; however, previous studies have showed no significant changes of MRI-measured indices (Barnette et al. 2009; Neal et al. 2007). Although the brain of a two month old ferret is structurally similar to that of an adult brain, it still undergoes functional differentiation and pruning of connections, which could result in a minor shift in the placement of our cortical cytoarchitectonic parcellations and such parcellations can only be observed in histological sections but not in MRI scans.

Secondly, tract-tracing experiments, despite considered as ground-truth, are not exempted of limitations, such as the creation of false positive and false negatives, specificity of tracer and antibody used, spillage of tracer and passive diffusion (Köbbert et al. 2000; Heimer and Robards 2013; Zaborszky, Wouterlood, and Lanciego 2006). In addition, in this study

we only considered the retrograde connections which are easier to quantify and neglected anterograde tracing results.

In sum, this study allowed us to validate structural connectivity estimates from diffusion MRI tractography by comparison with tract-tracing data in the ferret brain and it provided an estimation of the performances of three diffusion tractography algorithms, namely DT, CSD and msmt CSD, using both deterministic and probabilistic tracking. Generally, the currently available connectivity data for the ferret is quite limited; therefore, whole-brain tractography based on diffusion imaging can provide an initial, worthwhile estimate of structural connectivity that can be used for further anatomical, developmental and computational studies of the ferret brain.

Chapter 4

Characterization of the evolution of cortical lamination during ferret brain development, using histological slices

Cortical lamination is characteristic of the mammalian brain. A disruption in its development can cause critical perturbation in brain function and behavior. It is therefore crucial to better characterize the typical development of the cytoarchitectonic organization in order to identify abnormal development. Here, we used the ferret to study cytoarchitectonic maturation, as the ferret brain is a good intermediate between the highly complex human brain and the extensively studied but simple mouse brain. We developed an semi-automated pipeline to describe the cytoarchitectonic organization according to grey level profiles obtained from histological Nissl sections. This allowed us to acquire longitudinal whole brain quantifications from precise microscopic data.

4.1 Introduction

The mammalian neocortex is characteristically organized in 6 successive layers (Economo 2009). Each layer is identifiable by its variation of cell type and density. Furthermore, these layers vary in size (thickness) and neuronal density across the cortex, which results in the cortex being classified according to a set of cytoarchitectonic types. If the 6 layers can be clearly defined, the cortical area is classified as eulaminate. If layer IV is poorly defined, the cortical area is classified as dysgranular and if there are mainly 3 layers visible (layer I, layer II/III and layer V/VI), it is classified as agranular.

These variations in the cytoarchitecture have been used since the early 1900s as one of the first criteria for parcellating the brain (Brodmann 1909; Economo and Koskinas 1925). The cytoarchitecture has an integral role in deciphering brain structure and function (Rahimi-Balaei et al. 2018). The neocortical lamination is tightly linked to 1) brain morphology; as we can observe, in the Brodmann parcellation, that the parcels follow the folding pattern of the brain, and to 2) connectivity; as the difference in cytoarchitectonic type between a pair of regions, can predict the existence or absence of connections (Barbas 1986; Beul, Grant, and Hilgetag 2015; Goulas, Uylings, and Hilgetag 2017).

Cytoarchitecture and its lamination has originally been studied in the mammalian brain by means of visual inspection. The studies were performed on small sample sizes and using Nissl (Brodmann 1909) or silver staining (Economo and Koskinas 1925). The Nissl staining allows observers to identify neuronal cell bodies in the brain but also glia, which can cause observer-dependent variations in counts (Brodmann 1909). The silver stain stains the axon fibers and paths (Gallyas 1979). These initial studies remain founding results and although these techniques are still used today (Brodmann 1909; Economo and Koskinas 1925), they are highly time consuming. Furthermore, such histological studies are subject to inter-individual species variations as well as observer-dependent biases.

Since the 1980s, scientists have been developing different quantitative approaches such as stereology (Gundersen and Jensen 1985) and grey level profiles (Schleicher, Zilles, and Wree 1986; Schleicher and Zilles 1990; Schleicher et al. 1999) to approximate cytoarchitecture in a more extensive manner. Neuronal density is often used as a proxy for cytoarchitectonic type (Hilgetag and Grant 2010; Beul and Hilgetag 2019) as the two are positively correlated (Dombrowski, Hilgetag, and Barbas 2001). Stereology facilitates the reporting of neural densities by using random systematic sampling of histological sections and extrapolating the neuronal density from an area (Gundersen and Jensen 1985). Although this method allows us to obtain quantitative measures across the whole brain, it is not automated and extremely time consuming. Zilles and colleagues (Schleicher et al. 1999; Schleicher et al. 2009) have developed a dedicated system, which digitizes Nissl sections, computes the grey level index (GLI) and extracts manually placed profiles of grey level contrasts across the depth of the cortex. The variations of the grey contrast allows one to estimate the local variations in cell density throughout the cortex, hence estimating the position of the different cortical layers. Although this method requires a dedicated system and manual placement of the profiles, it presents the advantage of offering quantitative, observer-independent measures across the whole cortex.

Current studies have only been performed in mature brains, however the establishment of cytoarchitecture through neurogenesis and neuronal migration is one of the initial and founding processes of brain development (Guarnieri et al. 2018; Rahimi-Balaei et al. 2018). As cytoarchitecture is tightly linked with structural connectivity, a disruption in the brain structure

(cytoarchitecture or structural connectivity) impacts brain function and behavior (Schotten, Foulon, and Nachev 2020; Redell et al. 2020). It is therefore essential to better characterize the typical development of the cortical cytoarchitecture in order to identify abnormal development.

In this work we will use the ferret as an animal model to study the maturation of the cytoarchitectonic organization during development. The ferret is a good intermediate between the high complexity of the human brain and the lissencephalic (smooth) mouse brain. The ferret, at the adult age, displays a set of sulci (furrow) which are equivalent to the primary sulci in humans (Borrell 2018) and hence present some of the characteristics of a more complex brain. In addition, the ferret brain matures and undergoes gyrification during the first month after birth (Voigt, De Lima, and Beckmann 1993; Smart and McSherry 1986a) which allows us to observe postnatal processes (folding, lamination) which occur during the last trimester of gestation in humans (Brodmann 1909).

4.2 Material and Methods

We developed a pipeline in order to semi-automatically extract grey level profiles through the whole cortex of ferrets aged from postnatal day 4 (P4) to P32. These grey level profiles are a good quantitative metric for studying the maturation of the cortical cytoarchitecture (Schleicher and Zilles 1990). All the code was developed in Python (https://www.python.org).

4.2.1 Dataset and processing

The dataset was composed of Nissl stained histological slices of ferrets aged from P4, P8, P16 and P32. The slices were scanned at 20X on a Zeiss Axioscan Z1, then registered and cropped following the pipeline described previously in section 2.3 'Datasets and processing pipelines/Histological sections'. The cytoarchitectonic organization of the cortex was estimated by grey level intensity profiles. The profiles were automatically extracted based on a manually edited segmentation of the brain (only manual step of the profile processing). The full pipeline was further described in section 2.4 'Datasets and processing pipelines/Histological data processing' and is illustrated in Figure 4.1. The profiles were then normalized by length, mean value and minimum and maximum values (section 2.4.4 'Datasets and processing pipelines/Profile normalization'). The normalization of the profiles allowed us to remove potential intensity variations and to enhance the cytoarchitectonic patterns (profile shapes) which we used as proxy to cortical maturation. The profiles described the grey intensities such as 0 is black (high amount of staining) and 1 is white (no staining).

4.2.2 K-Mean clustering

The normalized profiles were clustered into 10 clusters using a k-mean algorithm (scikit-learn, Garreta and Moncecchi 2013). We chose to use 10 clusters as a balance between minimizing the number of clusters and minimizing the variance within clusters. (Figure 4.2).

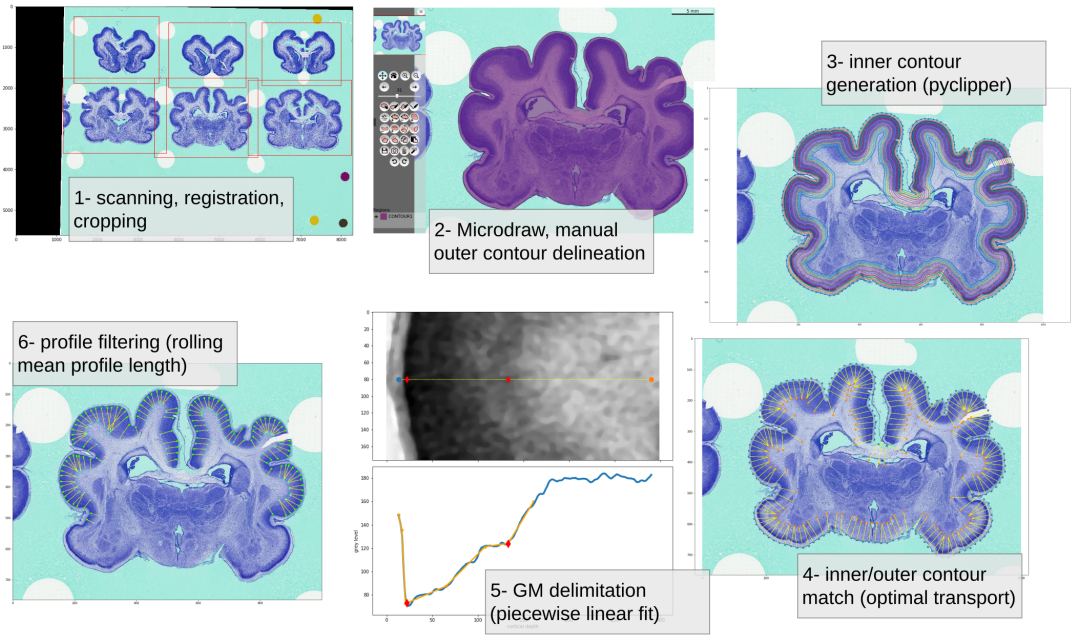

Figure 4.1: **Histological data processing pipeline.**
Sequence of panels representing a summary of the histological data processing pipeline.

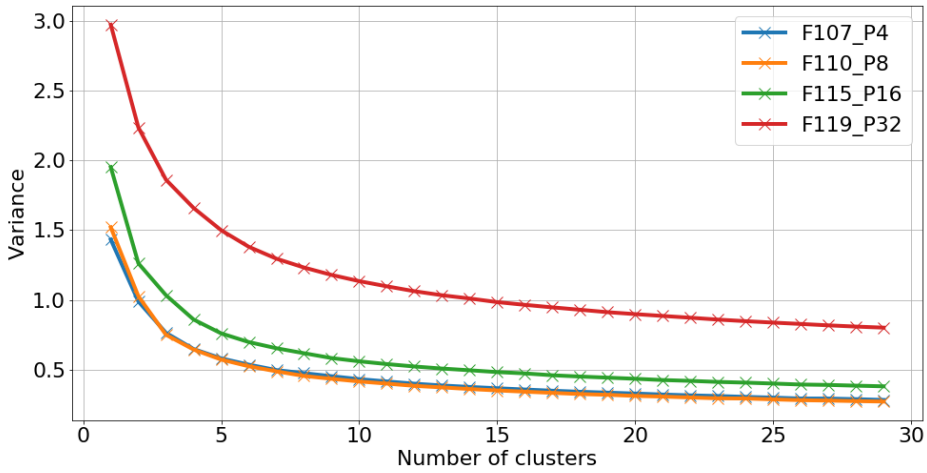

Figure 4.2: **Scree plot of the k-mean cluster analysis.**
The variance within clusters decreases as the number of clusters increases.

4.2.3 Profile cluster and parcellation

As described in section 2.5 'Datasets and processing pipelines/Establishing the correspondence between the histological and MRI space', each histological slice was registered to its corresponding MRI slices so that each of the profiles could be assigned to the closest node on the corresponding surface mesh. The surface was parcellated using a 200 parcel random parcellation, common at all time points of the development (Figure 4.3). The 200 parcels allowed us to obtain a fine grained parcellation while being able to maintain all the parcels with a minimum of 3 mesh nodes for the smallest mesh at P4. The cluster which was the most represented in the parcel was assigned as a label for the parcel.

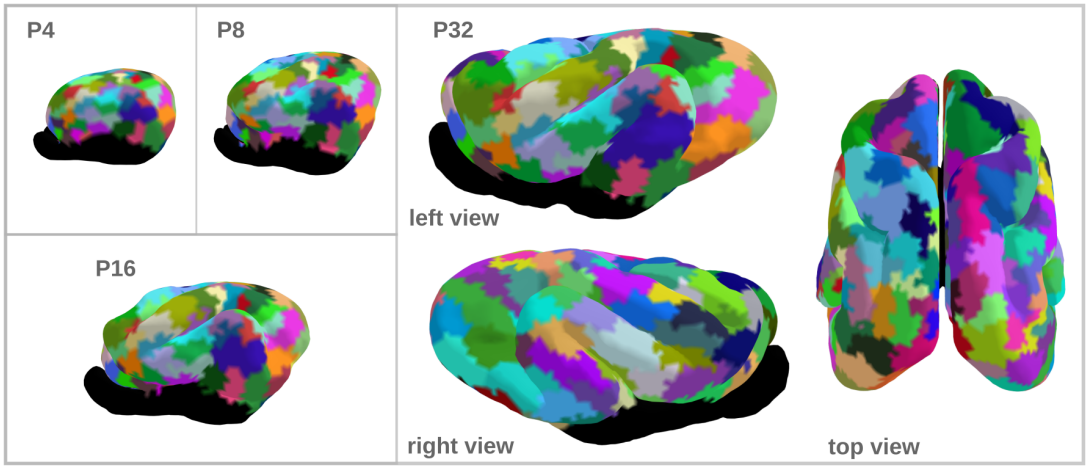

Figure 4.3: **Common 200 parcel random parcellation.**
Representation of the 200 parcel random parcellation at each time point (left views). Left, right and top view of the parcellation on the ferret at P32.

4.2.4 Maturation trends

In order to better understand the maturation trends occurring across the cortex, we made use of the above common parcellation across the different time points. For each of the parcels, we concatenated the four profiles corresponding to that parcel for the ferrets at time points P4, P8, P16 and P32 as one vector (Figure 4.4) and clustered them into 10 clusters.

4.3 Results

The profiles provided a representative description of the cytoarchitectonic organization of the whole brain. The cluster centers could reliably be matched back to the lamination observable on the histological sections. A number of the cluster centers which were sparse or not represented after being grouped into parcels could be identified as spurious. The overall clustering of the cytoarchitecture at the different time points resulted in a consistently symmetrical parcellation of the brain.

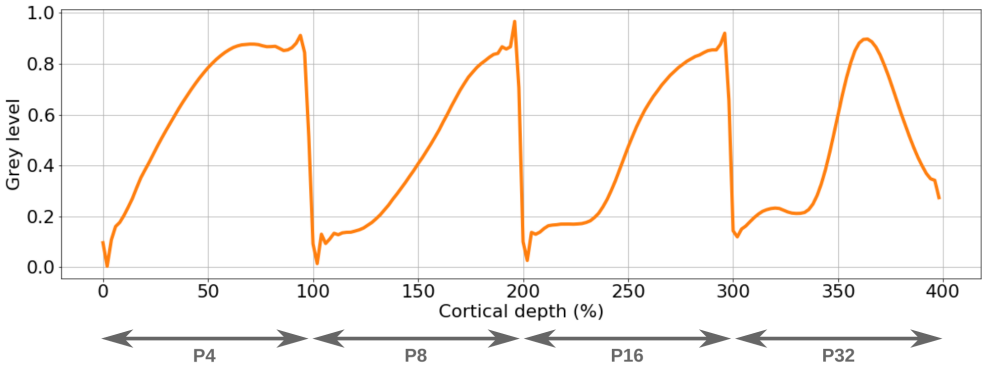

Figure 4.4: **Label-wise concatenation of cluster centers across time points.** The cluster center at each parcel was concatenated with its corresponding cluster center at the other time points. We represented here the example for one parcel. The x-axis represents four times the cortical depth (100 units per time point) and the y-axis represents the normalized grey level (where 0 is the darkest grey level of the profile and 1, the brightest). Between x=[0-100] ([100-200], [200-300], [300-400]), we can observe the cluster center from a given parcel going from the layer I/II interface (x=0) to the GM/WM interface (x=100) for the ferret at P4 (P8, P16, P32, respectively).

4.3.1 P4 results

At P4, we could observe that the most represented cluster centers (Figure 4.5 B and C, cluster purple, brown, blue and orange) were shaped as a gradual increase of the grey intensity from the beginning of layer II to the GM/WM interface. No layer was visible neither in the cluster centers nor in the histological sections (Figure 4.5 B and D). The cells were tightly packed and formed a single compact layer visible as the cortical plate. In terms of repartition of the clustering, the brain was mainly divided axially, separating the lateral and dorsal areas (Figure 4.5 C).

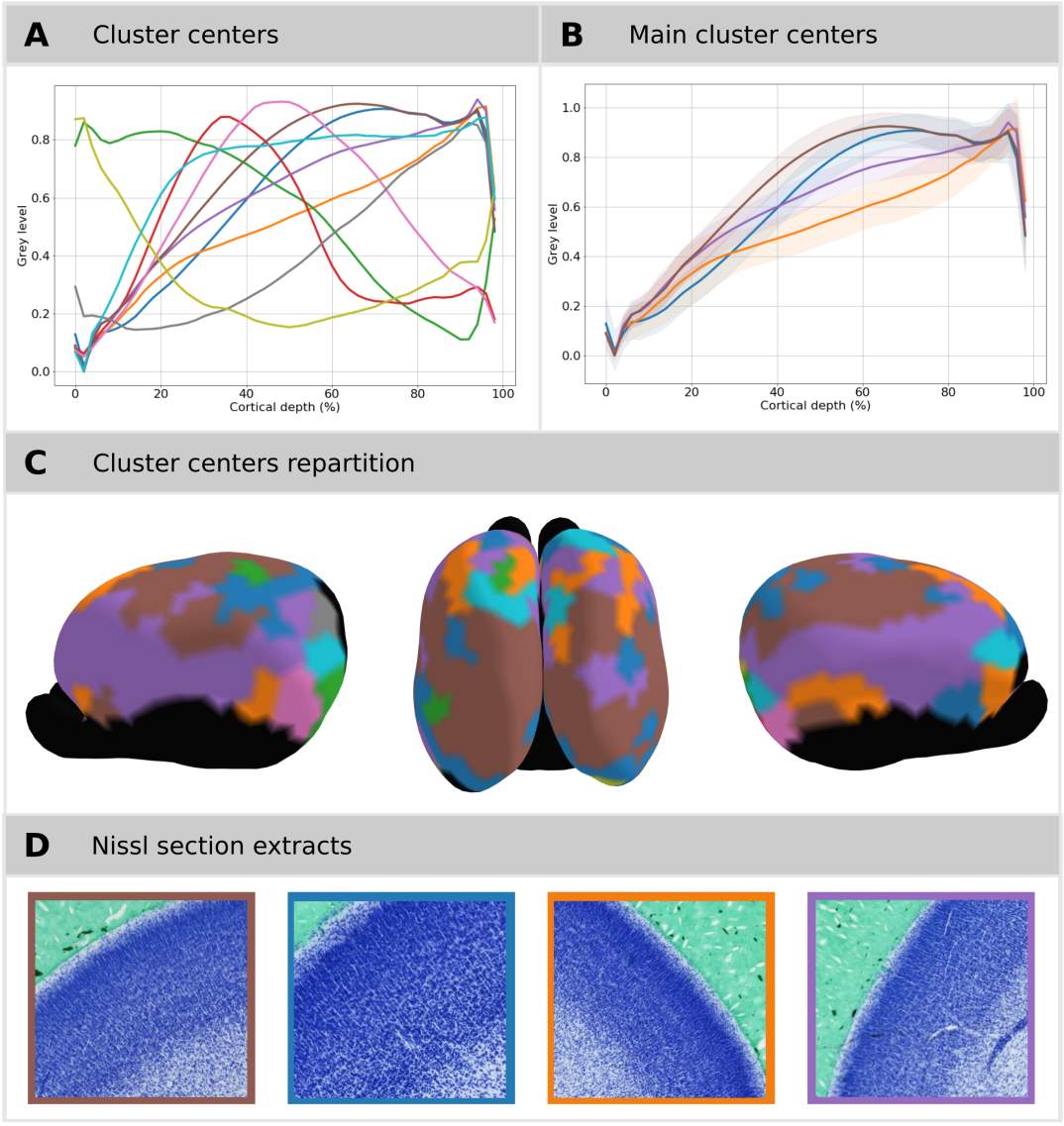

Figure 4.5: **Lamination clustering of the P4 ferret.**
(A) Ten cluster centers of the k-mean clustering. The x-axis represents the cortical depth, where 0% is at the layer I/II interface and 100% is at the GM/WM interface. The y-axis represents the normalized grey level, where 0 is the darkest grey level of the profile (more staining) and 1, the brightest intensity (less staining). (B) Main cluster centers, most represented clusters after projection on the surface parcellation. The shaded areas represent the standard deviation of the cluster centers. (C) Cluster repartition on the surface mesh. Left view, Top view and Right view of the ferret brain. (D) Representative extracts from the Nissl sections of the most represented clusters on the surface. The clusters can be identified by a color code, consistent across the panels.

4.3.2 P8 results

At P8, the main cluster centers (Figure 4.6 B and C, cluster green, pink, purple and blue) started from the layer I/II interface with an initial plateau between grey level 0.1 and 0.2, followed by a gradual increase until the GM/WM interface is reached (Figure 4.6 B). This first initial plateau between cortical depth 10% and 30% suggested the future delimitation of the cortical lamination between the supragranular layers (layer II and III) and the infragranular layers (layer V and VI). The demarcation of these two coarse layers were more visible in the lateral brain areas (Figure 4.6 C) where the initial plateau was followed by a rapid increase of the grey level (between cortical depth 30% and 70%, Figure 4.6 B). The infragranular layers were less densely packed and showed more distinguished neurons (Figure 4.6 D). In the dorsal areas, the cluster centers displayed a similar gradual increase of the grey level than the cluster centers at P4, where no layers were visible and all neurons were densely packed (Figure 4.5 B and 4.6 B, C and D).

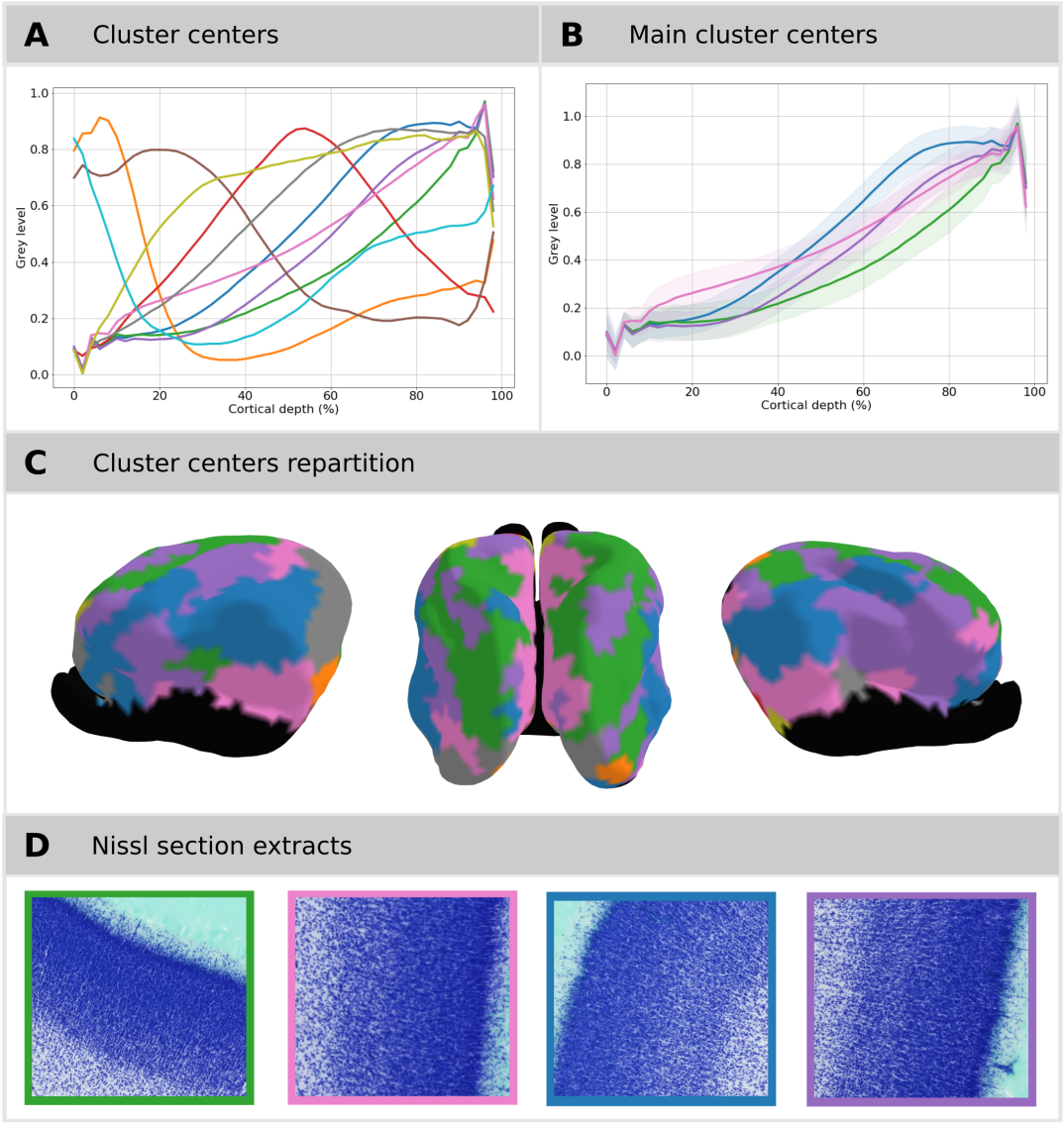

Figure 4.6: **Lamination clustering of the P8 ferret.**
(A) Ten cluster centers of the k-mean clustering. The x-axis represents the cortical depth, where 0% is at the layer I/II interface and 100% is at the GM/WM interface. The y-axis represents the normalized grey level, where 0 is the darkest grey level of the profile (more staining) and 1, the brightest intensity (less staining). (B) Main cluster centers, most represented clusters after projection on the surface parcellation. The shaded areas represent the standard deviation of the cluster centers. (C) Cluster repartition on the surface mesh. Left view, Top view and Right view of the ferret brain. (D) Representative extracts from the Nissl sections of the most represented clusters on the surface. The clusters can be identified by a color code, consistent across the panels.

4.3.3 P16 results

At P16, the supragranular/infragranular demarcation was visible throughout the cortex (Figure 4.7 B and C, cluster blue, purple, green and cyan). The initial plateau starting at layer II was extended, followed by a rapid increase of the grey level gradients. The gradients of the transition from the supragranular layers to the infragranular layers could be observed on the histological slices and gave us an indication of the level of differentiation of the infragranular layers (Figure 4.7 B and D). The supragranular layers were still undifferentiated across the cortex and are thought to maintain the cortical plate (Figure 4.7 D). We observed that lateral areas (cluster green and cyan) had a more distinct supra/infragranular demarcation, with the infragranular layers having better defined neurons due to the looser packing of these laminae. In addition, layers V and VI were differentiated and clearly identifiable in the primary somatosensory cortex (Figure 4.7 B and D, cluster green). The beginning of layer V could be identified when the cluster center profile reached a plateau at its maximal value after a steep supra/infragranular transition which occurs between a cortical depth of 30% and 60%. The plateau was initially composed of very high values i.e. less densely populated area (layer V) between cortical depth 60% and 80% and a slight decrease i.e. more densely populated area (layer VI) between cortical depth 80% and 90%. Layer V and VI were visible in the histological sections (Figure 4.7 C, cluster green).

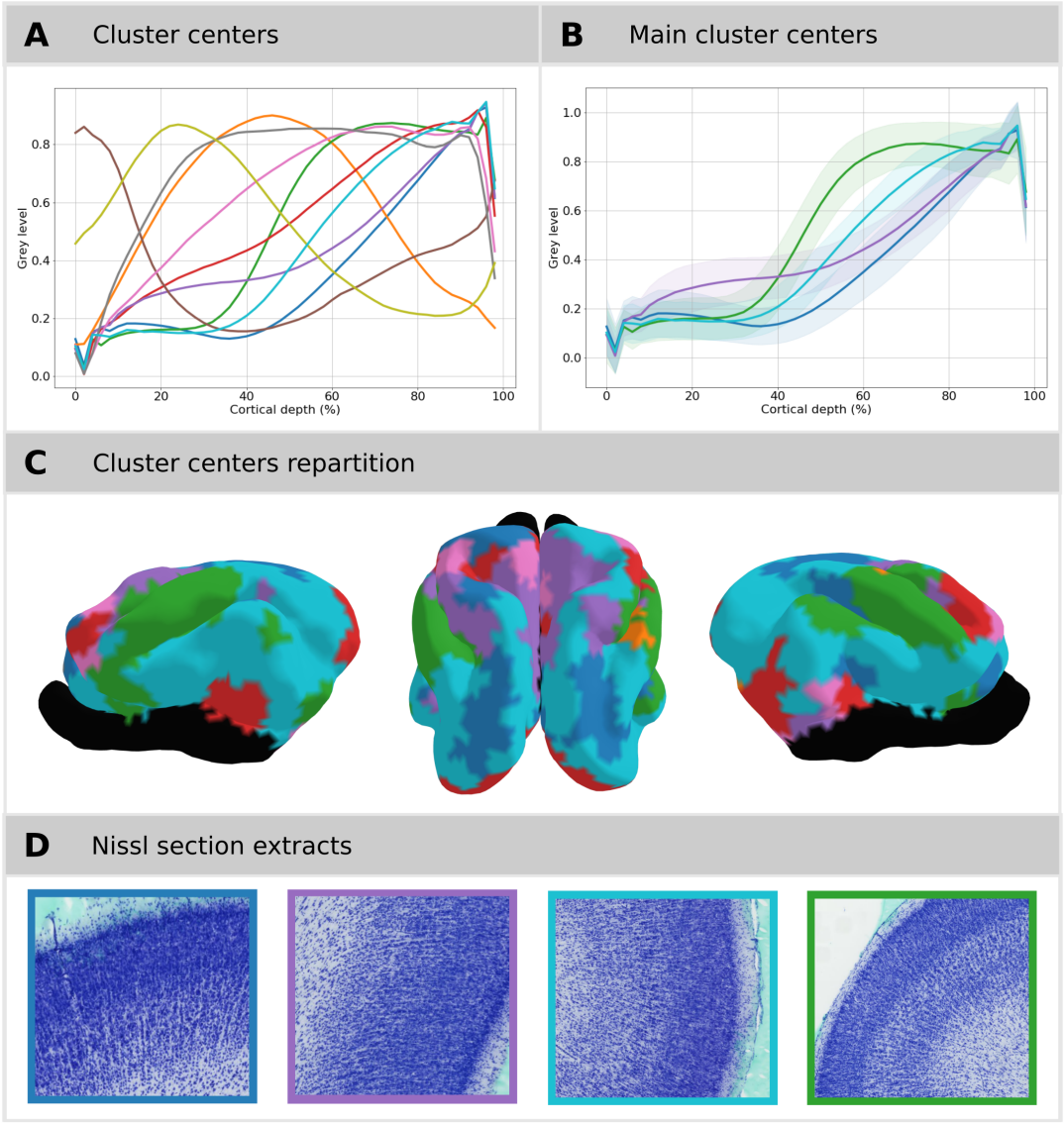

Figure 4.7: **Lamination clustering of the P16 ferret.**
(A) Ten cluster centers of the k-mean clustering. The x-axis represents the cortical depth, where 0% is at the layer I/II interface and 100% is at the GM/WM interface. The y-axis represents the normalized grey level, where 0 is the darkest grey level of the profile (more staining) and 1, the brightest intensity (less staining). (B) Main cluster centers, most represented clusters after projection on the surface parcellation. The shaded areas represent the standard deviation of the cluster centers. (C) Cluster repartition on the surface mesh. Left view, Top view and Right view of the ferret brain. (D) Representative extracts from the Nissl sections of the most represented clusters on the surface. The clusters can be identified by a color code, consistent across the panels.

4.3.4 P32 results

At P32, all neurons throughout the cortex were differentiated. The main profiles (Figure 4.8 B and C, cluster blue, green, pink and orange) detected three main layers. First the initial plateau represented a thick, densely populated layer containing the supragranular layers (layer II and III) and granular layer (layer IV) when it existed (Figure 4.8 B and D). After the supra/infragranular transition, we observed a thinner, less densely populated layer, layer V and finally a more densely populated layer of varying thickness, likely layer VI. The cluster centers could depict the various relative depths at which the different layers were positioned, as it can be observed for layer V in cluster green, pink and orange by their difference in maximal value representing the center of layer V (Figure 4.8 B, green: cortical depth 50%, pink: 65%, orange: 75%). Finally, similarly to P16, the primary somatosensory cortex (coronal gyrus, cluster pink) showed the most refined lamination (Figure 4.8 B, C and D, cluster pink).

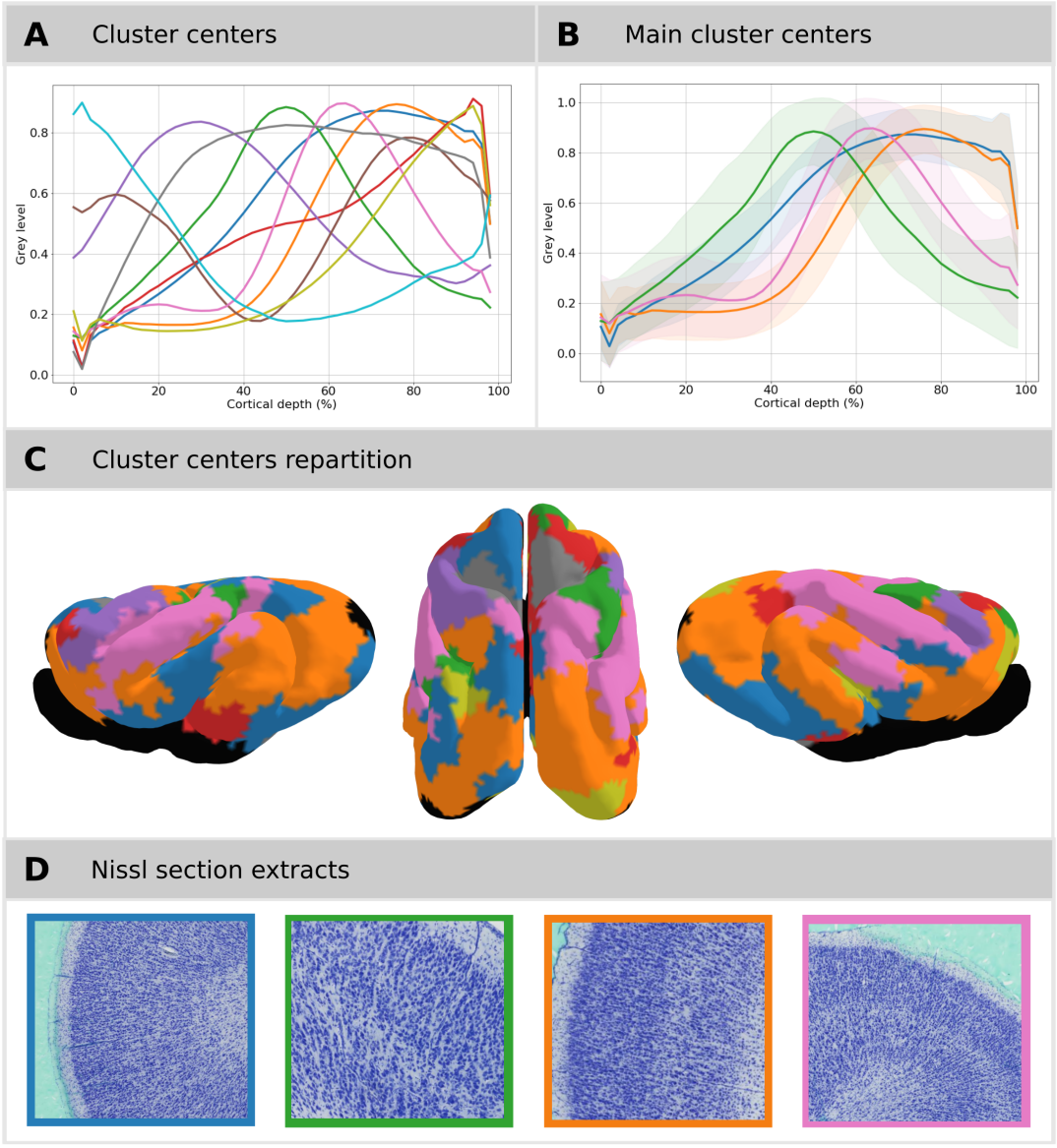

Figure 4.8: **Lamination clustering of the P32 ferret.**
(A) Ten cluster centers of the k-mean clustering. The x-axis represents the cortical depth, where 0% is at the layer I/II interface and 100% is at the GM/WM interface. The y-axis represents the normalized grey level, where 0 is the darkest grey level of the profile (more staining) and 1, the brightest intensity (less staining). (B) Main cluster centers, most represented clusters after projection on the surface parcellation. The shaded areas represent the standard deviation of the cluster centers. (C) Cluster repartition on the surface mesh. Left view, Top view and Right view of the ferret brain. (D) Representative extracts from the Nissl sections of the most represented clusters on the surface. The clusters can be identified by a color code, consistent across the panels.

4.3.5 Maturation trends results

The parcel-wise clustering of the individual cluster centers allowed us to obtain concise longitudinal maturation trends for the whole brain (Figure 4.9 A). The longitudinal cluster centers emphasized the general pattern of cytoarchitectonic development that was observed at the different time points (Figure 4.9 B). We observed that the cytoarchitectonic pattern depicted by the profiles were most similar at P4 and diverged with development (Figure 4.9 B). Moreover, the clustering appeared to be strongly led by the cytoarchitectonic pattern present at P32 as the clustering of the maturation trends was highly analogous to the original clustering of the profiles at P32 (Figure 4.8 C and 4.9 C).

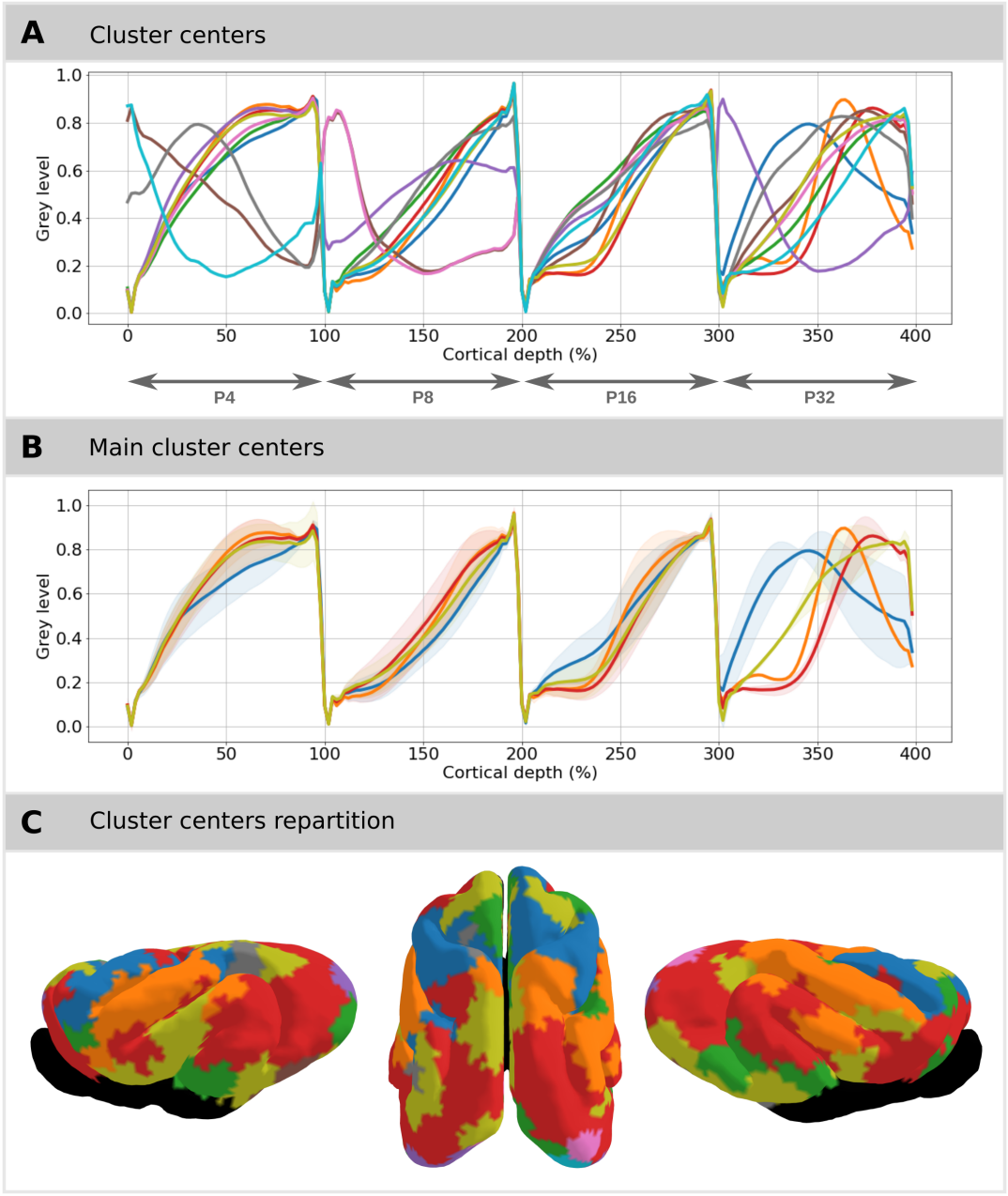

Figure 4.9: **Clustering of the parcel-wise maturation trends.**
(A) Ten cluster centers of the k-mean clustering. The x-axis represents four times the cortical depth (100 units per time point going from layer I/II interface to the GM/WM interface). The y-axis represents the normalized grey level, where 0 is the darkest grey level of the profile (more staining) and 1, the brightest intensity (less staining). (B) Main cluster centers, most represented clusters after projection on the surface parcellation. The shaded areas represent the standard deviation of the cluster centers. (C) Cluster repartition on the surface mesh. Left view, Top view and Right view of the ferret brain.

4.4 Partial discussion

In this study we investigated the development of cytoarchitecture in the ferret using an semi-automated processing of histological sections. The grey level profiles extracted from the Nissl sections and their clustering provided a concise description of the whole brain lamination. The profiles depicted the progressive inside-out pattern of development of the cortical layers. We observed a laterodorsal gradient of development of the cortical areas visible up to 4 weeks postnatally, after which all layers were formed.

The cytoarchitectonic organization at P4 was described by the profiles as a single dense layer, which evolved at P8 into a differentiation of the infragranular layers in the lateral areas visible by the apparition of an initial plateau in the profiles. At P16, a clear supra/infragranular demarcation was visible all over the cortex, with the lateral areas displaying the most defined lamination. Finally, at P32 all layers were present and all neurons were differentiated. This pattern of maturation was emphasized by our computation of mature trend clusters and previously described in the ferret visual cortex by traditional histological staining (Jackson, Peduzzi, and Hickey 1989; Sur and Leamey 2001). In addition, the observed pattern of neurogenesis complies with the inside-out pattern of development of the cortical layers studied in the ferret visual cortex (Jackson, Peduzzi, and Hickey 1989) as well as in primates (Rakic 1974).

Furthermore, our profiles highlighted an overall laterodorsal gradient of maturation of the cortical lamination, marked by an axial division of the clusters at P4 and a clear difference in lamination maturation at P8 and P16 observable in the profiles and confirmed by visual inspection of the sections. Such a gradient of cortical maturation has also been observed for different maturation processes in the ferret such as neurogenesis (Jackson, Peduzzi, and Hickey 1989), synaptogenesis (Voigt, De Lima, and Beckmann 1993) and dendritogenesis (Zervas and Walkley 1999). This laterodorsal gradient is usually described coupled with a rostro-caudal gradient of development (Jackson, Peduzzi, and Hickey 1989; Voigt, De Lima, and Beckmann 1993; Zervas and Walkley 1999), which we did not observe in our dataset. At P32, all cortical layers were formed and neurons differentiated, however a laterodorsal gradient of maturation was no longer present. Similar processes (laterodorsal gradient, inside-out pattern of development and all layers formed at 4 weeks of age) have been observed in the ferret by synaptophysin staining in their first weeks of postnatal development (Voigt, De Lima, and Beckmann 1993). Moreover the maturation trend cluster centers highlighted a high diversity in cytoarchitectonic patterns (profile shapes) at P32 indicating a higher refinement of the cortical lamination similar to that observed in the adult ferret (Radtke-Schuller 2018).

Our model uses cortical grey level profiles and characterizes the overall cytoarchitectonic maturation in the first month of development of the ferret. As our focus is on cytoarchitectonic pattern variations across development, it was not possible to obtain clusters that describe functional regions. The reason for this can be explained by the scale of our random parcellation, whereby the parcels extend over several functional regions in larger, more mature ferret brains. Moreover our profiles were normalized by their length, omitting cortical thickness as well as cell type and size in our clustering which are essential features for parcellating the brain (Brodmann 1909).

The semi-automated processing of histological Nissl sections appeared to be an effective method to obtain an observer independent characterization of the cytoarchitectonic organization of the brain and its maturation, however as with any study, there are limitations.

Firstly, due to time and resource constraints, our dataset is composed of one individual per time point. This could cause our results to be subjected to minor interindividual variations, which is expected in experimental research. To reduce the effect of interindividual variations, larger sample sizes are preferred. Secondly, the coronal sectioning of the brain slices induced sectioning transversally through the cortex mainly in the most occipital and frontal areas of the brain but also in some of the gyri. These transversal sections did not allow us to generate reliable profiles orthogonal to the brain surface in these regions and may have impacted the presence of rostro-caudal gradient of development. This limitation is however inherent to sectioning and would have occurred in the temporal areas with sagittal sectioning or in the dorsal and ventral areas with axial sectioning. Finally, although Nissl stains both neuron bodies and glia, this would not have impacted our results as we examined staining intensity and did not quantify our results in terms of neuronal density.

In conclusion, our semi-automatically generated grey level profiles can depict the inside-out pattern of the cortical layers. We identified a laterodorsal gradient of maturation of the cytoarchitecture in the ferret, up to 4 weeks of age, after which all the cortical layers are present. These results are in accordance with the results from traditional histological experiments described in the literature. Moreover, this work presents a valuable dataset allowing to study the development of the cytoarchitecture in the ferret. This dataset is made freely available through the FIIND project (https://neuroanatomy.github.io/fiind/) and can serve as background for further analysis on structural and function connectivity development.

Chapter 5

Investigation of the relationship between cortical lamination and cortico-cortical connectivity during ferret brain development

Cellular organization and structural connectivity are the substrate for brain function and behaviour. Cellular organization and structural connectivity have been shown to be related at the mature stage in mammals, however little is known about the establishment of this relationship during brain development. We used a multimodal approach, including histological slices and diffusion MRI to study the relationship between cytoarchitectonic organization, distance between brain regions and structural connectivity during the development of the ferret brain.

5.1 Introduction

Brain structure, i.e. its cellular organization and structural connectivity, is the basis for function and behavior. Disruptions in brain structure have been shown to impact brain function and behavior in a variety of ways (Redell et al. 2020; Schotten, Foulon, and Nachev 2020). Furthermore, it is well established that cortical cytoarchitecture and structural connectivity are interrelated (Barbas 1986; Beul, Grant, and Hilgetag 2015; Goulas, Uylings, and Hilgetag 2017). For example, the similarity of cytoarchitecture in two brain areas has been shown to predict a higher likelihood of areal interconnectivity in the mouse (Goulas, Uylings, and Hilgetag 2017), cat (Beul, Grant, and Hilgetag 2015), marmoset (Majka et al. 2016), macaque (Beul and Hilgetag 2019) and humans (Goulas et al. 2016; Wei et al. 2019). Although these cross-species validations help to decipher common and species-specific principles governing the presence or absence of structural connections (Goulas et al. 2019), most of these analyses are based on traditional histological and tract-tracing experiments, which are not only highly time consuming and observer dependent but only examine this relationship in the adult brain.

Early brain development is a crucial period for the establishment of cortical cytoarchitecture and structural connectivity (Guarnieri et al. 2018; Rahimi-Balaei et al. 2018). Disruptions in brain development such as prematurity or fetal alcohol exposure can alter brain morphology (Dubois et al. 2019), structural connectivity (Batalle et al. 2017), functional connectivity and cortical microstructures (Tang et al. 2018). It is therefore essential to improve the characterization of the typical development of brain structure in order to identify abnormal development.

We used the ferret as an animal model for studying the relationship between cortical lamination and structural connectivity during development. The ferret is a small gyrencephalic mammal, which has the particularity of being born with an immature, lissencephalic brain that develops into a mature, gyrified brain within the first postnatal month (Smart and McSherry 1986a; Smart and McSherry 1986b; Neal et al. 2007). Thus, the ferret has become a well established model for studying brain development (Jackson, Peduzzi, and Hickey 1989; Voigt 1989; Barnette et al. 2009; Sawada and Watanabe 2012; Khalil and Levitt 2014) and prematurity (Empie, Rangarajan, and Juul 2015; Wood et al. 2018).

Our dataset was composed of structural connectivity data from diffusion MRI tractography, which was previously validated in the adult ferret (Delettre et al. 2019) as well as cytoarchitectonic data that was extracted semi-automatically from histological Nissl sections and described in terms of grey level profiles (Chapter 4). Our four time points (postnatal day 4, 8, 16 and 32) from the histological sections and five time points (postnatal day 4, 8, 16, 32 and adult) from the diffusion tractography allowed us to observe processes which occur during the third trimester of gestation in humans (Clancy, Darlington, and Finlay 2001). This rich dataset describing the cytoarchitectonic organization of the developing ferret cortex in combination with the connectivity data from the diffusion MRI allowed us to test the previously observed relationship between cytoarchitecture and cortico-cortical connectivity and witness its evolution during early development.

5.2 Material and Methods

5.2.1 Histological slices

The dataset was composed of Nissl sections, stained for neuronal cell body and glia, at four time points: postnatal day 4 (P4), P8, P16 and P32. The histological slices of the individual

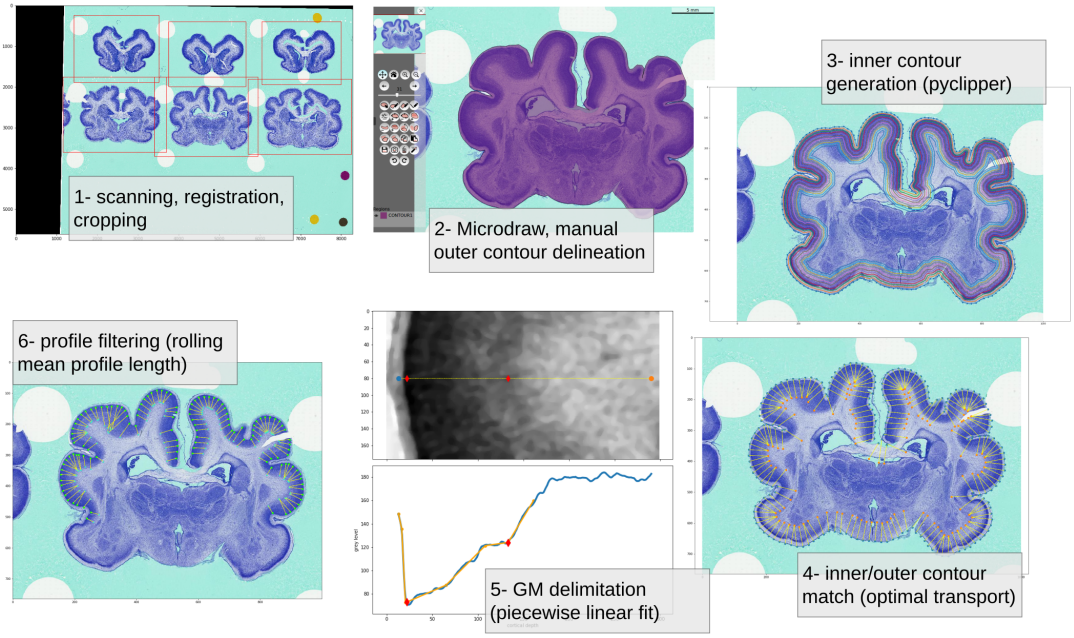

Figure 5.1: **Histological data processing pipeline.**
Sequence of panels representing a summary of the histological data processing pipeline.

brains were scanned at 20X on a Zeiss Axioscan Z1, then automatically registered to one another within each corresponding time points. The sections were cropped and imported to Microdraw (https://microdraw.pasteur.fr) for precise segmentation of the brain. The outer contours of brains served as a basis for the automatic extraction of grey level profiles, describing the cytoarchitectonic organization of the cortex. The profiles were normalized by length, mean, minimum and maximum values. Precisions of the dataset and processing can be found in section 2.3 'Datasets and processing pipelines/Histological sections' (Figure 5.1).

5.2.2 Diffusion MRI dataset

The diffusion MRI dataset was composed of five time points: postnatal day 4 (P4), P8, P16, P32 and adult stage. These ferrets were different specimens to the ones used for the histology data. The brains were scanned *ex vivo* in a Bruker scanner with a b-value of 4000 or 2000 s/mm^2 and 200 directions. The tractography algorithm used in this analysis is a probabilistic CSD with 1 million streamlines tracked using MRtrix3 (Tournier, Calamante, and Connelly 2010; Tournier, Calamante, and Connelly 2013). This tractography algorithm provided the highest correlation to tract-tracing experiments in the adult ferret (cf. Chapter 3, Delettre et al. 2019). The connectivity matrices were binarized in order to only consider the presence or absence of connections between pairs of regions. Pearson correlations between the binarized connectivity matrices are indicated in Figure 5.2. Details about the data acquisition, preprocessing and tractography pipeline can be found in section 2.2 'Datasets and processing pipelines/MRI processing'.

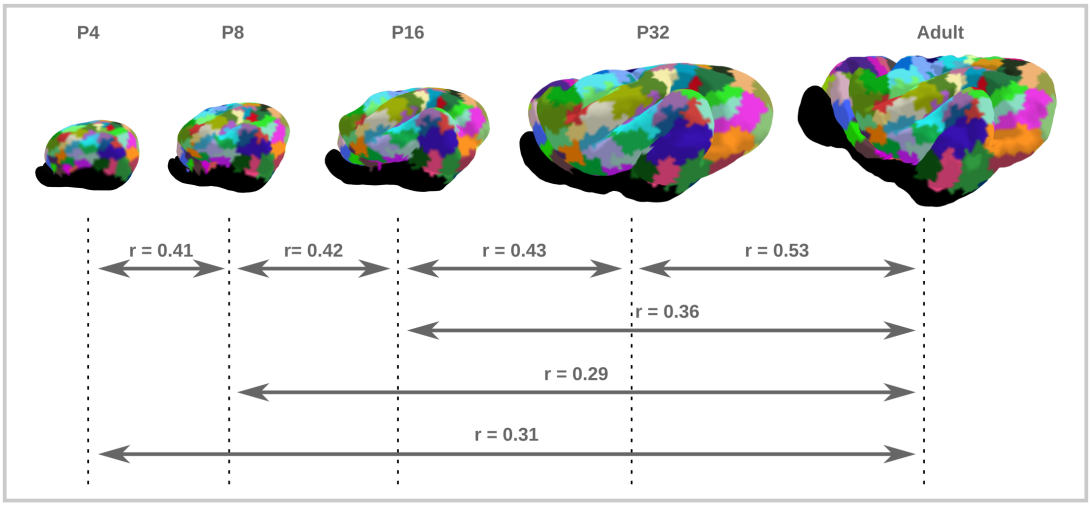

Figure 5.2: **Common random parcellation and correlation between connectivity matrices.** The brain surfaces display the common random parcellation used both for the histology and connectivity data (left hemisphere). The correlations are Pearson correlations between the binarized connectivity matrices.

5.2.3 Histology to MRI correspondence

The corresponding time points (P4, P8, P16 and P32) from the histological sections and MRI data were registered using a sequence of linear and non linear registrations (ANTs SyN, Avants et al. 2011; Tustison and Avants 2013) described in section 2.5 'Datasets and processing pipelines/Establishing the correspondence between the histological and MRI space'. For each MRI dataset a corresponding surface mesh was generated and a correspondence between the meshes across the time points was also established. A single 200 parcel random parcellation was computed and translated across the different time points (Figure 5.2). The distance between the brain regions was computed as the euclidean distance between the centroids of the parcels. Furthermore, each histological profile was associated to its closest node on the mesh and assigned to the corresponding parcel. This allowed us to use a common parcellation for the MRI and histological data. In this analysis, we computed the average profile per parcel as a representation of the parcel. This allowed us to keep as much of the variability of the profiles as possible.

5.2.4 Statistical analysis

5.2.4.1 Profile similarity

In order to estimate the similarity between pairs of histological profiles, we computed their Pearson correlation and applied a Fisher Z transformation using scipy (Virtanen et al. 2020).

5.2.4.2 Comparison of the histological profiles and presence of connections

In this analysis, we evaluated the relationship between each of the time points of the histological data with each of the time points of the connectivity data. We performed a Logistic

Regression (Garreta and Moncecchi 2013), using connectivity as dependent variable and cytoarchitectonic similarity and euclidean distance between regions as estimators, in order to quantify the capacity to predict connectivity from our two estimators. We split the dataset randomly into 100 sets with 80% of the data as training dataset and 20% as testing dataset for cross validating the results. We computed the regression for both estimators combined (bivariate) and each estimator independently (univariate). We then computed the average area under the curve (AUC) and the standard deviation of the AUCs for the 100 iterations in order to evaluate the capacity of the model to predict connectivity better than chance. We considered that connectivity could be predicted better than chance when its average AUC was superior to 0.50+2*std(AUC). The average coefficients indicated the type of relationship (positive or negative) between the dependent variable and each of the estimators. Furthermore we used the likelihood ratio to test the improvement of the univariate model by using a bivariate one.

5.3 Results

The automated processing of the histological sections and the diffusion dataset allowed us to test the relationship between the similarity of cytoarchitecture, distance and the existence of connections for the whole brain and during its development.

Overall the bivariate model (cytoarchitectonic similarity and distance) could always predict connectivity better than chance with an AUC between 0.60 and 0.685 (std = 0.01, Supplementary table B.1) for all the combinaisons of time points between the dependent variable and the estimators. Distance could also always predict connectivity better than chance (AUC = [0.59 - 0.678], std = 0.01, Figure 5.3, Supplementary table B.2). The relationship with distance was consistently described by negative coefficients ranging from -0.06 to -0.26 (Supplementary table B.2).

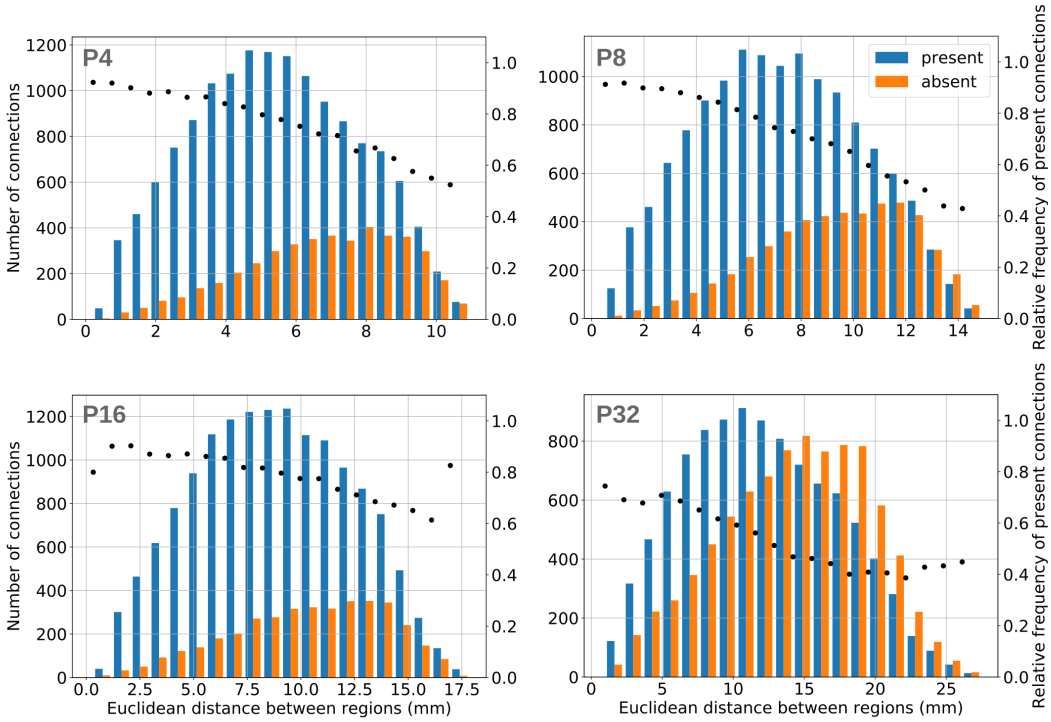

Figure 5.3: **Relationship between distance and presence or absence of connections.** Histogram representing the distribution of present (blue) or absent (orange) connections (y-axis left side) with the euclidean distance between brain regions (x-axis). The scatter plot represents the relative frequency of present connections (present/(present+absent connections), y-axis right side). For each of the graphs, we used the euclidean distance and connectivity data of the time point indicated on the figure (P4, P8, P16 and P32).

5.3.1 Individual cytoarchitectonic similarity was not consistently related to connectivity during development

First, we tested the ability of cytoarchitectonic similarity between each pair of regions to predict the existence or absence of interconnections at the same developmental stage. We observed that at P4 and P16, cytoarchitectonic similarity could not predict its current connectivity (P4: AUC = 0.497, std = 0.010; P16: AUC = 0.510, std = 0.009, Figure 5.4, Supplementary table B.3). At P8, we obtained a negative relationship between cytoarchitectonic similarity and connectivity (coef = -0.281, AUC = 0.551, std = 0.009). Finally at P32, cytoarchitectonic similarity could weakly predict the existence or absence of interconnections better than chance with a positive relationship (coef = 0.190, AUC = 0.528, std = 0.009).

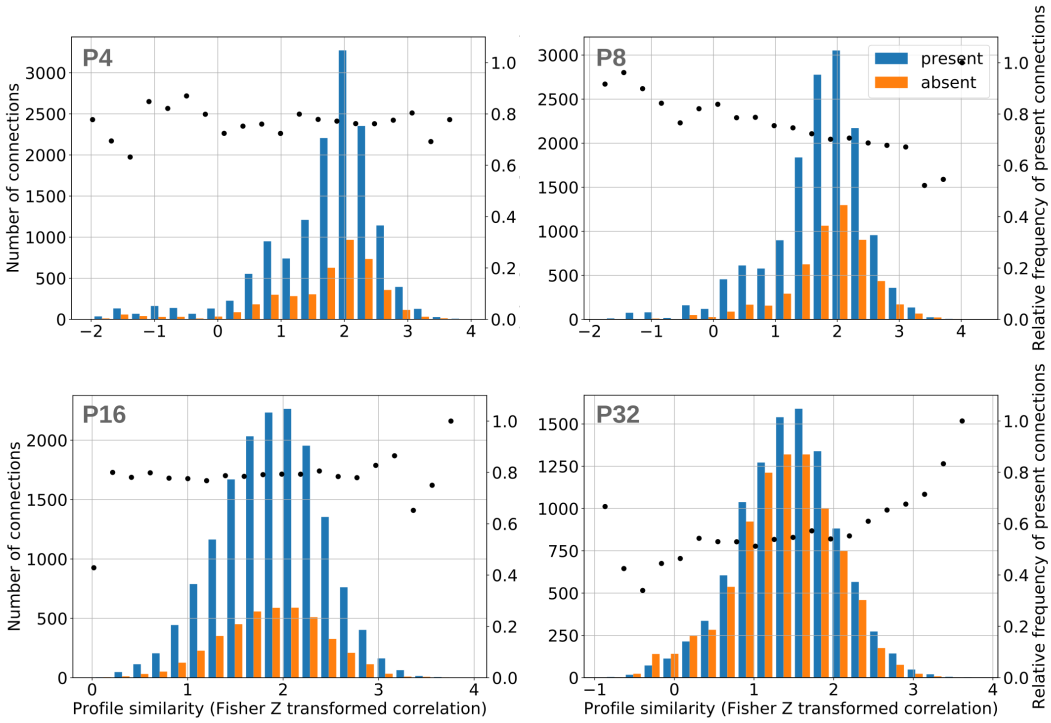

Figure 5.4: **Relationship between cytoarchitectonic similarity and presence or absence of connections.**
Histogram representing the distribution of present (blue) or absent (orange) connections (y-axis left side) with the Fisher Z transformed correlation between grey level profiles (x-axis). The scatter plot represents the relative frequency of present connections (present/(present+absent connections), y-axis right side). For each of the graphs, we used the z-score and connectivity data of the time point indicated on the figure (P4, P8, P16 and P32).

5.3.2 Cytoarchitectonic similarity was weakly related to connectivity at the adult stage

Cytoarchitectonic similarity at each of the time points could predict mature connectivity (adult stage) only slightly better than chance with an AUC between 0.529 and 0.572 (std = 0.008) (Supplementary table B.3), however cytoarchitectonic similarity was always positively related to connectivity (Figure 5.5, Figure 5.10, Supplementary table B.3).

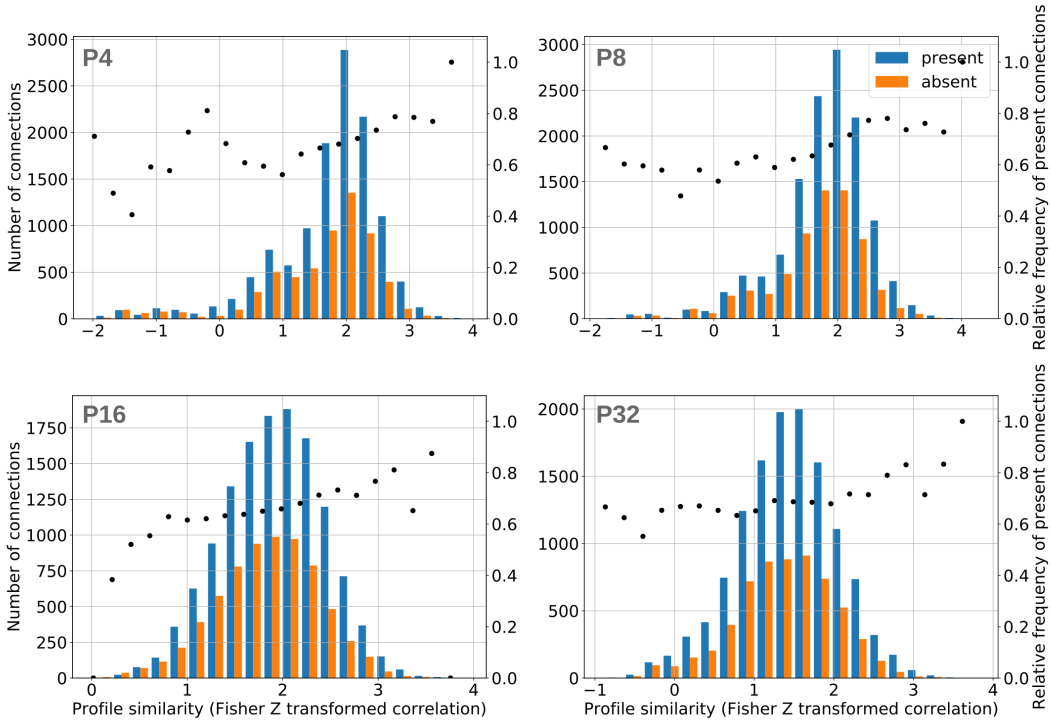

Figure 5.5: **Relationship between cytoarchitectonic similarity and connectivity from an adult ferret.**
Histogram representing the distribution of present (blue) or absent (orange) connections (y-axis left side) with the Fisher Z transformed correlation between grey level profiles (x-axis). The scatter plot represents the relative frequency of present connections (present/(present+absent connections), y-axis right side). For each of the graphs, we used the z-score indicated on the figure (P4, P8, P16 and P32) and the connectivity data from an adult ferret.

5.3.3 Cytoarchitectonic similarity was weakly related to connectivity at P32

Similarly to predicting the connectivity at the adult stage, we observed a weak relationship between cytoarchitectonic similarity at each of the time points and the connectivity at P32 (AUC = [0.528 - 0.584], std = 0.009, Supplementary table B.3). The relationship between cytoarchitectonic similarity and connectivity was also consistently described by positive coefficients (Figure 5.6, Figure 5.10, Supplementary table B.3).

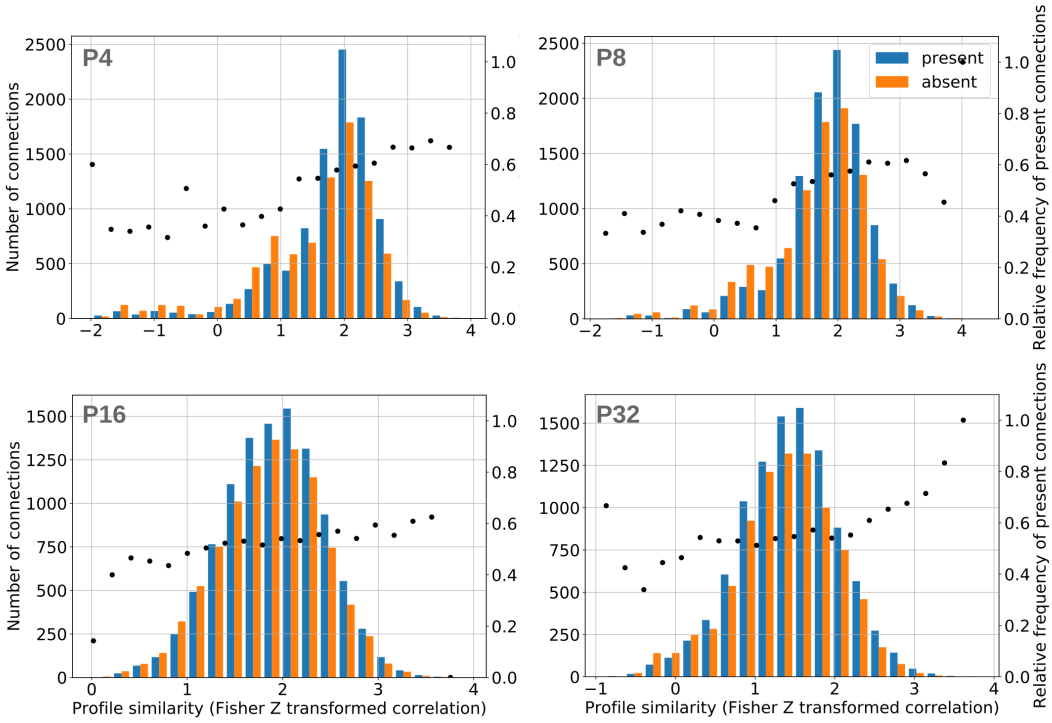

Figure 5.6: **Relationship between cytoarchitectonic similarity and connectivity from a ferret at P32.**
Histogram representing the distribution of present (blue) or absent (orange) connections (y-axis left side) with the Fisher Z transformed correlation between grey level profiles (x-axis). The scatter plot represents the relative frequency of present connections (present/(present+absent connections), y-axis right side). For each of the graphs, we used the z-score indicated on the figure (P4, P8, P16 and P32) and the connectivity data from a ferret at P32.

5.3.4 No positive relationship was observed between cytoarchitectonic similarity and connectivity at P16, P8 and P4

Connectivity at P16, P8 and P4 could either not be predicted by the cytoarchitectonic similarity at the different time points or could be predicted but with a negative relationship (Figure 5.7, 5.8 and 5.9, Figure 5.10, Supplementary table B.3).

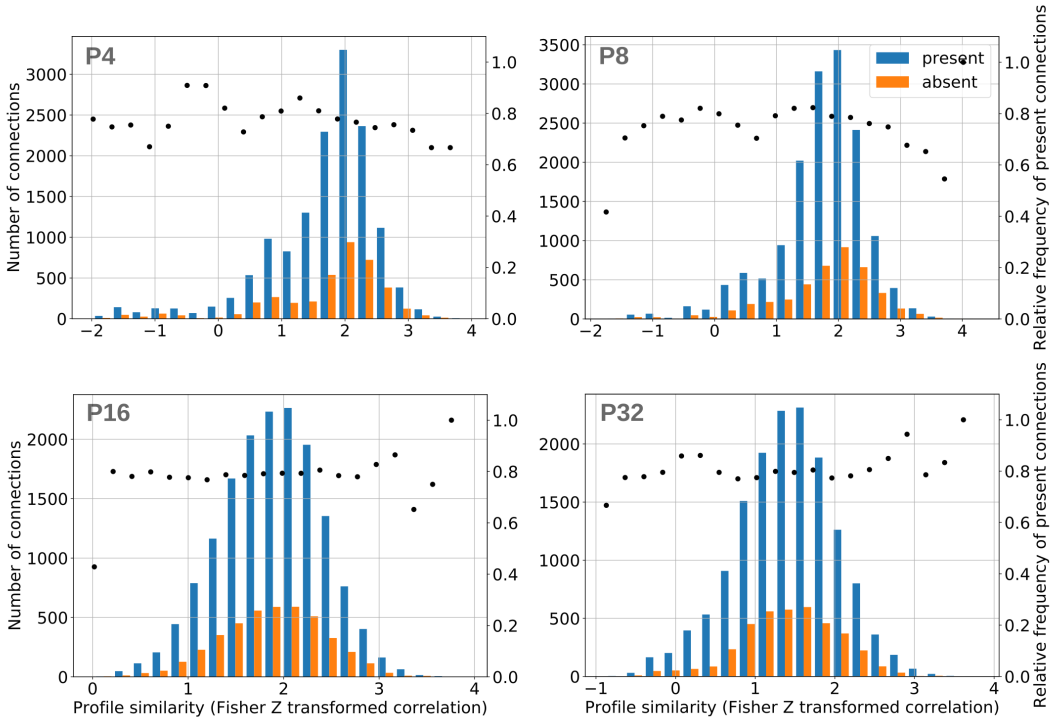

Figure 5.7: **Relationship between cytoarchitectonic similarity and connectivity from a ferret at P16.**
Histogram representing the distribution of present (blue) or absent (orange) connections (y-axis left side) with the Fisher Z transformed correlation between grey level profiles (x-axis). The scatter plot represents the relative frequency of present connections (present/(present+absent connections), y-axis right side). For each of the graphs, we used the z-score indicated on the figure (P4, P8, P16 and P32) and the connectivity data from a ferret at P16.

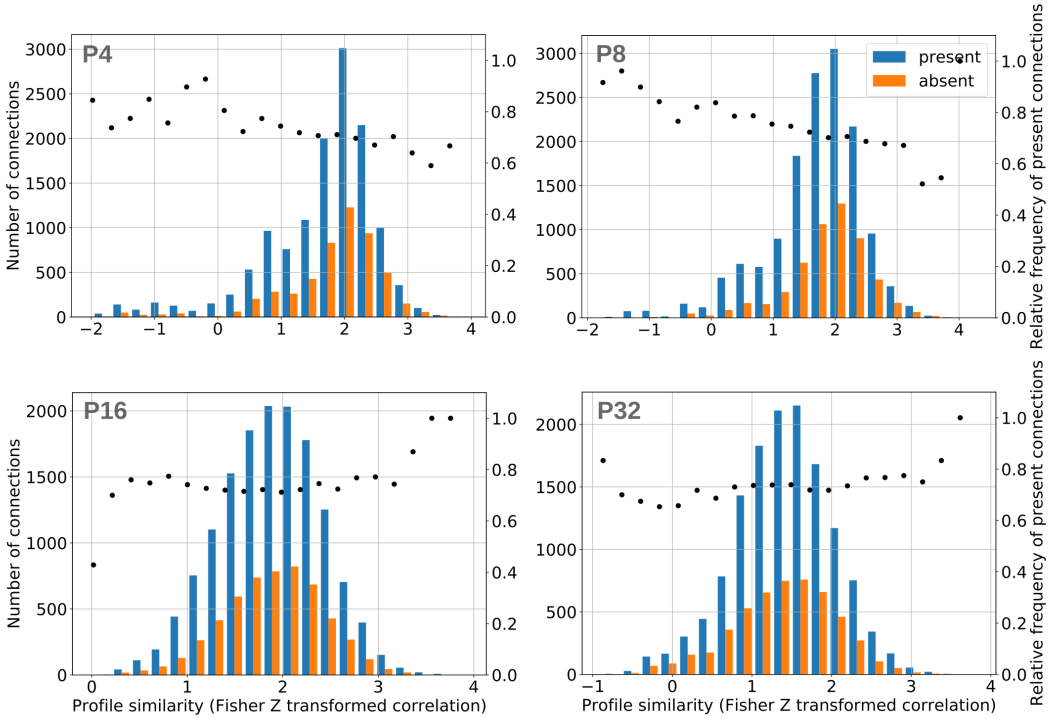

Figure 5.8: **Relationship between cytoarchitectonic similarity and connectivity from a ferret at P8.**
Histogram representing the distribution of present (blue) or absent (orange) connections (y-axis left side) with the Fisher Z transformed correlation between grey level profiles (x-axis). The scatter plot represents the relative frequency of present connections (present/(present+absent connections), y-axis right side). For each of the graphs, we used the z-score indicated on the figure (P4, P8, P16 and P32) and the connectivity data from a ferret at P8.

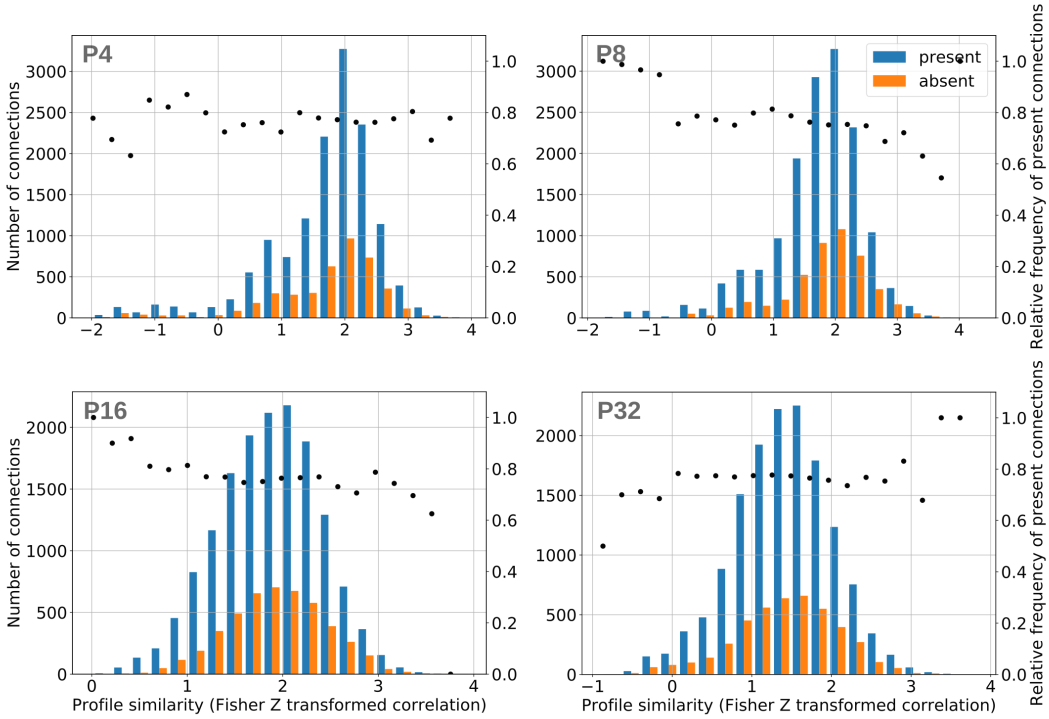

Figure 5.9: **Relationship between cytoarchitectonic similarity and connectivity from a ferret at P4.**
Histogram representing the distribution of present (blue) or absent (orange) connections (y-axis left side) with the Fisher Z transformed correlation between grey level profiles (x-axis). The scatter plot represents the relative frequency of present connections (present/(present+absent connections), y-axis right side). For each of the graphs, we used the z-score indicated on the figure (P4, P8, P16 and P32) and the connectivity data from a ferret at P4.

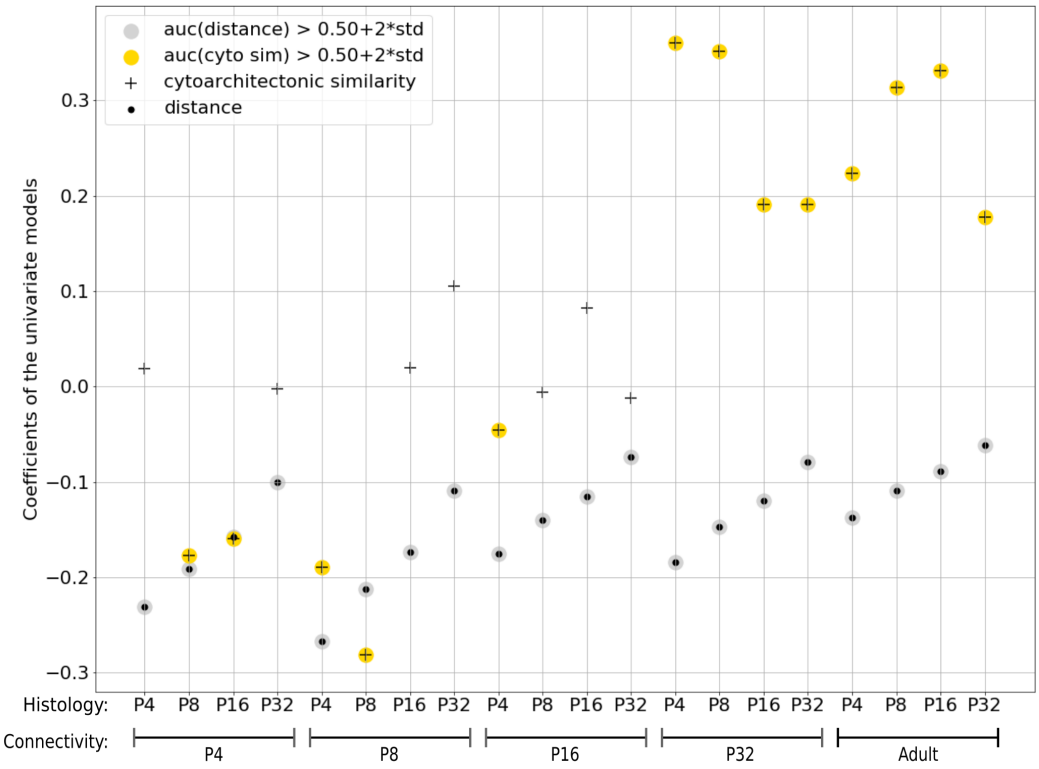

Figure 5.10: **Summary representation of the coefficients of the univariate logistic regression models.**
On the x-axis the time points of both the histology and connectivity datasets are represented. The coefficients from the model using cytoarchitectonic similarity as an estimator for connectivity are represented by a plus (+). If the AUC is more than two standard deviations away from 0.50, we considered that we can predict connectivity better than chance and the + was labelled in yellow. Similarly, for the univariate model using distance as estimator, the coefficients were represented by black dots (●) and were labelled in grey if connectivity could be predicted better than chance.

5.3.5 Distance contributed most to the predictions

Subsequently, the model using only cytoarchitectonic similarity was consistently improved in the bivariate model (likelihood ratio p-values < 10^{-3}, Figure 5.11, Supplementary table B.2 and B.3). In the cases where both univariate models (cytoarchitectonic similarity and distance) could predict connectivity, we observed that both estimators contributed to the prediction, however the distance model best improved the prediction. This was shown by a higher difference in log-likelihood between the distance only model and the bivariate model than between the cytoarchitecture only model and the bivariate model (Figure 5.11, Supplementary table B.1, B.2 and B.3).

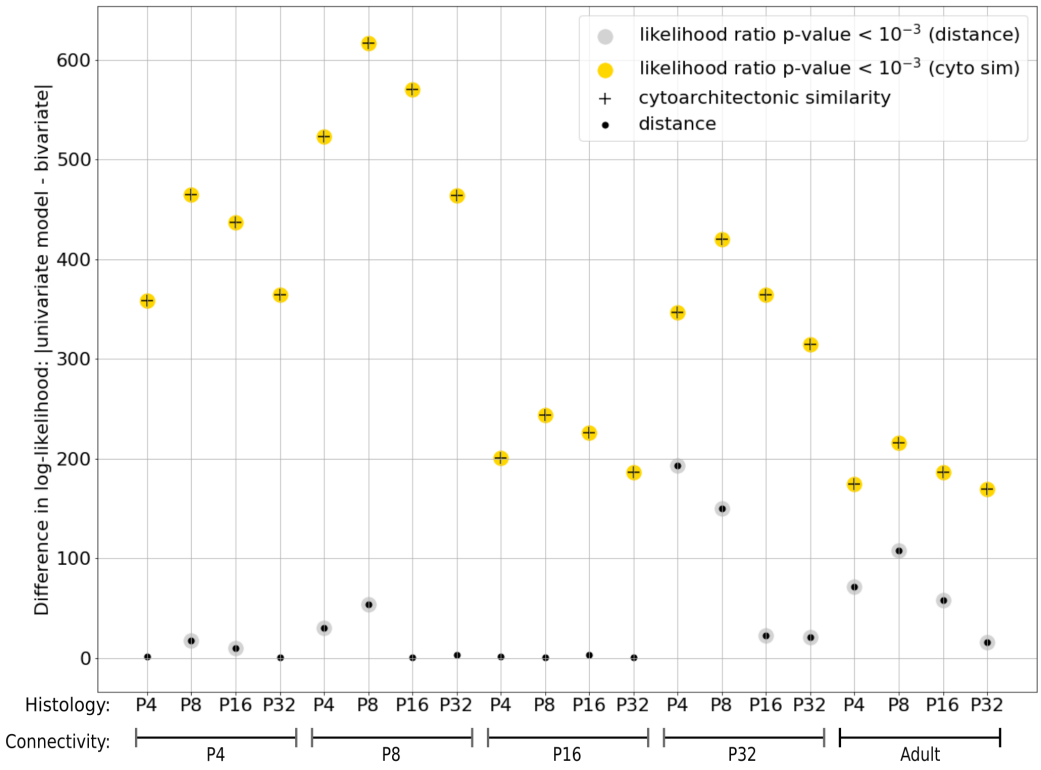

Figure 5.11: **Summary representation of the difference in log-likelihood between the univariate and bivariate models.**
On the x-axis the time points of both the histology and connectivity datasets are represented. The difference in absolute value between the log-likelihood of the univariate models with the log-likelihood of the bivariate model are indicated respectively with a plus (+) for the univariate model using cytoarchitectonic similarity and a black dot (●) for the one using distance. A statistical improvement of the univariate model in the bivariate model was identified by a p-value of the likelihood ratio under 10^{-3} and is labelled by a yellow circle for the univariate model using cytoarchitectonic similarity and in grey for the one using distance.

5.4 Partial discussion

In this study, we investigated the relationship between cytoarchitectonic similarity, distance and connectivity during the development of the ferret brain. We observed that the bivariate model including both cytoarchitectonic similarity and distance could consistently predict connectivity at all the time points with a higher contribution of distance in the prediction (Figure 5.11). When studying the relationship between distance alone as a predictor for connectivity, we consistently observed that two regions are more likely to be interconnected if they are in close physical proximity to each other. This relationship is recognized not only as a technical bias of diffusion tractography (Roberts et al. 2016; Liptrot, Sidaros, and Dyrby 2014) but also as a biological principle for preferential interconnection (Ercsey-Ravasz et al. 2013; Hilgetag et al. 2016). On the one hand, the spatial bias of diffusion tractography relies on the step-wise propagation of streamlines from a seed, causing the propagation of

the uncertainties along the length of the tracts (Liptrot, Sidaros, and Dyrby 2014). On the other hand, spatial proximity has been shown to be a factor for preferential interconnection as a way to minimize wiring costs (Ercsey-Ravasz et al. 2013). The configuration of the cortical networks following an exponential distance rule optimizes its efficiency (inverse of the shortest path length) by the formation of communities (Ercsey-Ravasz et al. 2013). As such, the two factors remain challenging to disentangle.

Although cytoarchitectonic similarity of ferrets as young as P4 could only weakly predict the presence or absence of connections of the ferrets at P32 and adult stage (AUC = [0.528 - 0.584], std = 0.009), we observed a positive relationship between cytoarchitectonic similarity and connectivity, indicating that two brain regions are more likely to be interconnected if they have a similar cytoarchitectonic organization. A positive relationship between cytoarchitectonic similarity and the presence of interconnections similarly reflected the organization of mature brains in the mouse (Goulas, Uylings, and Hilgetag 2017), cat (Beul, Grant, and Hilgetag 2015), marmoset (Majka et al. 2016), macaque (Beul and Hilgetag 2019) and human (Goulas et al. 2016; Wei et al. 2019). Contrary to the models predicting the connectivity at P32 and adult stage, the cortico-cortical connectivity of ferrets at P4, P8 and P16 could either not be predicted by the logistic regression or showed a negative relationship between cytoarchitectonic similarity and the presence of interconnections. This suggests that (1) the positive relationship between cytoarchitectonic similarity and connectivity is most likely a characteristic of mature brains or (2) it may indicate the failure of diffusion tractography to track reliably immature connectivity.

1. At P21, the ferret brain is only composed of a few radial glia cells, indicating the end of neuronal migration and the number of axons increases significantly (Voigt 1989). At 4 weeks of age, neuronal migration in the ferret is complete and all cortical layers are present (Chapter 4, Voigt, De Lima, and Beckmann 1993). The end of neuronal migration and the presence of all cortical layers has been described to coincide with a strong increase in synaptogenesis and the rapid development of cortico-cortical connections (Voigt, De Lima, and Beckmann 1993). Furthermore, we observed a higher correlation between the connectivity at P32 and the adult stage than between any other stages, suggesting that ferret brain connectivity at P32 reaches a state which resembles strongly mature connectivity. Overall this suggests that the footprint of a mature cytoarchitectonic organization is present early in development as we could predict mature connectivity (P32 and adult) from the cytoarchitecture of ferrets as young as P4. In addition, our results suggest that the footprint of a mature cytoarchitectonic organization is present prior to the footprint of mature connectivity. The footprint of cytoarchitecture reflected by the grey level profiles could either be interpreted as a representation of the type of cytoarchitectonic organization or as an indicator of cortical maturation. As described previously (Chapter 4), the shape of the grey level profiles (steepness of the slope between the supra- and infragranular layers) reflected the level of differentiation of the supra- and infragranular layers, which we used as an indicator for cytoarchitectonic maturation. This could postulate that two regions developing synchronously are more likely to be connected at the mature stage, however larger sample sizes are needed to confirm this.

2. Diffusion tractography is a valuable tool for estimating whole brain structural connectivity non-invasively. Its limitations such as the presence of false-positives or its capability to track crossing-fibers have been extensively studied on mature brains, using phantom datasets or compared to the results from tract-tracing experiments (Maier-Hein et al. 2017; Jones, Knösche, and Turner 2013; Thomas et al. 2014; Schilling et al.

2018; Tournier, Calamante, and Connelly 2012; Dell'Acqua and Tournier 2019). Although the accuracy of diffusion tractography has been further tested in fetal human brains (Jakab et al. 2017; Song et al. 2018), validations by observations at the microscale are rare (Mitter et al. 2015). During early development brain tissue is subject to major modifications such as neurogenesis, neuronal migration and maturation as well as axonal growth and myelination. These events induce modifications of the tissue properties visible in the diffusion MRI signals especially by an increase of the fractional anisotropy (FA) in the WM and a decrease in the GM (Barnette et al. 2009). The inversion of the FA signal to a high anisotropy in the WM and low anisotropy in the GM occur around P20 in the ferret (Barnette et al. 2009). The FA contrasts beyond P20 (high FA in the WM and low FA in the GM) are then similar to the contrasts observed in mature brains (Barnette et al. 2009). This coincides with what we observed in our FA contrasts (Supplementary figure B.1) indicating a mature-like connectivity present at P32. It is nonetheless essential to further validate the use of diffusion tractography in immature brains. Although the sample size in our study is limited, it seems primordial to focus on the interpretability of diffusion signals in developing brains.

Overall we recognize that our AUC may be considered as low values (AUC < 0.7) and thus only provide poor discrimination, indicating a low ability of the classifier (Hosmer and Lemeshow 2004). Furthermore, our sample size was limited and did not allow us to provide a confident estimation of the relationships, however this study has provided a first estimate of the evolution of the relationship between cortical lamination and cortico-cortical connectivity during early brain development. Further testing, including the increase of the sample size and the validation of diffusion tractography in immature brains, will be required to confirm our results.

To conclude, our results for the mature ferret (P32 and adult stage) confirm a positive relationship between cytoarchitectonic similarity and connectivity and a negative relationship between distance and connectivity previously observed in other mature mammals. Our unique dataset allowed us to further study the relationship between cytoarchitectonic similarity, distance and connectivity during the early stages of brain development. Although there is a need for validation of the interpretability of diffusion tractography in immature brains, our study suggests that the footprint of a mature cytoarchitectonic organization is present prior to the footprint of mature connectivity.

Chapter 6

Discussion

The aim of this thesis was to apply a multi-scale and multimodal approach to characterize ferret brain development. This was achieved in three individual studies emphasizing the different advantages of multi-scale and multimodal approaches. (1) Firstly, we used a multi-scale and multimodal approach to investigate the ability of different MRI tractography algorithms to reliably map structural connectivity of the ferret brain. (2) Secondly, we developed a semi-automated pipeline for processing microscale histological sections and retrieving whole brain quantifications. (3) Thirdly, we used a multimodal approach to obtain an integrated characterization of whole brain structural development. Furthermore, we provided "ferret-specific" outcomes regarding the development of brain structure. In addition, the two main datasets (MRI and histological slices) used in this work have been made freely available through the FIIND project (https://neuroanatomy.github.io/fiind/).

6.1 A multi-scale and multimodal approach for evaluating modalities

MRI data allows one to non-invasively obtain whole brain quantifications of morphological (structural MRI, Sawada et al. 2013), functional (functional MRI, Zhou et al. 2016) and structural connectivity (diffusion MRI, Das and Takahashi 2018). MRI is therefore a valuable tool for clinical studies (non-invasivity) and allows the collection of extensive datasets of healthy and pathological subjects (for example: Human Connectome Project, Van Essen et al. 2013; Abide, Di Martino et al. 2014). Although large sampling sizes are available for MRI data, its coarse resolution (around 1mm voxel size for human brain scans) and ambiguous signal (MRI uses proxies to biological tissues and processes) require further investigation for elaborating biologically reliable interpretations of the data (Thomas et al. 2014). For these reasons, validation appears as a key step in evaluating current MRI methodologies (Dyrby et al. 2018). For example, a number of validation studies have been utilizing phantom datasets to validate diffusion tractography (Maier-Hein et al. 2017; Sarwar, Ramamohanarao, and Zalesky 2019), however these studies can only provide an estimation of the reproducibility of the tractography algorithms as these phantoms are based on diffusion MRI data.

In this work, we undertook a multi-scale and multimodal approach to investigate the reliability of diffusion tractography in mapping structural connectivity (Chapter 3, Delettre et al. 2019). We used histological tract-tracing experiments as the ground truth for structural connectivity. Tract-tracing experiments allowed us to use quantifications reported from observations at the microscale (cellular level) (Zingg et al. 2014; Markov et al. 2014b; Bota, Sporns, and Swanson 2015; Bizley et al. 2015). Microscale experiments present the advantage of acquiring unambiguous, high resolution observations of biological tissue. However, such experiments are invasive, highly time consuming (manual processing of the data) and require the expert scientists or technicians to carry out the histological experiments. As a consequence microscale histological quantifications and datasets are primarily obtained from laboratory specimens, often only available with reduced sample sizes and limited regions of interest. Furthermore, such studies are not feasible for longitudinal studies (due to the invasiveness of the experiments) or in clinical contexts (due to the ethical concerns).

Although histological microscale experiments are highly time consuming, they are essential in validating different imaging modalities at the whole brain level against their microscale equivalent as no other ground-truth is currently available. Studies performed in the macaque (Donahue et al. 2016; Zhang et al. 2018; Azadbakht et al. 2015; Schilling et al. 2019b), squirrel monkey (Schilling et al. 2019a; Gao et al. 2013), pig (Knösche et al. 2015), mouse (Calabrese et al. 2015) and rat (Sinke et al. 2018), have compared the structural connectivity computed by diffusion tractography with the results from histological experiments. These studies have shown that diffusion tractography provide a good estimation of the structural connectivity, however few studies have expored the ability of various diffusion tractography approaches to estimate structural connectivity weights (Gao et al. 2013). Our study in Chapter 3 allowed us to validate the use of diffusion tractography in the adult ferret, for which connectivity data is rare. Furthermore, we provided quantified estimations of the performances of a set of tractography algorithms. Finally, we made our connectivity data available to the community through our publication (Delettre et al. 2019).

Validation is all the more necessary for animal models for which few comparable studies are available. Additionally, our study in Chapter 5 highlighted the need for a more extensive

validation of tractography in the early stages of development (during neuronal proliferation and the establishment of cortico-cortical connectivity), as only a few of studies validate fetal diffusion tractography with observations at the microscale level (Mitter et al. 2015). As with tractography validation studies in adult specimens, developmental studies similarly compare the reproducibility of results across scans or the match to the postnatal scans (Jakab et al. 2017; Song et al. 2018).

6.2 Automating histological data processing for whole brain quantifications

Microscale histological experiments provide high resolution direct observations of biological tissues, but traditionally require manual processing of the data. Processing this data is therefore highly time consuming, subject to observer dependent variations and possible biases. As a consequence, the microscale analyzes are based on limited sample sizes and a few regions of interest. In order to benefit from both microscale observations and obtain whole brain quantifications, the processing of datasets imaged at the microscale can be automatized. Although automatized processing pipelines allow the acquisition of whole brain histological datasets with larger sample sizes in a shorter time period, they do provide coarser results. The reason for this is due to the use of a proxy requirement for the biological feature, such as grey levels for cell density (Wree, Schleicher, and Zilles 1982) or grey level profiles for cortical lamination (Schleicher et al. 1999; Wagstyl et al. 2018). Furthermore, features such as cell type remain difficult to elucidate automatically (Inglis et al. 2008; García-Cabezas et al. 2016).

In our study in Chapter 4, we automatized the processing of Nissl brain slices to quantify the maturation of cortical lamination. Our histological slices were digitized at 20X on a slide scanner (Zeiss Axioscan Z1), which allowed the automatization of the processing pipeline, requiring only minimal manual interventions, and the sharing of our dataset (https://neuroanatomy.github.io/fiind/). The automatization of our processing pipeline allowed us to obtain whole brain, observer independent quantifications of the cortical lamination of the ferret brain. Furthermore, the rapid processing of the data allowed us to characterize the maturation of the cytoarchitectonic organization of the ferret at four time points. Our grey level profiles quantifying the cortical lamination highlighted the inside-out pattern of development of the cortical layers. In addition the brain maps depicting the distribution of grey level profile clusters underlined a laterodorsal gradient of maturation of the cortical lamination until four weeks postnatally where all layers are present. These findings as well as delineation of such cytoarchitectonic organization would have required several months of processing and analysis by an expert anatomist or technician, before the similar conclusions could be drawn.

6.3 A multimodal approach for studying whole brain structure

Multimodal approaches allow one to collectively study several biological features of the brain (i.e. morphology, cytoarchitecture, structural connectivity, functional connectivity). Although

univariate approaches can provide a precise description of a given feature, multivariate analyses are required for an integrated characterization of the brain (Miyawaki 2016; Beul and Hilgetag 2019). Multimodal approaches have been used to characterize the relationship between cytoarchitecture and structural connectivity (Barbas 1986; Beul, Grant, and Hilgetag 2015; Goulas, Uylings, and Hilgetag 2017) or between structural and functional connectivity (Messé et al. 2020), which allow the elucidation of principles of brain organization (Goulas et al. 2019).

In Chapter 5, the multimodal approach gave us a more holistic view on brain structure by integrating information about both structural connectivity and cytoarchitecture. We studied the relationship between whole brain cytoarchitecture (processing pipeline in Chapter 4) and whole brain connectivity (mature connectivity validated in Chapter 3) development. In order to compare both modalities, we registered the MRI slices to the histological slices as a series of 2D registrations. We used a random parcellation as a means to summarize the data in a common space for the statistical analysis.

Furthermore, the use of multimodal approaches in longitudinal studies allowed us to investigate the sequence of biological processes. In our study (Chapter 5), the bimodal dataset enabled us to investigate the relationship of cytoarchitecture and connectivity across time points and to conclude on a mature footprint of cytoarchitecture present prior to the mature footprint of structural connectivity. Although multi-scale approaches provide an integrated characterization of the brain, such as information about the relationships between different biological features and their sequence of development, these approaches require thorough validation of the chosen modalities for reliable conclusions as the biases of each of the modalities can be confounded in the results.

Our multimodal approach allowed us to validate the existence of a positive relationship between cytoarchitectonic similarity and the presence of interconnections in the mature ferret (preferential interconnection of brain regions with similar cytoarchitectonic organization), which has previously been observed in the mouse, cat, marmoset, macaque and human. The automated processing of our dataset allowed us to further study this relationship during the early development of the ferret cytoarchitecture and connectivity. Overall, we observed that the positive relationship between cytoarchitectonic organization and connectivity was not maintained for the earlier time points in development (P4, P8 and P16) while the cytoarchitecture at any time point could predict mature connectivity. Although diffusion tractography from immature brains requires further validation, this study suggested that the footprint of mature cytoarchitecture is present prior to the footprint of mature connectivity.

6.4 Limitations and future directions

Our results provided a whole brain characterization of the development of brain structure (cytoarchitecture and connectivity) in the ferret as well as a validation of diffusion tractography in the mature ferret brain, however we acknowledge that our sample sizes are limiting. Despite the small sample size; our MRI dataset was scanned *ex vivo*, at 0.24 mm isotropic voxels, with high b-values (2000 and 4000 s/mm^2) and in 200 directions. This resulted in up to 37 hours of scanning time per subject for high resolution scans. Furthermore, the histological slices were scanned at 20X and also required approximately 30 hours of scanning time per brain to obtain a 0.22 um/pixel resolution. This demonstrates the extensive costs and

time resources required for such studies. Furthermore, these costs are escalated with larger sample sizes and this is often easily forgotten. Fortunately, all scans (MRI and histological slices) have been made freely available through the FIIND project for further studies. This is important for not only extending the longevity of such pioneering research but also for the advancement of this research through collaborative initiatives that encourage sharing of scientific resources.

Although microscale experiments are highly valuable tools for validating different modalities and precisely characterizing biological processes, due to its inherent characteristics (invasivity, time-consuming) we can not expect every study to provide its own corresponding microscale dataset as scientific resources are not limitless. It is therefore essential to share the available datasets and to use comparative studies to elucidate common principles of organization (Goulas et al. 2019) and development. Although humans are the ideal and desired experimental subject, numerous ethical considerations make human research difficult. Thus animal models, such as the ferret, play an important role in human brain research.

The brain is highly complex and can be studied across different scales and different features (morphology, cytoarchitecture, structural and functional connectivity, behavior). It is necessary to not only study each aspect in isolation but also collectively to obtain a better understanding of this complex ensemble. Importantly, zooming-in and out (multi-scale) allows scientists to alternate between a precise description of the biological processes at the microscale and the summation of these processes into whole brain principles.

Finally, this thesis provides a validation of diffusion tractography in the mature ferret brain, a whole brain characterization of the development of cytoarchitecture as well as its relationship to the development of cortico-cortical connectivity. Furthermore, the datasets generated by this thesis are valuable resources for further studies in the ferret and brain development. The adult connectivity dataset has already been used for modeling the brain activity recorded by ECoG (Messé et al. 2020) and will be used to model brain dynamics, similarly to what has been done with human tissue in The Virtual Brain (Leon et al. 2013). Finally, our dataset could be incorporated to create a virtual developing ferret with complementary cytoarchitecture information and resources.

Bibliography

Andersson, Jesper L R and Stamatios N Sotiropoulos (2016). "An integrated approach to correction for off-resonance effects and subject movement in diffusion MR imaging". en. In: *Neuroimage* 125, pp. 1063–1078.

Arroyo, M and S E Reed (1977). "The use of ferret trachea organ cultures for therapeutic studies of anti-influenzal drugs. I. Evaluation of the model in comparison with infection in humans". en. In: *J. Antimicrob. Chemother.* 3.6, pp. 601–607.

Atapour, Nafiseh et al. (2019). "Neuronal Distribution Across the Cerebral Cortex of the Marmoset Monkey (Callithrix jacchus)". en. In: *Cereb. Cortex* 29.9, pp. 3836–3863.

Auzias, Guillaume, Olivier Coulon, and Andrea Brovelli (2016). "MarsAtlas: A cortical parcellation atlas for functional mapping". en. In: *Hum. Brain Mapp.* 37.4, pp. 1573–1592.

Avants, Brian B et al. (2011). "A reproducible evaluation of ANTs similarity metric performance in brain image registration". en. In: *Neuroimage* 54.3, pp. 2033–2044.

Azadbakht, Hojjatollah et al. (2015). "Validation of High-Resolution Tractography Against In Vivo Tracing in the Macaque Visual Cortex". en. In: *Cereb. Cortex* 25.11, pp. 4299–4309.

Barbas, H (1986). "Pattern in the laminar origin of corticocortical connections". en. In: *J. Comp. Neurol.* 252.3, pp. 415–422.

Barnette, Alan R et al. (2009). "Characterization of brain development in the ferret via MRI". en. In: *Pediatr. Res.* 66.1, pp. 80–84.

Basser, Peter J et al. (2000). "In vivo fiber tractography using DT-MRI data". In: *Magn. Reson. Med.* 44.4, pp. 625–632.

Batalle, Dafnis et al. (2017). "Early development of structural networks and the impact of prematurity on brain connectivity". en. In: *Neuroimage* 149, pp. 379–392.

Berman, N E, J K Johnson, and R M Klein (1997). "Early generation of glia in the intermediate zone of the developing cerebral cortex". en. In: *Brain Res. Dev. Brain Res.* 101.1-2, pp. 149–164.

Beul, Sarah F, Helen Barbas, and Claus C Hilgetag (2017). "A predictive structural model of the primate connectome". en. In: *Sci. Rep.* 7, p. 43176.

Beul, Sarah F, Simon Grant, and Claus C Hilgetag (2015). "A predictive model of the cat cortical connectome based on cytoarchitecture and distance". In: *Brain Structure and Function* 220.6, pp. 3167–3184.

Beul, Sarah F and Claus C Hilgetag (2019). "Neuron density fundamentally relates to architecture and connectivity of the primate cerebral cortex". en. In: *Neuroimage* 189, pp. 777–792.

Bizley, Jennifer K and Andrew J King (2009). "Visual influences on ferret auditory cortex". en. In: *Hear. Res.* 258.1-2, pp. 55–63.

Bizley, Jennifer K et al. (2015). "Cortico-cortical connectivity within ferret auditory cortex". en. In: *J. Comp. Neurol.* 523.15, pp. 2187–2210.

Borrell, Víctor (2018). "How Cells Fold the Cerebral Cortex". In: *The Journal of Neuroscience* 38.4, pp. 776–783.

Bota, Mihail, Olaf Sporns, and Larry W Swanson (2015). "Architecture of the cerebral cortical association connectome underlying cognition". en. In: *Proc. Natl. Acad. Sci. U. S. A.* 112.16, E2093–101.

Brett, Matthew et al. (2018). "nipy/nibabel: 2.3.0". In:

Brodmann, Korbinian (1909). *Vergleichende Lokalisationslehre der Grosshirnrinde in ihren Prinzipien dargestellt auf Grund des Zellenbaues*. de.

Calabrese, Evan et al. (2015). "A diffusion MRI tractography connectome of the mouse brain and comparison with neuronal tracer data". en. In: *Cereb. Cortex* 25.11, pp. 4628–4637.

Charvet, Christine J, Diarmuid J Cahalane, and Barbara L Finlay (2015). "Systematic, cross-cortex variation in neuron numbers in rodents and primates". en. In: *Cereb. Cortex* 25.1, pp. 147–160.

Clancy, B, R B Darlington, and B L Finlay (2001). "Translating developmental time across mammalian species". en. In: *Neuroscience* 105.1, pp. 7–17.

Collins, Christine E et al. (2010). "Neuron densities vary across and within cortical areas in primates". en. In: *Proc. Natl. Acad. Sci. U. S. A.* 107.36, pp. 15927–15932.

Collins, D Louis et al. (1995). "Automatic 3-D model-based neuroanatomical segmentation". In: *Hum. Brain Mapp.* NATO ASI Series 3.3, pp. 190–208.

Craddock, R Cameron et al. (2012). "A whole brain fMRI atlas generated via spatially constrained spectral clustering". en. In: *Hum. Brain Mapp.* 33.8, pp. 1914–1928.

Das, Avilash and Emi Takahashi (2018). *Characterization of White Matter Tracts by Diffusion MR Tractography in Cat and Ferret that Have Similar Gyral Patterns*.

Delettre, Céline et al. (2019). "Comparison between diffusion MRI tractography and histological tract-tracing of cortico-cortical structural connectivity in the ferret brain". en. In: *Netw Neurosci* 3.4, pp. 1038–1050.

Dell, Leigh-Anne et al. (2019a). "Cortical and thalamic connectivity of occipital visual cortical areas 17, 18, 19 and 21 of the domestic ferret (Mustela putorius furo)". In: *Journal of comparative neurology*.

– (2019b). "Cortical and thalamic connectivity of posterior parietal visual cortical areas PPc and PPr of the domestic ferret (Mustela putorius furo)". In: *Journal of comparative neurology*.

– (2019c). "Cortical and thalamic connectivity of temporal visual cortical areas 20a and 20b of the domestic ferret (Mustela putorius furo)". In: *Journal of comparative neurology*.

Dell'Acqua, Flavio and J-Donald Tournier (2019). "Modelling white matter with spherical deconvolution: How and why?" en. In: *NMR Biomed.* 32.4, e3945.

Dennis, Emily L and Paul M Thompson (2013). "Typical and atypical brain development: a review of neuroimaging studies". en. In: *Dialogues Clin. Neurosci.* 15.3, pp. 359–384.

Desikan, Rahul S et al. (2006). "An automated labeling system for subdividing the human cerebral cortex on MRI scans into gyral based regions of interest". en. In: *Neuroimage* 31.3, pp. 968–980.

Di Martino, A et al. (2014). "The autism brain imaging data exchange: towards a large-scale evaluation of the intrinsic brain architecture in autism". en. In: *Mol. Psychiatry* 19.6, pp. 659–667.

Dombrowski, S M, C C Hilgetag, and H Barbas (2001). "Quantitative architecture distinguishes prefrontal cortical systems in the rhesus monkey". en. In: *Cereb. Cortex* 11.10, pp. 975–988.

Donahue, Chad J et al. (2016). "Using Diffusion Tractography to Predict Cortical Connection Strength and Distance: A Quantitative Comparison with Tracers in the Monkey". en. In: *J. Neurosci.* 36.25, pp. 6758–6770.

Dong, Hong Wei and The Allen Institute for Brain Science (2008). *The Allen Reference Atlas: A Digital Color Brain Atlas of the C57BL/6J Male Mouse*. en. Wiley.

Dubois, Jessica et al. (2019). "The dynamics of cortical folding waves and prematurity-related deviations revealed by spatial and spectral analysis of gyrification". en. In: *Neuroimage* 185, pp. 934–946.

Dyrby, Tim B et al. (2011). *An ex vivo imaging pipeline for producing high-quality and high-resolution diffusion-weighted imaging datasets*.

Dyrby, Tim B et al. (2018). "Validation strategies for the interpretation of microstructure imaging using diffusion MRI". In: *NeuroImage* 182, pp. 62–79.

Economo, Constantin Freiherr von and Georg N Koskinas (1925). *Die cytoarchitektonik der hirnrinde des erwachsenen menschen*. de.

Economo, Constantin von (2009). *Cellular Structure of the Human Cerebral Cortex*. en. Karger Medical and Scientific Publishers.

Empie, Kristen, Vijayeta Rangarajan, and Sandra E Juul (2015). "Is the ferret a suitable species for studying perinatal brain injury?" In: *International Journal of Developmental Neuroscience* 45.1, pp. 2–10.

Engel, Andreas K et al. (2013). "Intrinsic coupling modes: multiscale interactions in ongoing brain activity". en. In: *Neuron* 80.4, pp. 867–886.

Ercsey-Ravasz, Mária et al. (2013). "A predictive network model of cerebral cortical connectivity based on a distance rule". en. In: *Neuron* 80.1, pp. 184–197.

Feng, Y et al. (2013). "Viscoelastic properties of the ferret brain measured in vivo at multiple frequencies by magnetic resonance elastography". en. In: *J. Biomech.* 46.5, pp. 863–870.

Fornito, Alex and Edward T Bullmore (2015). "Connectomics: a new paradigm for understanding brain disease". en. In: *Eur. Neuropsychopharmacol.* 25.5, pp. 733–748.

Fox, James G (1998). *Biology and Diseases of the Ferret*. en. Wiley-Blackwell.

Friedrichs-Maeder, Cecilia L et al. (2017). "Exploring the role of white matter connectivity in cortex maturation". en. In: *PLoS One* 12.5, e0177466.

Gallyas, F (1979). "Silver staining of myelin by means of physical development". en. In: *Neurol. Res.* 1.2, pp. 203–209.

Gao, Yurui et al. (2013). "Validation of DTI tractography-based measures of primary motor area connectivity in the squirrel monkey brain". In: *PLoS ONE* 8.10, e75065.

García-Cabezas, Miguel Á et al. (2016). "Distinction of Neurons, Glia and Endothelial Cells in the Cerebral Cortex: An Algorithm Based on Cytological Features". en. In: *Front. Neuroanat.* 10, p. 107.

Garreta, Raul and Guillermo Moncecchi (2013). *Learning scikit-learn: Machine Learning in Python*. en. Packt Publishing Ltd.

Glasser, Matthew F et al. (2016). "A multi-modal parcellation of human cerebral cortex". en. In: *Nature* 536.7615, pp. 171–178.

Gorgolewski, Krzysztof et al. (2011). "Nipype: a flexible, lightweight and extensible neuroimaging data processing framework in python". en. In: *Front. Neuroinform.* 5, p. 13.

Goulas, Alexandros, Harry B M Uylings, and Claus C Hilgetag (2017). "Principles of ipsilateral and contralateral cortico-cortical connectivity in the mouse". en. In: *Brain Struct. Funct.* 222.3, pp. 1281–1295.

Goulas, Alexandros et al. (2016). *Cytoarchitectonic similarity is a wiring principle of the human connectome*. biorxiv.

Goulas, Alexandros et al. (2019). "A blueprint of mammalian cortical connectomes". en. In: *PLoS Biol.* 17.3, e2005346.

Guarnieri, Fabrizia Claudia et al. (2018). "Disorders of neurogenesis and cortical development". en. In: *Dialogues Clin. Neurosci.* 20.4, pp. 255–266.

Gundersen, H J G and E B Jensen (1985). "The unbiased estimation of number and sizes of arbitrary particles". In: *Bone* 6.5, pp. 413–413.

Hagmann, P et al. (2010). "White matter maturation reshapes structural connectivity in the late developing human brain". en. In: *Proc. Natl. Acad. Sci. U. S. A.* 107.44, pp. 19067–19072.

Harris, Charles R et al. (2020). "Array programming with NumPy". en. In: *Nature* 585.7825, pp. 357–362.

Hasan, K M, D L Parker, and A L Alexander (2001). "Comparison of gradient encoding schemes for diffusion-tensor MRI". en. In: *J. Magn. Reson. Imaging* 13.5, pp. 769–780.

Heimer, Lennart and Martine J Robards (2013). *Neuroanatomical tract-tracing methods*. en. Springer Science & Business Media.

Herculano-Houzel, Suzana (2009). "The human brain in numbers: a linearly scaled-up primate brain". In: *Frontiers in Human Neuroscience* 3.

Herculano-Houzel, Suzana, Charles Watson, and George Paxinos (2013). "Distribution of neurons in functional areas of the mouse cerebral cortex reveals quantitatively different cortical zones". en. In: *Front. Neuroanat.* 7, p. 35.

Heuer, Katja et al. (2016). "Open Neuroimaging Laboratory". In: *Research Ideas and Outcomes* 2, e9113.

Hilgetag, Claus C and Simon Grant (2010). "Cytoarchitectural differences are a key determinant of laminar projection origins in the visual cortex". en. In: *Neuroimage* 51.3, pp. 1006–1017.

Hilgetag, Claus C et al. (2016). "The primate connectome in context: Principles of connections of the cortical visual system". en. In: *Neuroimage* 134, pp. 685–702.

Holmes, Holly E et al. (2017). "Comparison of and MRI for the Detection of Structural Abnormalities in a Mouse Model of Tauopathy". en. In: *Front. Neuroinform.* 11, p. 20.

Horiuchi-Hirose, Miwa and Kazuhiko Sawada (2016). "Differential cortical laminar structure revealed by NeuN immunostaining and myeloarchitecture between sulcal and gyral regions independent of sexual dimorphisms in the ferret cerebrum". en. In: *Anat. Rec.* 299.8, pp. 1003–1011.

Horton, J C (2000). "Boundary disputes". en. In: *Nature* 406.6796, p. 565.

Hosmer Jr., David W and Stanley Lemeshow (2004). *Applied Logistic Regression*. en. John Wiley & Sons.

Inglis, A et al. (2008). "Automated identification of neurons and their locations". en. In: *J. Microsc.* 230.Pt 3, pp. 339–352.

Jackson, C A, J D Peduzzi, and T L Hickey (1989). "Visual cortex development in the ferret. I. Genesis and migration of visual cortical neurons". In: *The Journal of Neuroscience* 9.4, pp. 1242–1253.

Jakab, András et al. (2017). "In utero diffusion tensor imaging of the fetal brain: A reproducibility study". In: *NeuroImage: Clinical* 15, pp. 601–612.

Jenkinson, Mark et al. (2002). "Improved Optimization for the Robust and Accurate Linear Registration and Motion Correction of Brain Images". In: *Neuroimage* 17.2, pp. 825–841.

Jenkinson, Mark et al. (2012). "FSL". en. In: *Neuroimage* 62.2, pp. 782–790.

Jeurissen, Ben et al. (2014). "Multi-tissue constrained spherical deconvolution for improved analysis of multi-shell diffusion MRI data". en. In: *Neuroimage* 103, pp. 411–426.

Jeurissen, Ben et al. (2017). "Diffusion MRI fiber tractography of the brain". en. In: *NMR Biomed.*

Jones, Derek K (2008). "Tractography gone wild: probabilistic fibre tracking using the wild bootstrap with diffusion tensor MRI". en. In: *IEEE Trans. Med. Imaging* 27.9, pp. 1268–1274.

Jones, Derek K, Thomas R Knösche, and Robert Turner (2013). "White matter integrity, fiber count, and other fallacies: The do's and don'ts of diffusion MRI". In: *Neuroimage* 73, pp. 239–254.

Kandel, Eric et al. (2012). *Principles of neural science, Fifth Edition*. en. McGraw Hill Professional.

Kasprian, Gregor et al. (2008). "In utero tractography of fetal white matter development". In: *Neuroimage* 43.2, pp. 213–224.

Kellner, Elias et al. (2016). "Gibbs-ringing artifact removal based on local subvoxel-shifts". en. In: *Magn. Reson. Med.* 76.5, pp. 1574–1581.

Khalil, Reem and Jonathan B Levitt (2014). "Developmental remodeling of corticocortical feedback circuits in ferret visual cortex". en. In: *J. Comp. Neurol.* 522.14, pp. 3208–3228.

Knösche, Thomas R et al. (2015). "Validation of tractography: Comparison with manganese tracing". en. In: *Hum. Brain Mapp.* 36.10, pp. 4116–4134.

Knutsen, Andrew K et al. (2013). "Spatial and temporal variations of cortical growth during gyrogenesis in the developing ferret brain". en. In: *Cereb. Cortex* 23.2, pp. 488–498.

Köbbert, C et al. (2000). "Current concepts in neuroanatomical tracing". en. In: *Prog. Neurobiol.* 62.4, pp. 327–351.

Krubitzer, Leah (2009). "In search of a unifying theory of complex brain evolution". en. In: *Ann. N. Y. Acad. Sci.* 1156, pp. 44–67.

Lempel, Augusto A and Kristina J Nielsen (2019). "Ferrets as a Model for Higher-Level Visual Motion Processing". en. In: *Curr. Biol.* 29.2, 179–191.e5.

Leon, Paula Sanz et al. (2013). "The Virtual Brain: a simulator of primate brain network dynamics". In: *Frontiers in Neuroinformatics* 7.

Liptrot, Matthew G, Karam Sidaros, and Tim B Dyrby (2014). "Addressing the path-length-dependency confound in white matter tract segmentation". en. In: *PLoS One* 9.5, e96247.

Maier-Hein, Klaus H et al. (2017). "The challenge of mapping the human connectome based on diffusion tractography". en. In: *Nat. Commun.* 8.1, p. 1349.

Majka, Piotr et al. (2016). "Towards a comprehensive atlas of cortical connections in a primate brain: Mapping tracer injection studies of the common marmoset into a reference digital template". In: *Journal of Comparative Neurology* 524.11, Spc1–Spc1.

Markov, N T et al. (2014a). "A weighted and directed interareal connectivity matrix for macaque cerebral cortex". en. In: *Cereb. Cortex* 24.1, pp. 17–36.

Markov, Nikola T et al. (2014b). "Anatomy of hierarchy: feedforward and feedback pathways in macaque visual cortex". en. In: *J. Comp. Neurol.* 522.1, pp. 225–259.

Messé, Arnaud (2020). "Parcellation influence on the connectivity-based structure–function relationship in the human brain". In: *Human Brain Mapping* 41.5, pp. 1167–1180.

Messé, Arnaud et al. (2020). *Structural basis of envelope and phase intrinsic coupling modes of the cerebral cortex*. biorxiv.

Mitter, Christian et al. (2015). "Validation of In utero Tractography of Human Fetal Commissural and Internal Capsule Fibers with Histological Structure Tensor Analysis". en. In: *Front. Neuroanat.* 9, p. 164.

Miyawaki, Yoichi (2016). "Multivariate Analysis of Magnetic Resonance Imaging Signals of the Human Brain". In: *Current Topics in Medicinal Chemistry* 16.24, pp. 2685–2693.

Neal, Jason et al. (2007). "Insights into the gyrification of developing ferret brain by magnetic resonance imaging". en. In: *J. Anat.* 210.1, pp. 66–77.

Oliphant, Travis (2015). *Guide to NumPy: 2nd Edition*. en. CreateSpace.

Pandya, Deepak N et al. (2015). *Cerebral Cortex: Architecture, Connections, and the Dual Origin Concept*. en. Oxford University Press, USA.

Park, Hae-Jeong and Karl Friston (2013). "Structural and functional brain networks: from connections to cognition". en. In: *Science* 342.6158, p. 1238411.

Radtke-Schuller, Susanne (2018). *Cyto- and Myeloarchitectural Brain Atlas of the Ferret (Mustela putorius) in MRI Aided Stereotaxic Coordinates*. en. Springer.

Rahimi-Balaei, Maryam et al. (2018). "Neuronal Migration During Development of the Cerebellum". en. In: *Front. Cell. Neurosci.* 12, p. 484.

Rakic, P (1974). "Neurons in rhesus monkey visual cortex: systematic relation between time of origin and eventual disposition". en. In: *Science* 183.4123, pp. 425–427.

Redell, John B et al. (2020). "Traumatic brain injury and hippocampal neurogenesis: Functional implications". en. In: *Exp. Neurol.* 331, p. 113372.

Reillo, Isabel and Víctor Borrell (2012). "Germinal zones in the developing cerebral cortex of ferret: ontogeny, cell cycle kinetics, and diversity of progenitors". en. In: *Cereb. Cortex* 22.9, pp. 2039–2054.

Reillo, Isabel et al. (2011). "A role for intermediate radial glia in the tangential expansion of the mammalian cerebral cortex". en. In: *Cereb. Cortex* 21.7, pp. 1674–1694.

Roberts, James A et al. (2016). "The contribution of geometry to the human connectome". en. In: *Neuroimage* 124.Pt A, pp. 379–393.

Roe, A W et al. (1992). "Visual projections routed to the auditory pathway in ferrets: receptive fields of visual neurons in primary auditory cortex". en. In: *J. Neurosci.* 12.9, pp. 3651–3664.

Rogers, Cynthia E et al. (2018). "Aberrant structural and functional connectivity and neurodevelopmental impairment in preterm children". en. In: *J. Neurodev. Disord.* 10.1, p. 38.

Rubinov, Mikail and Olaf Sporns (2010). "Complex network measures of brain connectivity: uses and interpretations". en. In: *Neuroimage* 52.3, pp. 1059–1069.

Sarwar, Tabinda, Kotagiri Ramamohanarao, and Andrew Zalesky (2019). "Mapping connectomes with diffusion MRI: deterministic or probabilistic tractography?" en. In: *Magn. Reson. Med.*

Sawada, Kazuhiko and Misaki Watanabe (2012). "Development of cerebral sulci and gyri in ferrets (Mustela putorius)". en. In: *Congenit. Anom.* 52.3, pp. 168–175.

Sawada, Kazuhiko et al. (2013). "MRI-based morphometric characterizations of sexual dimorphism of the cerebrum of ferrets (Mustela putorius)". en. In: *Neuroimage* 83, pp. 294–306.

Schilling, Kurt G et al. (2018). "Challenges in diffusion MRI tractography - Lessons learned from international benchmark competitions". en. In: *Magn. Reson. Imaging* 57, pp. 194–209.

Schilling, Kurt G et al. (2019a). "Anatomical accuracy of standard-practice tractography algorithms in the motor system - A histological validation in the squirrel monkey brain". en. In: *Magn. Reson. Imaging* 55, pp. 7–25.

Schilling, Kurt G et al. (2019b). "Limits to anatomical accuracy of diffusion tractography using modern approaches". en. In: *Neuroimage* 185, pp. 1–11.

Schleicher, A, K Zilles, and A Wree (1986). "A quantitative approach to cytoarchitectonics: software and hardware aspects of a system for the evaluation and analysis of structural inhomogeneities in nervous tissue". en. In: *J. Neurosci. Methods* 18.1-2, pp. 221–235.

Schleicher, A et al. (1999). "Observer-independent method for microstructural parcellation of cerebral cortex: A quantitative approach to cytoarchitectonics". en. In: *Neuroimage* 9.1, pp. 165–177.

Schleicher, Axel and Karl Zilles (1990). "A quantitative approach to cytoarchitectonics: Analysis of structural inhomogeneities in nervous tissue using an image analyser". In: *Journal of Microscopy* 157.3, pp. 367–381.

Schleicher, Axel et al. (2009). "Quantitative architectural analysis: a new approach to cortical mapping". en. In: *J. Autism Dev. Disord.* 39.11, pp. 1568–1581.

Schotten, Michel Thiebaut de, Chris Foulon, and Parashkev Nachev (2020). *Brain disconnections link structural connectivity with function and behaviour*. biorxiv.

Sinke, Michel R T et al. (2018). "Diffusion MRI-based cortical connectome reconstruction: dependency on tractography procedures and neuroanatomical characteristics". en. In: *Brain Struct. Funct.* 223.5, pp. 2269–2285.

Smart, I H and G M McSherry (1986a). "Gyrus formation in the cerebral cortex in the ferret. I. Description of the external changes". en. In: *J. Anat.* 146, pp. 141–152.

Smart, I H and G M McSherry (1986b). "Gyrus formation in the cerebral cortex of the ferret. II. Description of the internal histological changes". en. In: *J. Anat.* 147, pp. 27–43.

Snyder, Jessica M et al. (2018). "Ontogeny of white matter, toll-like receptor expression, and motor skills in the neonatal ferret". en. In: *Int. J. Dev. Neurosci.* 70, pp. 25–33.

Song, Jae W et al. (2018). "How accurate are prenatal tractography results? A postnatal in vivo follow-up study using diffusion tensor imaging". en. In: *Pediatr. Radiol.* 48.4, pp. 486–498.

Sporns, Olaf (2010). *Networks of the Brain*. MIT Press.

Sporns, Olaf, Giulio Tononi, and Rolf Kötter (2005). "The Human Connectome: A Structural Description of the Human Brain". In: *PLoS Computational Biology* 1.4, e42.

Sur, Mriganka and Catherine A Leamey (2001). "Development and plasticity of cortical areas and networks". In: *Nature Reviews Neuroscience* 2.4, pp. 251–262.

Talairach, Jean and Pierre Tournoux (1988). *Co-planar Stereotaxic Atlas of the Human Brain: 3-dimensional Proportional System : an Approach to Cerebral Imaging*. en. George Thieme Verlag.

Tang, Shiyu et al. (2018). "Effects of Early Alcohol Exposure on Functional Organization and Microstructure of a Visual-Tactile Integrative Circuit". en. In: *Alcohol. Clin. Exp. Res.* 42.4, pp. 727–734.

Tardif, Suzette D et al. (2003). "Reproduction in captive common marmosets (Callithrix jacchus)". en. In: *Comp. Med.* 53.4, pp. 364–368.

Thomas, Cibu et al. (2014). "Anatomical accuracy of brain connections derived from diffusion MRI tractography is inherently limited". en. In: *Proc. Natl. Acad. Sci. U. S. A.* 111.46, pp. 16574–16579.

Toro, Roberto (2012). *On the Possible Shapes of the Brain*.

Toro, Roberto et al. (in prep). "Expansion and folding of the ferret neocortex".

Tournier, J-Donald, Fernando Calamante, and Alan Connelly (2010). "Improved probabilistic streamlines tractography by 2nd order integration over fibre orientation distributions". In: Proc. Intl. Soc. Mag. Reson. Med.

– (2012). "MRtrix: Diffusion tractography in crossing fiber regions". In: *International Journal of Imaging Systems and Technology* 22.1, pp. 53–66.

– (2013). "Determination of the appropriate b value and number of gradient directions for high-angular-resolution diffusion-weighted imaging". en. In: *NMR Biomed.* 26.12, pp. 1775–1786.

Tustison, Nicholas J and Brian B Avants (2013). "Explicit B-spline regularization in diffeomorphic image registration". en. In: *Front. Neuroinform.* 7, p. 39.

Tustison, Nicholas J et al. (2010). "N4ITK: improved N3 bias correction". en. In: *IEEE Trans. Med. Imaging* 29.6, pp. 1310–1320.

Tzourio-Mazoyer, N et al. (2002). "Automated anatomical labeling of activations in SPM using a macroscopic anatomical parcellation of the MNI MRI single-subject brain". en. In: *Neuroimage* 15.1, pp. 273–289.

Van Essen, David C et al. (2013). "The WU-Minn Human Connectome Project: an overview". en. In: *Neuroimage* 80, pp. 62–79.

Varela, F et al. (2001). "The brainweb: phase synchronization and large-scale integration". en. In: *Nat. Rev. Neurosci.* 2.4, pp. 229–239.

Veraart, Jelle et al. (2016). "Denoising of diffusion MRI using random matrix theory". en. In: *Neuroimage* 142, pp. 394–406.

Virtanen, Pauli et al. (2020). "SciPy 1.0: fundamental algorithms for scientific computing in Python". en. In: *Nat. Methods* 17.3, pp. 261–272.

Visser, Milanka M et al. (2018). "White matter degeneration after ischemic stroke: a longitudinal diffusion tensor imaging study". en. In: *J. Neuroimaging*.

Voigt, T (1989). "Development of glial cells in the cerebral wall of ferrets: direct tracing of their transformation from radial glia into astrocytes". en. In: *J. Comp. Neurol.* 289.1, pp. 74–88.

Voigt, T, A D De Lima, and M Beckmann (1993). "Synaptophysin immunohistochemistry reveals inside-out pattern of early synaptogenesis in ferret cerebral cortex". en. In: *J. Comp. Neurol.* 330.1, pp. 48–64.

Wagstyl, Konrad et al. (2018). "Mapping Cortical Laminar Structure in the 3D BigBrain". en. In: *Cereb. Cortex* 28.7, pp. 2551–2562.

Walt, Stéfan van der et al. (2014). "scikit-image: image processing in Python". en. In: *PeerJ* 2, e453.

Wei, Yongbin et al. (2019). "Multiscale examination of cytoarchitectonic similarity and human brain connectivity". en. In: *Netw Neurosci* 3.1, pp. 124–137.

Wood, Thomas et al. (2018). "A Ferret Model of Encephalopathy of Prematurity". en. In: *Dev. Neurosci.* 40.5-6, pp. 475–489.

Wree, A, A Schleicher, and K Zilles (1982). "Estimation of volume fractions in nervous tissue with an image analyzer". en. In: *J. Neurosci. Methods* 6.1-2, pp. 29–43.

Wu, Zhanxiong et al. (2019). "Effects of Brain Parcellation on the Characterization of Topological Deterioration in Alzheimer's Disease". en. In: *Front. Aging Neurosci.* 11, p. 113.

Zaborszky, Laszlo, Floris G Wouterlood, and José Luis Lanciego (2006). *Neuroanatomical Tract-Tracing: Molecules, Neurons, and Systems*. en. Springer Science & Business Media.

Zalesky, Andrew et al. (2016). "Connectome sensitivity or specificity: which is more important?" In: *Neuroimage* 142, pp. 407–420.

Zervas, M and S U Walkley (1999). "Ferret pyramidal cell dendritogenesis: changes in morphology and ganglioside expression during cortical development". en. In: *J. Comp. Neurol.* 413.3, pp. 429–448.

Zhang, Tuo et al. (2018). "Optimization of macaque brain DMRI connectome by neuron tracing and myelin stain data". en. In: *Comput. Med. Imaging Graph.* 69, pp. 9–20.

Zhou, Zhe Charles et al. (2016). "Resting state network topology of the ferret brain". en. In: *Neuroimage* 143, pp. 70–81.

Zingg, Brian et al. (2014). "Neural networks of the mouse neocortex". In: *Annals of Neurosciences* 22.4.

Supplementary material from chapter 3

Supplementary figures from Delettre et al. 2019.

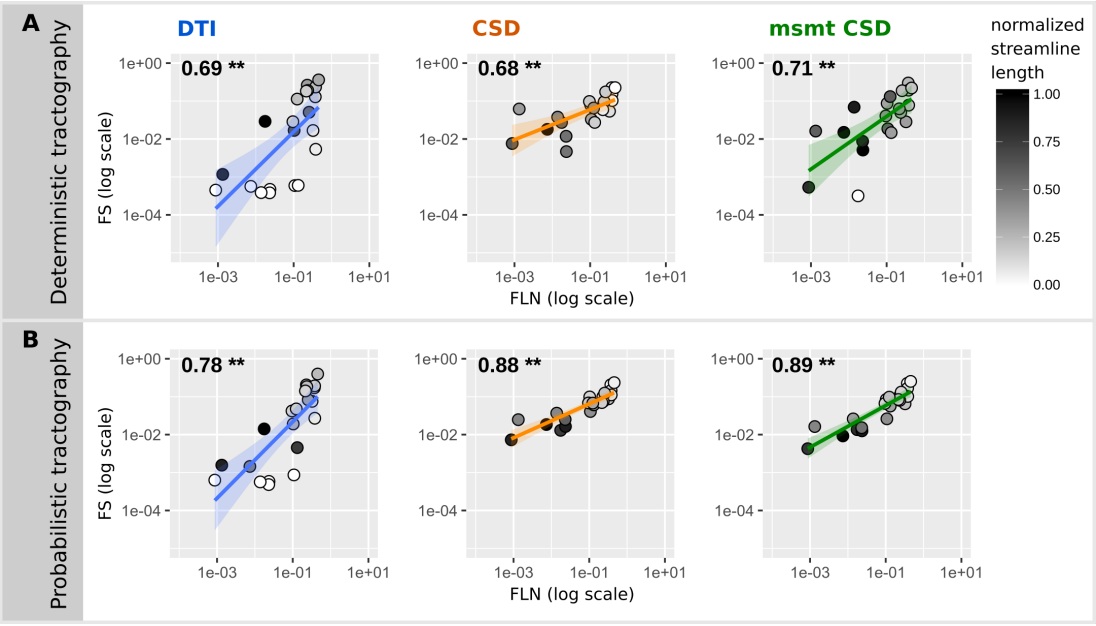

Figure A.1: **Pearson's correlation between diffusion MRI tractography and tract-tracing experiments (symmetrical matrix).**
Scatterplots of the ranked fraction of neurons vs. the ranked fraction of streamlines for deterministic (A) and the probabilistic (B) tractography. Grey colors code for the average streamline length (values normalized by the maximum streamline length of all the algorithms). P-values inferior to 1.10-3 are indicated by ** and p-values inferior to 0.05 by *.

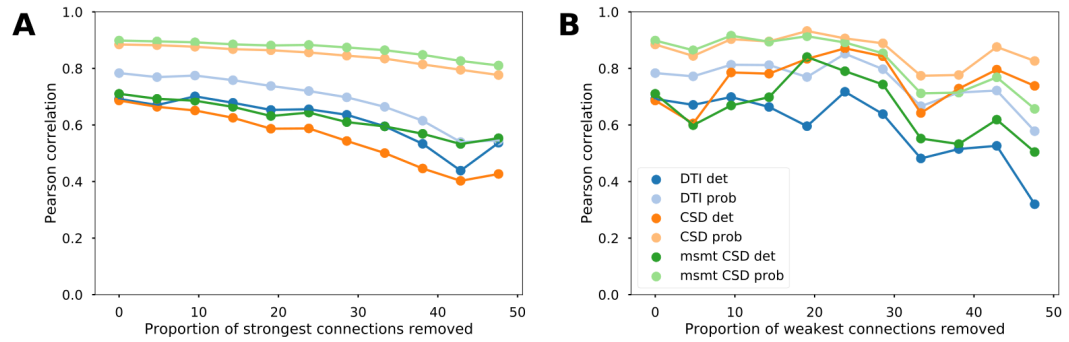

Figure A.2: **Reliability of the association between diffusion MRI tractography and tract-tracing data (symmetrical matrix).**
Evolution of the Pearson correlation values between tract-tracing and diffusion MRI tractography data as a function of the proportion of removed strong (A) and weak (B) connections for the different tractography models.

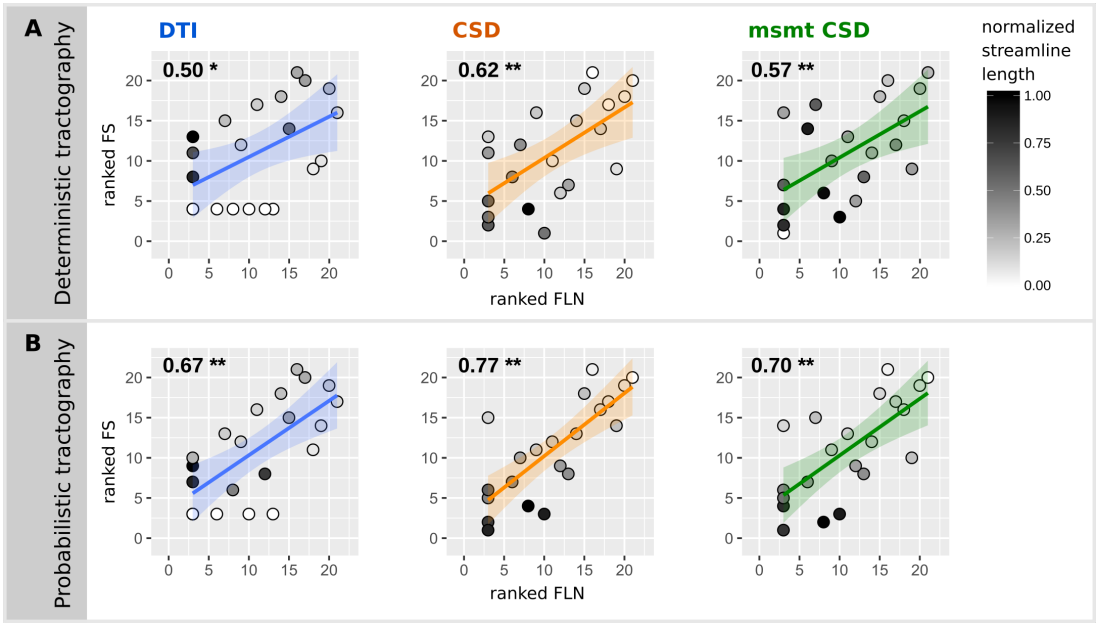

Figure A.3: **Spearman's correlation between diffusion MRI tractography and tract-tracing experiments (directed matrix).**
Scatterplots of the ranked fraction of neurons vs. the ranked fraction of streamlines for deterministic (A) and the probabilistic (B) tractography. Grey colors code for the average streamline length (values normalized by the maximum streamline length of all the algorithms). P-values inferior to 1.10-3 are indicated by ** and p-values inferior to 0.05 by *.

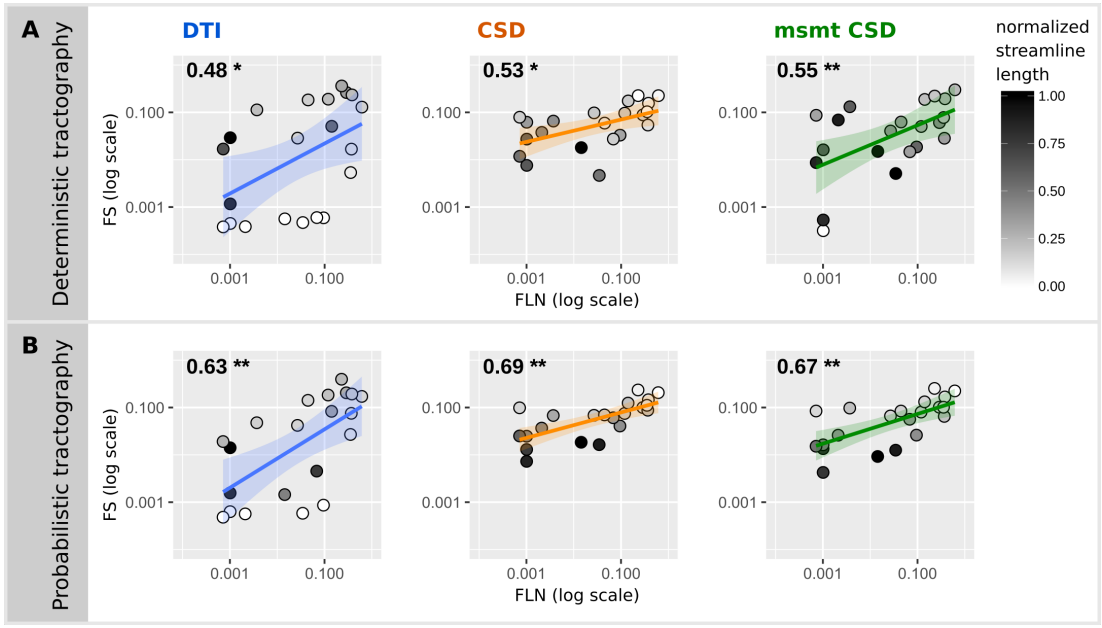

Figure A.4: **Pearson's correlation between diffusion MRI tractography and tract-tracing experiments (directed matrix).**
Scatterplots of the ranked fraction of neurons vs. the ranked fraction of streamlines for deterministic (A) and the probabilistic (B) tractography. Grey colors code for the average streamline length (values normalized by the maximum streamline length of all the algorithms). P-values inferior to 1.10-3 are indicated by ** and p-values inferior to 0.05 by *.

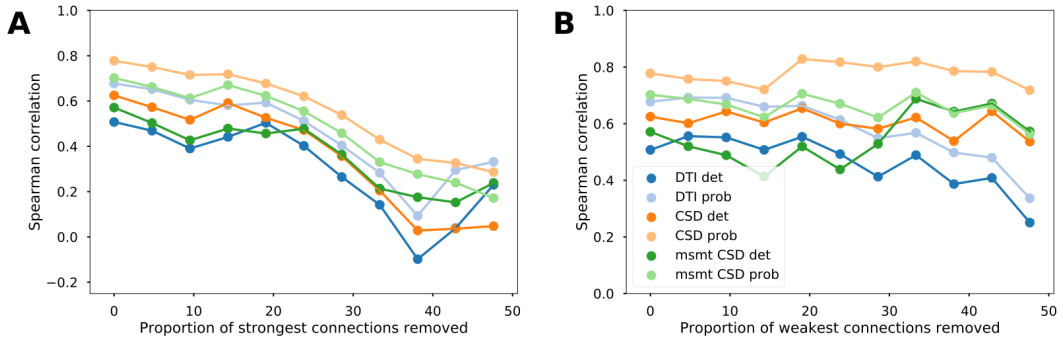

Figure A.5: **Reliability of the association between diffusion MRI tractography and tract-tracing data (directed matrix).**
Evolution of the Spearman correlation values between tract-tracing and diffusion MRI tractography data as a function of the proportion of removed strong (A) and weak (B) connections for the different tractography models.

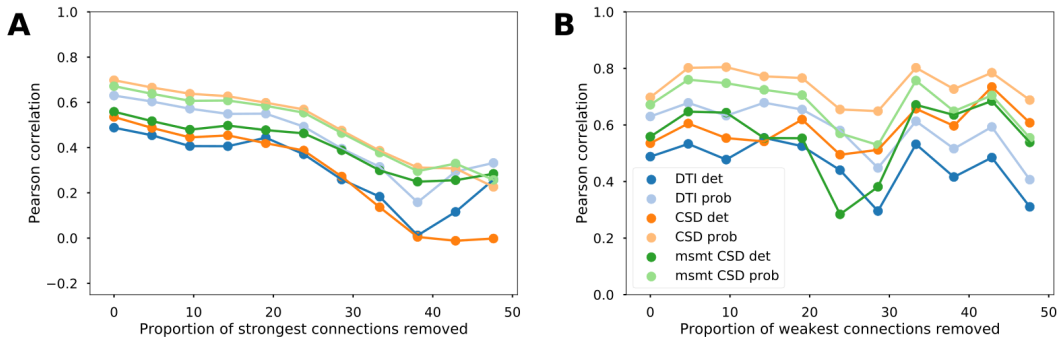

Figure A.6: **Reliability of the association between diffusion MRI tractography and tract-tracing data (directed matrix).**
Evolution of the Pearson correlation values between tract-tracing and diffusion MRI tractography data as a function of the proportion of removed strong (A) and weak (B) connections for the different tractography models.

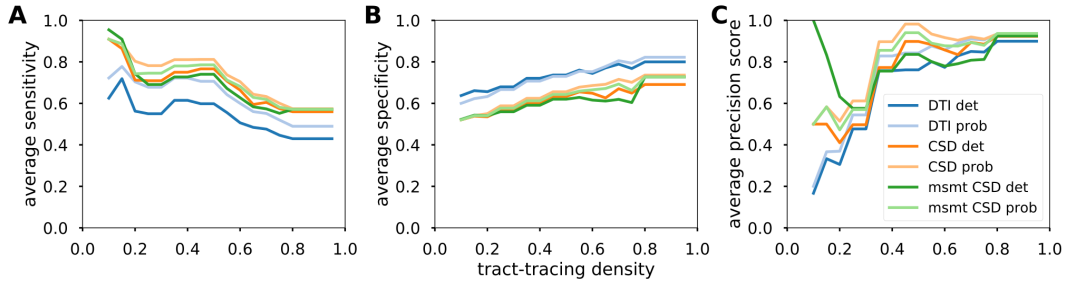

Figure A.7: **Average sensitivity (A), average specificity (B) and average precision score (C) along tract-tracing density (directed matrix).**

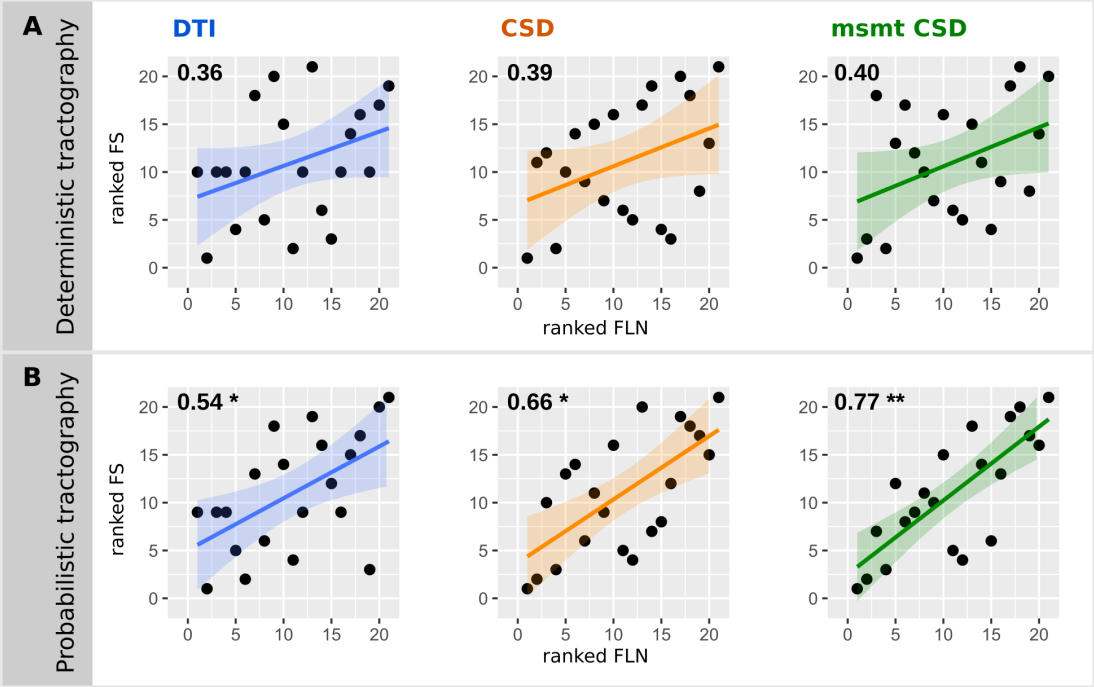

Figure A.8: **Spearman's partial correlation between diffusion MRI tractography and tract-tracing experiments (symmetrical matrix).**
Scatterplots of the ranked residuals FLN after regressing out the euclidean distance between each pair of areas vs. the ranked residuals FS for deterministic (A) and the probabilistic (B) tractography. P-values inferior to 1.10-3 are indicated by ** and p-values inferior to 0.05 by *.

		Undirected tract-tracing matrix		Directed tract-tracing matrix	
		Spearman	Pearson	Spearman	Pearson
Deterministic	DTI	0.36	0.56 *	0.38	0.3
	CSD	0.39	0.44 *	0.35	0.23
	msmt CSD	0.4	0.50 *	0.39	0.3
Probabilistic	DTI	0.54 *	0.66 **	0.55 *	0.46 *
	CSD	0.66 *	0.85 **	0.67 *	0.53 *
	msmt CSD	0.77 **	0.85 **	0.77 **	0.48 *

Table A.1: **Partial correlations between diffusion MRI tractography and tract-tracing experiments after regressing out the euclidean distance between each pair of areas.**

Supplementary material from chapter 5

Connectivity subject	Histology subject	AUC	Standard deviation	Coefficient cytoarchitecture	Coefficient distance	Log-likelihood
P4	P4	0.650	0.009	0.042	-0.232	-7498.677
P4	P8	0.668	0.009	-0.156	-0.191	-8112.527
P4	P16	0.660	0.009	-0.154	-0.158	-8260.311
P4	P32	0.648	0.009	-0.038	-0.101	-7763.811
P8	P4	0.676	0.009	-0.176	-0.266	-8080.015
P8	P8	0.685	0.009	-0.267	-0.212	-8557.586
P8	P16	0.672	0.009	0.037	-0.173	-8761.451
P8	P32	0.660	0.009	0.074	-0.109	-8319.137
P16	P4	0.616	0.011	-0.030	-0.175	-7358.116
P16	P8	0.625	0.009	0.015	-0.140	-7866.280
P16	P16	0.620	0.009	0.095	-0.116	-7984.765
P16	P32	0.614	0.011	-0.038	-0.074	-7436.546
P32	P4	0.651	0.009	0.397	-0.194	-9509.253
P32	P8	0.649	0.007	0.392	-0.153	-10349.976
P32	P16	0.626	0.008	0.209	-0.121	-10629.257
P32	P32	0.624	0.009	0.173	-0.079	-9994.979
Adult	P4	0.607	0.008	0.243	-0.142	-8989.699
Adult	P8	0.619	0.009	0.338	-0.114	-9783.869
Adult	P16	0.603	0.008	0.346	-0.090	-9997.200
Adult	P32	0.601	0.009	0.161	-0.061	-9250.394

Table B.1: **Bivariate model, cytoarchitectonic similarity and distance as estimators for connectivity.**
Age of the subjects for the connectivity and histology datasets (P4 = postnatal day 4). Average AUC for 100 random sampling of the dataset. Standard deviation of the 100 AUC. Coefficients of the logistic regression.

Connectivity subject	Histology subject	AUC	Standard deviation	Coefficient distance	Log-likelihood	Likelihood ratio p-value
P4	P4	0.6499	0.0092	-0.2313	-7500.2636	0.1201
P4	P8	0.6652	0.0093	-0.1917	-8130.2017	< 0.001
P4	P16	0.6584	0.0086	-0.1576	-8270.2267	< 0.001
P4	P32	0.6483	0.0089	-0.1005	-7764.7921	0.2249
P8	P4	0.6709	0.0090	-0.2674	-8110.3839	< 0.001
P8	P8	0.6785	0.0090	-0.2128	-8611.3677	< 0.001
P8	P16	0.6720	0.0091	-0.1733	-8761.9134	0.4223
P8	P32	0.6591	0.0087	-0.1090	-8321.9373	0.0332
P16	P4	0.6164	0.0106	-0.1754	-7359.1500	0.2236
P16	P8	0.6256	0.0085	-0.1403	-7866.4663	0.6450
P16	P16	0.6201	0.0090	-0.1155	-7987.7234	0.0282
P16	P32	0.6147	0.0109	-0.0736	-7437.4726	0.2430
P32	P4	0.6218	0.0092	-0.1839	-9702.0224	< 0.001
P32	P8	0.6299	0.0079	-0.1472	-10500.0219	< 0.001
P32	P16	0.6221	0.0080	-0.1202	-10652.0405	< 0.001
P32	P32	0.6191	0.0087	-0.0793	-10015.6198	< 0.001
Adult	P4	0.5916	0.0078	-0.1378	-9061.2020	< 0.001
Adult	P8	0.5986	0.0090	-0.1095	-9892.0349	< 0.001
Adult	P16	0.5920	0.0084	-0.0889	-10055.1914	< 0.001
Adult	P32	0.5963	0.0090	-0.0614	-9266.3704	< 0.001

Table B.2: **Univariate model, distance as estimator for connectivity.**
Age of the subjects for the connectivity and histology datasets (P4 = postnatal day 4). Average AUC for 100 random sampling of the dataset. Standard deviation of the 100 AUC. Coefficient of the logistic regression. P-value from the likelihood ratio test between the univariate distance based model and the bivariate model. A p-value under 0.05 indicated that adding the second estimator (here cytoarchitectonic similarity) improved significantly the prediction of the connectivity.

Connectivity subject	Histology subject	AUC	Standard deviation	Coefficient cytoarchitecture	Log-likelihood	Likelihood ratio p-value
P4	P4	0.497	0.010	0.019	-7857.227	< 0.001
P4	P8	0.533	0.009	-0.177	-8577.329	< 0.001
P4	P16	0.522	0.009	-0.159	-8696.771	< 0.001
P4	P32	0.493	0.008	-0.003	-8127.793	< 0.001
P8	P4	0.543	0.010	-0.189	-8602.860	< 0.001
P8	P8	0.552	0.010	-0.281	-9174.578	< 0.001
P8	P16	0.499	0.009	0.019	-9331.257	< 0.001
P8	P32	0.514	0.009	0.105	-8783.430	< 0.001
P16	P4	0.530	0.011	-0.046	-7558.853	< 0.001
P16	P8	0.500	0.016	-0.006	-8109.851	< 0.001
P16	P16	0.511	0.010	0.082	-8210.723	< 0.001
P16	P32	0.497	0.011	-0.012	-7622.528	< 0.001
P32	P4	0.585	0.008	0.361	-9856.180	< 0.001
P32	P8	0.569	0.008	0.351	-10769.772	< 0.001
P32	P16	0.531	0.007	0.191	-10993.449	< 0.001
P32	P32	0.529	0.009	0.191	-10309.306	< 0.001
Adult	P4	0.559	0.009	0.224	-9163.740	< 0.001
Adult	P8	0.573	0.009	0.313	-9999.534	< 0.001
Adult	P16	0.548	0.008	0.331	-10183.374	< 0.001
Adult	P32	0.529	0.009	0.177	-9419.362	< 0.001

Table B.3: **Univariate model, cytoarchitectonic similarity as estimator for connectivity.** Age of the subjects for the connectivity and histology datasets (P4 = postnatal day 4). Average AUC for 100 random sampling of the dataset. Standard deviation of the 100 AUC. Coefficient of the logistic regression. P-value from the likelihood ratio test between the univariate distance based model and the bivariate model. A p-value under 0.05 indicated that adding the second estimator (here distance) improved significantly the prediction of the connectivity.

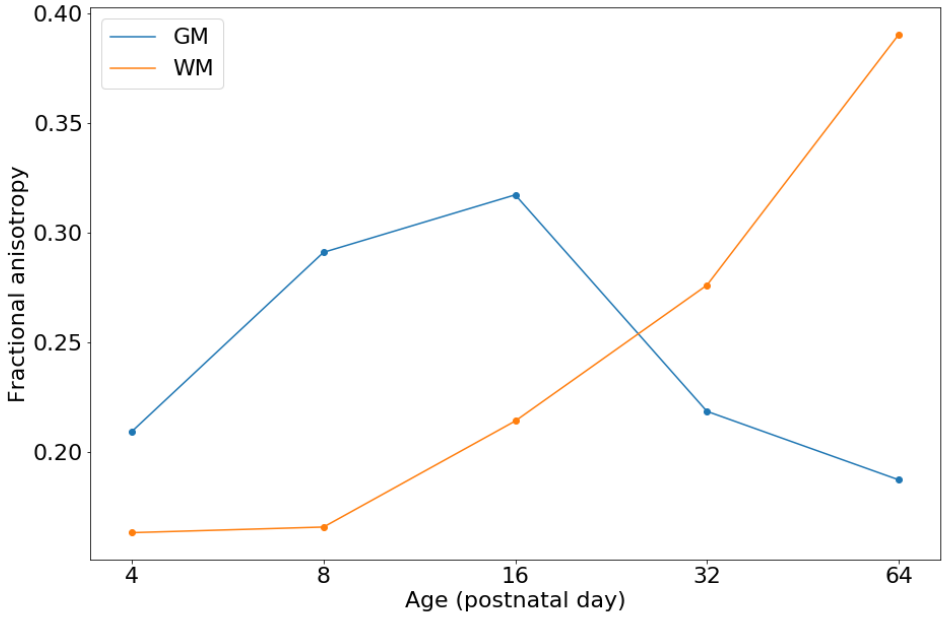

Figure B.1: **Evolution of the fractional anisotropy contrast in the GM and WM with development.**